Realization of the First MW-Class Gyrotron Multistage Depressed Collector

Zur Erlangung des akademischen Grades eines

DOKTORS DER INGENIEURWISSENSCHAFTEN (Dr.-Ing.)

von der KIT-Fakultät für Elektrotechnik und Informationstechnik des Karlsruher Instituts für Technologie (KIT)

angenommene

DISSERTATION

von

M.Sc. Benjamin Ell
geb. in Karlsruhe

Tag der mündlichen Prüfung:	11.07.2025
Hauptreferent:	Prof. Dr.-Ing. John Jelonnek
Korreferent:	Dr. Jean-Philippe Hogge

Kurzfassung

Mit steigendem Energiebedarf bietet die kontrollierte Fusion leichter Atomkerne eine vielversprechende Alternative zu fossilen Brennstoffen, die saubere und reichlich vorhandene Energie erzeugt. Im Gegensatz zu unserer Sonne sind wesentlich höhere Plasmatemperaturen erforderlich, um eine sich selbst erhaltende Fusionsreaktion bei geringerem Plasmadruck zu erreichen. Die Elektronen Zyklotron Resonanz Heizung (engl. ECRH) wird zum Aufheizen und Stabilisieren des Plasmas verwendet und basiert auf einer Kombination mehrerer parallel arbeitender Gyrotrons. In aktuellen Fusionsanlagen wie Wendelstein 7-X (W7-X) und ITER werden 10 bis 24 Gyrotrons mit einer Ausgangsleistung von 1 MW eingesetzt, mit weiteren Verbesserungen in Bezug auf Anzahl und Geräteleistung in der Zukunft. Diese Gyrotrons werden mit Kollektoren mit einstufiger Gegenspannung (Singlestage Depressed Collector: SDC) betrieben und erreichen einen Gesamtwirkungsgrad von bis zu 50 %. Künftige Projekte wie das DEMOnstrationskraftwerk (DEMO) werden mehr ECRH Leistung und längere Betriebszeiten erfordern, um Nettoenergie ins Netz zu liefern. Aufgrund des hohen Stromverbrauchs von ECRH Installationen mit vielen MW sind Fortschritte beim Gyrotron-Wirkungsgrad erforderlich. In dieser Arbeit wird der Einsatz von mehrstufigen Kollektoren (Multistage Depressed Collector: MDC) vorgeschlagen, um den Gyrotron-Wirkungsgrad von 50 % auf 60 % zu erhöhen, wodurch die Ausgangsleistung des Kraftwerks erhöht und die Betriebskosten gesenkt werden, was die Fusion als realisierbare Energiequelle voranbringt.

Der MDC mit $\vec{E}\times\vec{B}$ Drift ist der vielversprechendste Ansatz für die Trennung von Elektronenbahnen in einem Hochleistungsgyrotron. Die größten Herausforderungen bei der Entwicklung des ersten MDC für ein Gyrotron sind die Anpassung an die bestehende Technik mit einem zuverlässigen Design bei gleichzeitiger Minimierung von Kosten und Aufwand. Zu den bestehenden driftbasierten MDC Geometriekonzepten gehören Auslegungen mit einem axialen elektrischen Feld und zwei mit azimutalen elektrischen Feldern, der

koaxiale und der zylindrische Ansatz. Das zylindrische Design wurde hier aufgrund seiner Einfachheit mit weniger Elementen und einem vereinfachten magnetischen Aufbau ausgewählt.

In dieser Arbeit wird der zylindrische MDC Ansatz erfolgreich optimiert und zu einem zweistufigen Prototyp Design entwickelt, um eine starke $\vec{E}\times\vec{B}$ Drift in einem kompakten und modularen Gehäuse zu erreichen. Eine Auslegung mit dreifach Helix wurde aufgrund seiner Kompaktheit gewählt. Dies wurde kombiniert mit geraden zylindrischen Elektroden für eine einfachere Herstellung und einem weiterentwickelten Arbeitspunkt für eine zusätzliche Größenreduzierung. Nach der empirischen Optimierung des elektromagnetischen Designs wird dieses in einer erweiterten Toleranzanalyse mit den Auswirkungen auf die elektrische Leistung validiert. Im nominalen Betriebspunkt wird ein Kollektorwirkungsgrad von 78.8 % mit einem reflektierten Strom von lediglich 50 mA erreicht, was einem Gesamt-Gyrotronwirkungsgrad von 64.6 % entspricht. Die Anpassung an bestehende Gyrotrons am Karlsruher Institut für Technologie (KIT) mit verschiedenen Betriebsszenarien zeigt, wie die flexible Auslegung verschiedene Versuchsaufbauten ermöglicht.

Die mechanische Konstruktion des Kurzpuls MDC Prototyps integriert Design For Manufacturing (DFM) und Design For Assembly (DFA) Prinzipien, um eine effiziente Fertigung und Montage zu gewährleisten. Der Schwerpunkt liegt auf einer zuverlässigen und robusten Auslegung, die für eine experimentelle Validierung geeignet ist. Zu den Schlüsselelementen gehören die Verwendung von standardisierten Ultrahochvakuum Dichtungssystemen und modularen mechanischen Komponenten. Die Montage des MDC sowohl in der Konfiguration für das KIT 2 MW koaxiale Kavitäts Gyrotron, als auch für das W7-X Upgrade Kurzpuls Gyrotron bestätigt die Anpassungsfähigkeit und Verfügbarkeit des Systems für MDC Experimente.

Zusätzlich zum Kurzpuls MDC Prototyp werden die gleichen Prinzipien auf einen MDC für Dauerbetrieb (Continuous Wave: CW) angewandt, um einen Ausblick auf die zukünftige Forschung zu geben. Es wird gezeigt, dass die thermische Kollektorwandbelastung erfolgreich reduziert werden kann, um mit den aktuellen Kühltechniken kompatibel zu sein, während die Elektrodengröße erheblich reduziert wird. Die kleinere Elektrodengröße wird auch bei einem neuen SDC Design mit fortschrittlichem elektrischen Feld Sweeping auf der Grundlage der $\vec{E}\times\vec{B}$ Drift eingesetzt, um die Sweeping Frequenz deutlich zu erhöhen und Temperaturschwankungen zu minimieren.

Abstract

As the global demand for sustainable energy grows, controlled fusion of light atom nuclei offers a promising alternative to fossil fuels, producing clean and abundant energy. In contrast to the fusion process in our Sun, much higher plasma temperatures are required to achieve a self-sustaining fusion reaction at the reduced plasma pressure required for magnetic confinement. The Electron Cyclotron Resonance Heating (ECRH) is used to heat and stabilize the plasma and is based on a combination of multiple gyrotrons operating in parallel. Current fusion devices, such as Wendelstein 7-X (W7-X) and ITER, use 10 to 24 gyrotrons with an output power of 1 MW in the first phase and planned upgrades in number and unit power in the future. These gyrotrons are operated with Singlestage Depressed Collectors (SDCs) and achieve an overall efficiency of up to 50 %. Future projects, such as the DEMOnstration power plant (DEMO), will require more ECRH power and longer operating times to provide net power to the grid. Advancements in gyrotron efficiency are required to achieve effective power generation due to the high-power consumption of ECRH installations with many MW. This work proposes the use of Multistage Depressed Collectors (MDCs) to increase the gyrotron efficiency from 50 % to 60 %, thereby increasing the output power of the plant and reducing operating costs, advancing fusion as a viable energy source.

The MDC with $\vec{E}\times\vec{B}$ drift is the most promising approach for the separation of electron trajectories in a high-power gyrotron. The main challenges in the development of the first MDC for a megawatt-class gyrotron are the adaptation to existing equipment with a reliable design while minimizing cost and effort. The existing $\vec{E}\times\vec{B}$ drift-based MDC geometry concepts include designs with an axial electric field and two with azimuthal electric fields, the coaxial and the cylindrical approach. Among all the concepts investigated, the cylindrical design is selected here due to its simplicity with fewer parts and a simplified magnetic setup, which is critical to effectively demonstrate the basic principle of electron separation.

In this work, the cylindrical MDC approach is successfully optimized and developed into a two-stage prototype design to achieve strong $\vec{E}\times\vec{B}$ drift in a small and modular package. A triple helix design is chosen for its advantages in compactness, combined with straight cylindrical electrodes for easier fabrication and an advanced operating point for further size reduction. After the empirical optimization of the electromagnetic design, it is validated in an extended tolerance analysis with the effects on the electrical performance. At the nominal operation point, a collector efficiency of 78.8 % with a reflected current of only 50 mA is achieved which correlates to a total gyrotron efficiency of 64.6 %. The adaptation of the MDC to existing gyrotrons at Karlsruhe Institute of Technology (KIT) with different operating scenarios shows how the flexible design can facilitate diverse experimental setups.

The mechanical design of the Short-Pulse (SP) MDC prototype integrates Design For Manufacturing (DFM) and Design For Assembly (DFA) principles to ensure efficient manufacturing and assembly. The focus is on achieving a reliable and robust design suitable for experimental validation. Key elements include the use of standardized ultra-high vacuum sealing systems and modular mechanical components that allow flexible adaptation to different gyrotron configurations. The assembly of the MDC, using both the KIT 2 MW 170 GHz coaxial-cavity gyrotron and the W7-X upgrade SP gyrotron configurations, confirms the adaptability and readiness of the system for MDC experiments.

In addition to the SP MDC prototype, the same design principles are applied to an upscaled Continuous Wave (CW) MDC design approach to provide an outlook for future research in this technology. It is shown that the power loading density can be successfully reduced to be compatible with current cooling techniques, while the electrode size is significantly reduced. The smaller electrode size is also applied to a new SDC design with advanced electric field sweeping based on the $\vec{E}\times\vec{B}$ drift to significantly increase the sweeping frequency. The increased sweeping frequency minimizes temperature variation and thus cyclic thermal fatigue, which could result in higher acceptable power loading densities.

Contents

Abbreviations

ACI	After Cavity Interaction
CEA	Commissariat à l'énergie atomique et aux énergies alternatives
CF	ConFlat
CNC	Computerized Numerical Control
COMSOL	COMSOL Multiphysics®
CST	CST Studio Suite
CuCr1Zr	Copper-Chromium-Zirconium
CW	Continuous Wave
DEMO	DEMOnstration power plant
DFA	Design For Assembly
DFM	Design For Manufacturing
ECRH	Electron Cyclotron Resonance Heating
EU	European Union
FKM	Fluorine rubber (german: Fluorine Kautschuk Material)
FULGOR	**Fu**sion **L**ong Pulse **G**yrotron Lab**or**atory
GND	Ground Potential
HV	HyperVapotron
IHM	Institute for Pulsed Power and Microwave Technology

KIT	Karlsruhe Institute of Technology
LMFS	Longitudinal Magnetic Field Sweeping
LP	Long-Pulse
MATLAB	MATrix LABoratory
MDC	Multistage Depressed Collector
MIG	Magnetron Injection Gun
MPS	Modular Power Supply
PCB	Printed Circuit Board
PSU	Power Supply Unit
QO	Quasi-Optical
SC	Super Conducting
SDC	Singlestage Depressed Collector
SEE	Secondary Electron Emission
SMF	Stray Magnetic Field
SP	Short-Pulse
TE	Transverse Electric
TEM	Transverse Electro-Magnetic
TM	Transverse Magnetic
TMFS	Transverse Magnetic Field Sweeping
TWT	Travelling Wave Tube
W7-X	Wendelstein 7-X
WEST	Tungsten (chemical symbol "W") Environment in Steady-state Tokamak

Symbols

α_p	pitch factor
β	angle of a magnetic field line
ΔT	temperature difference
$\Delta z_\mathrm{b,col}$	electron beam thickness on the axial collector wall
γ	Lorentz factor
μ_0	vacuum permeability
$\partial\Sigma$	boundary curve
Σ	surface
τ	short time interval
θ_helix	azimuthal coverage angle of the helical surface
θ_over	azimuthal overlap angle of the helical surface
θ_straight	azimuthal coverage angle of the straight cut
ϑ	angle between electric and magnetic field
$\vec{\nabla}$	nabla operator as vector
$\vec{d}$	distance vector
$\vec{v_\mathrm{d}}$	drift velocity vector
A	infinitesimal element vector of the surface Σ
d_coil	thickness of coil core

D_d	drift distance
d_helix	depth of the helical surface
e	(positive) elementary charge
f_c	electron cyclotron frequency
h_ExB	height of the $\vec{E}\times\vec{B}$ drift region
h_helix	axial distance of the helical gap
h_straight	height bottom straight cut
h	height of coil core
i	index variable
j	index variable
l	infinitesimal element vector of the surface $\partial\Sigma$
m_e	electron rest mass
m	number of electrodes
n	number of periods
p	number of unique potentials
T	period length
t	time
v_0	electron velocity at collector entrance
V_coil	volume of coil core
$v_\parallel$	longitudinal component of velocity
$v_\perp$	transverse component of velocity
z_ExB	initial axial position of the $\vec{E}\times\vec{B}$ drift region

Voltages and Potentials

ΔU	potential difference
Φ_0	amplitude of the electric potential
Φ_{dep}	depression potential
Φ_{max}	maximum electric potential
Φ	electric potential
$U_{1,\mathrm{a}}$	PSU voltage without depressed collector
$U_{1,\mathrm{b}}$	PSU voltage 1 for SDC
$U_{1,\mathrm{c}}$	PSU voltage 1 for MDC
$U_{2,\mathrm{b}}$	PSU voltage 2 for SDC
$U_{2,\mathrm{c}}$	PSU voltage 2 for MDC
$U_{3,\mathrm{c}}$	PSU voltage 3 for MDC
U_{acc}	acceleration voltage at the electron gun
U_{dec1}	deceleration voltage of first stage of MDC
U_{dec2}	deceleration voltage of second stage of MDC
U_{dec}	deceleration voltage of SDC

Electric Field

$\vec{E}_{\parallel}$	parallel electric field
$\vec{E}_{\perp}$	transverse electric field
$\vec{E}$	electric field vector
E_{θ}	azimuthal electric field component
$E_{\max}$	maximum electric field
E_{r}	radial electric field component
E_{z}	axial electric field component
E	electric field

Magnetic Field

$\vec{B}$	magnetic field vector
$\vec{m}$	magnetic moment vector
B_{θ}	azimuthal magnetic field component
$B_{\mathrm{r,col}}$	radial magnetic field in the collector
B_{r}	radial magnetic field component
$B_{\mathrm{z,col}}$	axial magnetic field in the collector
$B_{\mathrm{z,cvt}}$	axial magnetic field in the cavity
B_{z}	axial magnetic field component
B	magnetic field
m_{z}	axial component of the magnetic moment

Currents

I_{a}	body current without depressed collector
I_{b}	body current of SDC
I_{col1}	collector current of first stage of MDC
I_{col2}	collector current of second stage of MDC
I_{col}	collector current of SDC
I_{c}	body current of MDC
I_{gun}	current at the electron gun

Power

P_{acc}	power of the accelerated electron beam
P_{dec}	power the decelerated electrons
P_{MDC}	power demand of MDC PSU
P_{output}	output power of the electromagnetic wave
$P_{\mathrm{recovered}}$	recovered power of a depressed collector
P_{RF}	power of the electromagnetic wave after the cavity
P_{Sbeam}	power of the spent electron beam
P_{SDC}	power demand of SDC PSU

Efficiency

η_{col}	collector efficiency
η_{int}	interaction efficiency
η_{RF}	efficiency of the QO system
η_{total}	overall (total) gyrotron efficiency

Radii

$\Delta r_{\mathrm{b,col}}$	electron beam thickness in the collector
$\Delta r_{\mathrm{b,cvt}}$	electron beam thickness in the cavity
Δr_{b}	electron beam thickness
Δr_{gc}	guiding center radius spread
Δr	maximum radial drift distance
r_0	radial position at a reference position
$r_{\mathrm{gc,col}}$	guiding center radius in the collector
$r_{\mathrm{gc,cvt}}$	guiding center radius in the cavity
r_{gc}	guiding center radius
r_{in}	Inner radius of coil core
r_{L}	Larmor radius
R	inner collector or electrode radius

Coordinates

$\dot{\theta}$	azimuthal derivative
θ	azimuthal cylindrical coordinate
$\vec{\theta}$	azimuthal vector
$\vec{r}$	radial vector
$\vec{z}$	axial vector
r	radial cylindrical coordinate
u	first surface variable
v	second surface variable
x	transverse Cartesian coordinate
y	transverse Cartesian coordinate
z	axial Cartesian or cylindrical coordinate

1 Introduction

The necessity for alternative sources of electrical power to meet the growing energy needs and to facilitate a transition away from fossil fuels is evident. The new generation of power plants must be capable of independent operation, regardless of the time of day, weather conditions, and fuel supplies from other countries. Furthermore, the generation of radioactive waste and the pollution of the environment by further emissions of greenhouse gases must be avoided. The most promising solution for such a power plant is the fusion of light atoms.

The fusion reaction is omnipresent in the universe, both in our Sun and other stars. Nevertheless, it is not a simple matter to utilize it in a controlled manner on Earth. In order for the fusion process to occur, the kinetic energy of the atoms must be sufficiently high to overcome the Coulomb barrier, which is the point at which the strong nuclear force of attraction is larger than the electromagnetic force of repulsion. On a macroscopic scale, the kinetic energy is observed as the temperature of an object. The temperature required for a fusion process is significantly above the ionization energy at which atoms are separated into their electrically charged nuclei and electrons, which is known as the plasma state.

Fusion research has been ongoing for several decades, during which significant progress has been made in understanding the physics of fusion and in developing the technologies needed to achieve fusion power. The research for future large-scale fusion power plants focuses on the magnetically confined plasma using the tokamak and stellarator concepts. The tokamak is the most advanced reactor concept. A toroidal magnetic field is applied to confine the plasma, while a solenoidal magnetic field is utilized to generate the current required to maintain the plasma. The stellarator is the second type of fusion reactor where complex magnetic fields are applied to confine the plasma. Stellarators do not need the plasma current to maintaining a stable plasma for long periods of time, whereas tokamaks are pulsed power plants [1].

The fusion reaction with the highest nuclear cross-section, indicating the probability of a fusion reaction, is the fusion of Deuterium and Tritium, with a high energy of 17.6 MeV released in each fusion reaction. However, the maximum plasma pressure acceptable for magnetic confinement is very limited. To achieve a stable plasma operation at such limited pressures with the fusion reaction of Deuterium and Tritium, a plasma temperature above 100 million Kelvin is needed. The plasma in a fusion reactor must be heated during the start-up and stabilized during operation. Various methods are known for heating, such as resistive heating, Neutral Beam Injection (NBI) and heating with electromagnetic waves. The later can be implemented in the form of Ion Cyclotron Resonance Heating (ICRH) at tens of MHz, in the form of Lower Hybrid Resonance Heating (LHRH) at a few GHz, or in the form of Electron Cyclotron Resonance Heating (ECRH) between 100 GHz to 300 GHz. The advantage of an ECRH system, in addition to the ability to control the plasma temperature, is the control of the plasma density, which is crucial for achieving and maintaining a stable fusion reaction. The penetration of high-power microwaves into the plasma enables uniform heating, which in turn reduces the likelihood of plasma instabilities that can damage the reactor walls and reduce the efficiency of the fusion process.

Gyrotrons are the only known sources capable of generating the high-frequency millimeter waves in the sub-THz regime required for ECRH and plasma stabilization with a power of several megawatts. The energy of the electromagnetic wave generated by a vacuum electron tube, such as a gyrotron, is close to the electron cyclotron resonance frequency [2]. This is in contrast to traditional vacuum electron tubes, for which the wavelength of the electromagnetic wave is directly related to the cavity size.

Already in today's experimental devices, such as Wendelstein 7-X (W7-X) and ITER, a combination of multiple gyrotrons is necessary to achieve the required ECRH power inside the plasma vessel. At W7-X, in total 10 gyrotrons are installed to provide 7.5 MW of ECRH power to the plasma. With a future upgrade of the gyrotrons up to 18 MW [3]. For ITER it is planned to operate in total 24 gyrotrons with an individual tube output power of 1 MW [4, 5]. It is currently under discussion to increase the number of gyrotrons for ITER to even higher numbers in order to provide more ECRH power to the plasma. Those gyrotrons are equipped with Singlestage Depressed Collectors (SDCs) to achieve an overall tube efficiency of around 50 %. Future facilities that are

increased in size to represent the feasibility of a fusion power plant, like the DEMOnstration power plant (DEMO), will require more ECRH power than the systems build today. The overall tube efficiency of today is acceptable for smaller test facilities with lower ECRH power and shorter operation times as the energy usage is limited. However, a high tube efficiency will be important for higher power levels and longer operation times.

1.1 Motivation

The future DEMO will be the first fusion power plant to feed electricity into the grid with a net power of 500 MW [6]. The net power fed into the electric grid of a fusion power plant is directly dependent on the efficiency of the overall plant. Consequently, an increase in efficiency of the supplementary components is highly demanded to increase the overall efficiency. The plasma vessel of DEMO is planned to be a tokamak with gyrotrons as the source of the ECRH system. The fusion power of DEMO could be in the range of 2 GW [7], while in the current layout for the ECRH system, a total of 108 gyrotrons are planned [8]. The maximum output power of a single gyrotron in Continuous Wave (CW) operation is currently in the range of 1 MW to 2 MW, further increasing the total output power of the ECRH system for DEMO. At such power levels, it is mandatory to achieve a high gyrotron efficiency in order to reduce the electrical power required for the operation of the power plant during CW operation.

Increasing the overall tube efficiency from 50 % to 60 % will reduce the electrical input power of a 100 MW ECRH system by about 34 MW. The electrical output power of a whole DEMO sized power plant to the grid will be increased by over 6 % with an ECRH system equipped with Multistage Depressed Collector (MDC) gyrotrons. Considering the expected energy generation cost of a fusion power plant beyond 2040 in a competitive scenario of \$80/(MW h) to \$100/(MW h) [9] this would result in a yearly saving of \$24 million/a to \$30 million/a. Hence, the objective of this work is the development and implementation of a new novel MDC to significantly increase the gyrotron efficiency.

1.2 Gyrotron - Operation Principle and Main Components

A gyrotron is a high-power vacuum electron tube oscillating at microwave frequencies [2]. Gyrotrons are useful in a wide range of applications, such as fusion energy research, particle accelerators, and radar systems [10–12]. The interaction of the electrons with the electromagnetic wave in the gyrotron is based on the principle of the electron cyclotron resonance. It occurs when a charged particle, such as an electron, moves in a magnetic field at a frequency close to the cyclotron frequency of the particle or a multiple of it in case of harmonic operation. The relativistic electron cyclotron frequency is calculated when the Lorentz force equation is set equal to the equation of the centripetal force of an electron in a magnetic field and is given by [2]

$$f_\mathrm{c} = \frac{e\,B}{2\,\pi\,\gamma\,m_\mathrm{e}} \tag{1.1}$$

where e is the electrical charge of the electron, B is the amplitude of the magnetic field, γ is the Lorentz factor and m_e is the electron mass.

In a gyrotron, as shown schematically in Fig. 1.1, the electrons are emitted by an electron gun, a Magnetron Injection Gun (MIG) and accelerated to relativistic velocities by a strong electric field. The MIG consists of a cathode at a negative potential where the electrons are emitted at an emitter ring and the anode at a positive or Ground Potential (GND) potential. The potential of the anode is defined as the body potential of the gyrotron. In the system just described, a diode-type MIG is used to provide the baseline for a gyrotron. However, more degrees of freedom during gyrotron operation can be achieved by the implementation of a triode-type MIG with an additional modulation anode [14]. The emitter ring and the cathode of a traditional MIG, either of diode- or triode-type, are placed at an inner structure inside the gyrotron, while the anode is placed at the outer wall of the tube as shown in Fig. 1.1. The emitter ring is limited in size by the maximum acceptable dimension of the outer gyrotron diameter that fits to the superconducting magnet. A new compact inverse MIG was developed at Karlsruhe Institute of Technology (KIT) with the cathode and emitter ring at the outer wall of the gyrotron and the anode at the inside [15].

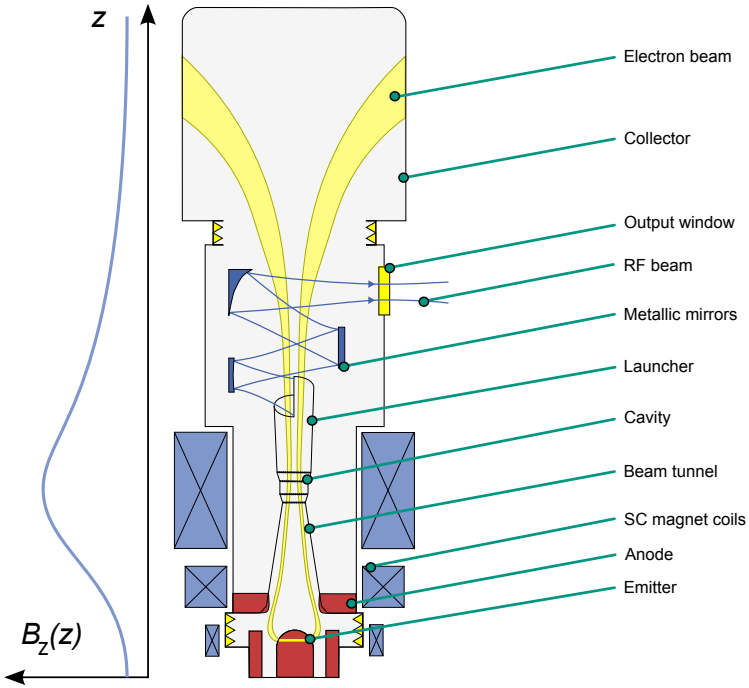

Figure 1.1: Magnetic profile along the axis (left) and schematic of a gyrotron (right) [13].

A 16.8 % larger emitter compared to the currently used conventional MIG was achieved in the design for the first prototype [16].

After acceleration, the electrons are guided by an externally applied magnetic field in a helical orbit along the magnetic field lines. Hence, it follows a helical trajectory that is a combination of a transverse component of velocity $v_\perp$ and longitudinal component of velocity $v_\parallel$. The ratio between both velocity components is defined as the pitch factor α_p

$$\alpha_\mathrm{p} = \frac{v_\perp}{v_\parallel} \tag{1.2}$$

The slope of a helical electron trajectory is described by this pitch factor. A large pitch factor (small $v_\parallel$) produces a flat helical slope, while a small pitch

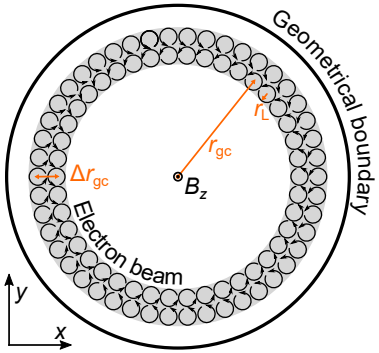

Figure 1.2: Axial cross-section of the axis-symmetric hollow cylindrical electron beam as used in a gyrotron (deviated from [18]).

factor (high $v_{\parallel}$) produces a steep slope. The design and operation parameters of the MIG are responsible for a desired α_{p} in the range of $\alpha_{\mathrm{p}} \approx 1.0$ to 1.4 [17]. A current of individual electrons on helical trajectories is arranged in the form of an axis-symmetric hollow cylindrical electron beam as shown in Fig. 1.2. B_{z} is the axial magnetic field, r_{L} is the Larmor radius, r_{gc} is the guiding center radius of an individual electron, x and y are the transverse Cartesian coordinates. The thickness Δr_{b} of such an annular electron beam is defined by the spread of the guiding center radius Δr_{gc}

$$\Delta r_{\mathrm{b}} = \Delta r_{\mathrm{gc}} + 2\, r_{\mathrm{L}} \tag{1.3}$$

After the electron beam is generated at the MIG, it is guided through the beam tunnel to the cavity. The externally applied magnetic field is compressed along the path of the electron beam to the cavity where the maximum magnetic field strength is reached. Several Tesla of magnetic field flux are generated by a Super Conducting (SC) magnet which is placed around the gyrotron cavity. In addition to the main coils, such a magnet contains several other coils to generate an appropriate magnetic field profile, especially important for the MIG operation. The gyrotron is usually supported by the top plate of the SC magnet.

The kinetic energy of the electron beam is converted to electromagnetic energy inside the cavity. Gyrotrons are unique compared to conventional vacuum

electronic devices such as magnetrons, klystrons, and Travelling Wave Tubes (TWTs). All of those have structures that are smaller than the size of the wavelength. A gyrotron, on the other hand, is operated with higher order electromagnetic modes in the cavity, increasing the cavity dimension. This larger size enhances the capability for the cavity cooling system which is limited to a maximum wall loading of 2 kW/cm^2 [19]. Moreover, the higher order electromagnetic modes are essential for decreased magnetic fields at the metallic boundary. Surface currents, which are induced by the oscillating magnetic fields at the cavity boundary, are reduced with decreased magnetic fields.

An electromagnetic field in a waveguide can be expanded into Transverse Electric (TE), Transverse Magnetic (TM) and Transverse Electro-Magnetic (TEM) modes [20]. Only the electric field is transverse to the propagation direction for TE modes, while it is the magnetic field for TM modes. For TEM modes, both field components are transverse to the propagation direction as for a plane wave at free space. A $TE_{34,19}$ mode is shown as an example for a high order mode in Fig. 1.3 as it is used for interaction with the electron beam in the KIT 2 MW 170 GHz coaxial-cavity gyrotron. The interaction of the electron beam with the desired TE mode requires a beam radius r_{gc} which corresponds approximately to the radius of maximum electric field of the TE mode for efficient energy conversion. In the cavity, the electrons are bunched and interact with the transverse electric field. The energy converted to the TE mode is provided only by the electron transverse velocity component $v_{\perp}$. The longitudinal component of velocity $v_{\parallel}$ of the electrons does not interact with the TE mode however, $v_{\parallel}$ is important to avoid trapped electrons and reflections on magnetic mirrors [21]. The interaction mechanism between electron beam and electromagnetic wave is described in detail in [2, 22, 23].

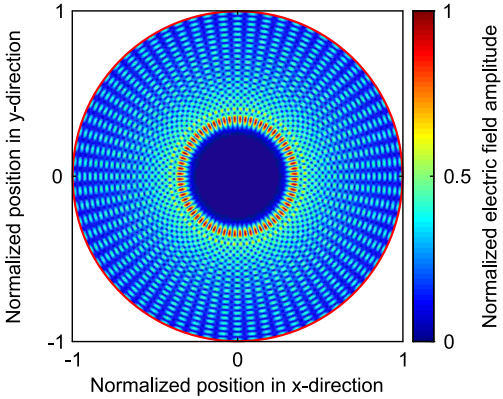

Figure 1.3: $TE_{34,19}$ mode as used in the KIT 2 MW 170 GHz coaxial-cavity gyrotron.

1.3 Gyrotron - Efficiency

In a gyrotron, electrons are guided along magnetic field lines, enabling efficient energy conversion with the electromagnetic wave in the cavity. Gyrotrons achieve approximately 35 % interaction efficiency in converting electron beam energy into electromagnetic energy. The interaction efficiency η_{int} is defined as

$$\eta_{\mathrm{int}} = \frac{P_{\mathrm{RF}}}{P_{\mathrm{acc}}} = 1 - \frac{P_{\mathrm{Sbeam}}}{P_{\mathrm{acc}}} \tag{1.4}$$

with the generated power of the electromagnetic field P_{RF}, the power of the accelerated electron beam before interaction P_{acc} and the power of the spent electron beam after interaction P_{Sbeam}. Hence, the power of the spent electron beam is defined as

$$P_{\mathrm{Sbeam}} = P_{\mathrm{acc}} - P_{\mathrm{RF}} = P_{\mathrm{acc}}\,\eta_{\mathrm{int}} \tag{1.5}$$

where η_{int} is the interaction efficiency. The electromagnetic wave in the form of a TE mode in the cavity is coupled out of the gyrotron by a quasi-optical system. This quasi-optical system converts the TE mode to a Gaussian mode

by the launcher and the metallic mirrors in the mirror-box before it is ejected from the gyrotron through an output window as shown in Fig. 1.1 [24]. The efficiency of the transformation of the electromagnetic wave in the gyrotron η_{RF} is estimated to $> 90\,\%$ due to losses to stray radiation (1.75 % of the quasi-optical system, less than 0.09 % at the window) and ohmic losses in the launcher (2.56 %) [25] and After Cavity Interaction (ACI) (5 %) [26]. The output power P_{output} of a gyrotron is calculated to

$$P_{\mathrm{output}} = P_{\mathrm{acc}}\,\eta_{\mathrm{int}}\,\eta_{\mathrm{RF}} \tag{1.6}$$

The spent electron beam is collected by a collector, which is located above the mirror-box as shown in Fig. 1.1. A depression potential can be applied to the input of the collector, which slows down the electron beam and allows power to be recovered. The collector efficiency η_{col} is defined as

$$\eta_{\mathrm{col}} = \frac{P_{\mathrm{recovered}}}{P_{\mathrm{Sbeam}}} = 1 - \frac{P_{\mathrm{dec}}}{P_{\mathrm{Sbeam}}} \tag{1.7}$$

with the recovered power $P_{\mathrm{recovered}}$. The alternative definition of the collector efficiency η_{col} is given with the power of the decelerated electrons P_{dec} when they intersect with a boundary like the collector wall. The efficiency of an SDC is typically in the range of 60 % [27] for a total gyrotron efficiency of approximately 50 %, while it is increased for a two stage MDC to 70 % to 80 % for a total gyrotron efficiency around 60 %. Gyrotron collectors are presented in more detail in section 1.4. The overall gyrotron efficiency η_{total} is calculated as [18]

$$\eta_{\mathrm{total}} = \frac{P_{\mathrm{output}}}{P_{\mathrm{acc}} - P_{\mathrm{recovered}}} = \frac{\eta_{\mathrm{int}}\,\eta_{\mathrm{RF}}}{1 - (1 - \eta_{\mathrm{int}})\,\eta_{\mathrm{col}}} \tag{1.8}$$

The visual representation of equation 1.8 is shown in Fig. 1.4 for $\eta_{\mathrm{RF}} = 90\,\%$. An increase of the total gyrotron efficiency can be achieved by an increased interaction or collector efficiency. However, the interaction efficiency of a high-power gyrotron is limited to approximately 35 % due to the interaction of the electromagnetic wave with the transverse component of the electron velocity. An increase in the collector efficiency is a more promising alternative.

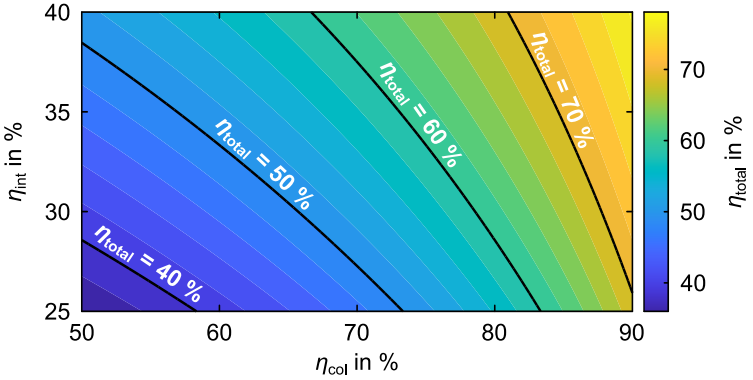

Figure 1.4: Relation of η_{int}, η_{col} and η_{total} for $\eta_{\mathrm{RF}} = 90\,\%$

The calculation of a plug-in efficiency of the overall gyrotron would require additional consideration of the efficiency of the high voltage Power Supply Unit (PSU), the power demands for the cooling system.

1.4 Basic Considerations for Gyrotron Collectors

In the collector, a high thermal load is observed due to the deposition of the electron beam after interaction. As the interaction efficiency is limited to around 35 %, most of the beam power remains after interaction. This spent beam is then collected on the inner surface of the collector, which must be designed to handle the resulting high thermal loads from the electron beam power. To withstand the thermal load, the collector is made out of oxygen free copper, as this material has a high thermal and electrical conductivity. Oxygen free copper is well studied and verified for the use in different kinds of vacuum electronic tubes however, especially pure copper [28] is limited in its mechanical stability at high temperatures where other copper alloys like GLIDCOP [29] and Copper-Chromium-Zirconium (CuCr1Zr) [30] show superior performance and are being used in an increasing number of devices.

The high-power loading density is a combination of the high absolute power of the spent electron beam in combination with a small impact area. In the

specific case of an azimuthal magnetic field component $B_\theta = 0$, the impact area of the electron beam on the collector wall can be estimated by applying Bush's theorem [31]

$$\dot{\theta} = -\frac{e}{2\,m_\mathrm{e}} \left(B_\mathrm{z,col} - B_\mathrm{z,cvt} \frac{{\Delta r_\mathrm{b,cvt}}^2}{{\Delta r_\mathrm{b,col}}^2} \right) \tag{1.9}$$

$B_\mathrm{z,col}$ and $B_\mathrm{z,cvt}$ are the axial magnetic field components in the collector and the cavity, respectively. The radial positions in the approximate form of Bush's theorem [31] are replaced by the thicknesses of the annular electron beam $\Delta r_\mathrm{b,col}$ and $\Delta r_\mathrm{b,cvt}$ in the collector and the cavity, respectively. Under the assumption that the azimuthal movement of the electrons vanishes ($\dot{\theta} = 0$), the equation 1.9 can be simplified to

$$\Delta r_\mathrm{b,col} = \sqrt{\frac{B_\mathrm{z,cvt}}{B_\mathrm{z,col}}}\, \Delta r_\mathrm{b,cvt} \tag{1.10}$$

The angle β of the electron beam at the collector wall is important for the further estimation of the size of the impact area and is calculated based on the angle of the magnetic field lines with basic trigonometric function

$$\beta = \tan^{-1} \frac{B_\mathrm{r,col}}{B_\mathrm{z,col}} \tag{1.11}$$

with the radial magnetic field component in the collector $B_\mathrm{r,col}$. The thickness of the electron beam on the collector wall $\Delta z_\mathrm{b,col}$ is then calculated to

$$\Delta z_\mathrm{b,col} = \sqrt{\frac{B_\mathrm{z,cvt}}{B_\mathrm{z,col}}}\, \frac{\Delta r_\mathrm{b,cvt}}{\sin\beta} \tag{1.12}$$

The surface area of the intersection region between the electron beam and the collector wall is calculated by the product between $\Delta z_\mathrm{b,col}$ and the inner circumference of the cylindrical collector. In order to enhance the surface area and to decrease the short-term power loading density, it is possible to increase the collector radius and reduce the angle of the electron beam at the collector

wall, respectively. As the radius of the collector is increased, the thickness of the electron beam is also increased due to the reduced magnetic field required to expand the electron beam to the larger radius.

1.4.1 Energy Recuperation

The power of the spent electron beam is reduced by applying a depression voltage. The depression voltage in current European Union (EU) gyrotron designs is either applied with a small insulator at the bottom of the gyrotron, directly after the anode of the MIG, or with a large insulator between the mirror-box and the collector. The first potential concept is used in the W7-X gyrotrons in which case the internal decelerating electric field is observed from the spent beam electrons at the entrance of the mirror-box [32]. The second concept is used in the KIT 2 MW 170 GHz coaxial-cavity gyrotron [33], and competitors [34, 35], where the deceleration takes place later at the entrance of the collector. During deceleration part of the kinetic energy of the electrons is transformed to potential energy. The thermal load on the collector wall is reduced with the reduction of the kinetic energy of the electrons while the overall gyrotron efficiency is increased.

Conventional depressed collectors utilize a single depression voltage and were first used in the 1990s [27, 34, 35]. A schematic representation of a gyrotron with an SDC is shown in Fig. 1.5a including the connection to the PSU. The SDC works in a classical voltage operation scheme, where a negative potential is applied at the cathode, a positive at the anode (gyrotron body) and the collector is set to ground potential. It results in a reduced voltage for the cathode PSU for the identical acceleration voltage. The difference between the acceleration voltage and the voltage of the cathode PSU is compensated by the body PSU, which does supply little to no current to the gyrotron and thus no power. From a physical point of view, it is equivalent to an operation of the gyrotron with a body potential at GND and a collector potential at a negative potential. However, the PSU of the collector would be either operated as a sink or a modular PSU would be required. The idea of a modular PSU will be briefly presented in section 1.5 and discussed in more detail in section 2.1.

In an ideal MIG, all electrons have the same kinetic energy after acceleration if neglecting the velocity spread at the emitter. In a realistic gyrotron, the

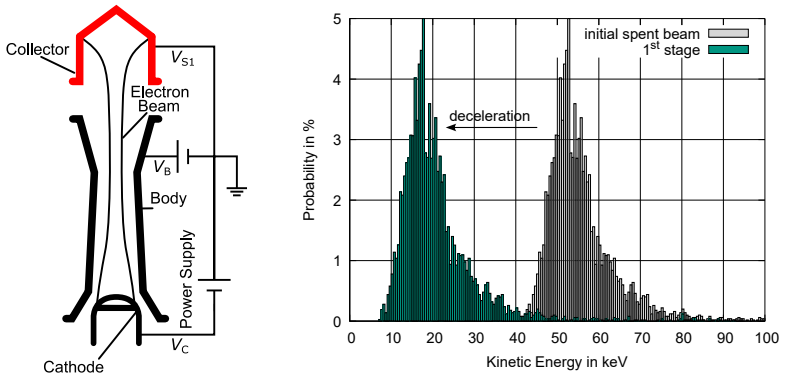

(a) Potentials **(b)** Energy distribution

Figure 1.5: Schematic view of an SDC with the electric potential connection to the PSU (left) (deviated from [36]) and energy distribution of the spent electron beam before and after deceleration in the SDC (right).

energy spectrum is broadened due to a variation in the electron velocities. The interaction with the electric field in the cavity results in a widened energy distribution in the spent electron beam, as shown in Fig. 1.5b. The maximum deceleration potential that can be applied is limited by the slowest electron, while an increase would cause reflections that have a negative influence on the gyrotron operation. The limitation of the deceleration potential and the widely spread energy distribution lead to a limitation of the collector efficiency. The increased efficiency of an SDC over the non-depressed operation reduces the power loading on the inner collector wall due to less power in the spent electron beam. The reliability and lifetime of the collector are improved. However, a significant power is still maintained in the decelerated spent electron beam and transformed a thermal load at a limited surface area. The impact area of the electron beam with the collector wall must be increased to further decrease the power loading density for Long-Pulse (LP) and CW operation.

1.4.2 Reduction of Thermal Wall Loading

The two aspects of management and dissipation of the high-power loading on the inner collector surface are presented in this subsection. The management of high-power loading density is addressed with the implementation of an electron

beam sweeping system to increase the impact area of the electron beam with the collector wall for decreased time averaged power loading density. The dissipation of the high-power loading is addressed with a specific cooling system for the collector as described in the following section.

Increase of the Impact Area by Electron Beam Sweeping

In today's high-power gyrotrons, two different techniques are used to sweep the magnetic field:

- Longitudinal Magnetic Field Sweeping (LMFS), where the electron beam is moved axially [32, 37]
- Transverse Magnetic Field Sweeping (TMFS), where the electron beam is tilted on the inner collector wall and rotated in the azimuthal direction [38–40]

Schematic representations of the LMFS and the TMFS are shown in Fig. 1.6a on the left and right, respectively. The upper and lower limits for both systems are indicated by dotted red circles.

Longitudinal Magnetic Field Sweeping

The axial movement of the electron beam in the LMFS is achieved by a periodic variation of the axial magnetic field component in the collector region. This magnetic field is generated by cylindrical coil(s) around the copper wall of the collector. Such a setup is similar to a transformer with the secondary winding represented by that copper wall. It is observed as a shorted single turn coil with the induced currents referred to as eddy currents. They are increased with the sweeping frequency and have a shielding effect on the magnetic field inside the collector. At a sweeping frequency of 7 Hz, the attenuation of the magnetic field is more than 80 % [38]. The sweeping frequency of the LMFS coils is therefore limited to approximately 10 Hz due to the high eddy currents generated in the highly conductive copper collector.

The electron beam movement on the collector wall is influenced by the sweeping frequency and sweeping function. A sinusoidal current is typically applied

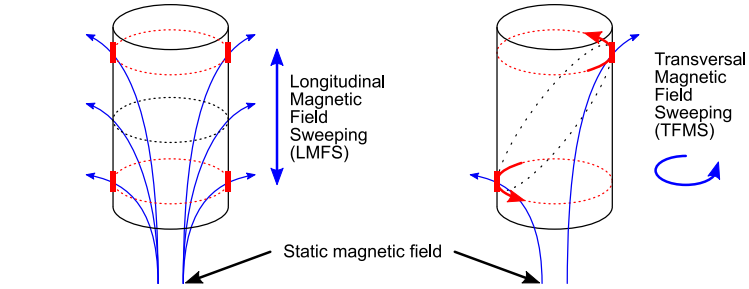

(a) LMFS (left) and TMFS (right) (deviated from [40])

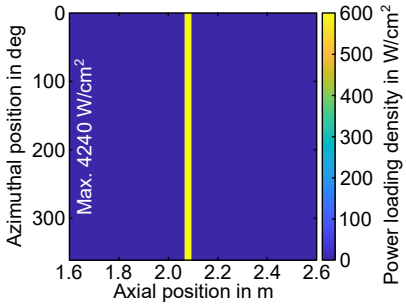

(b) LMFS Snapshot

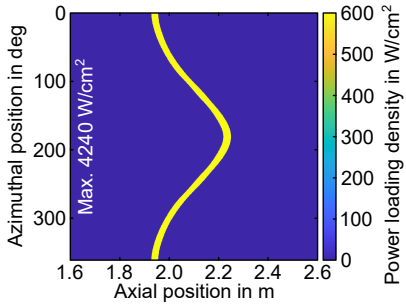

(c) TMFS snapshot

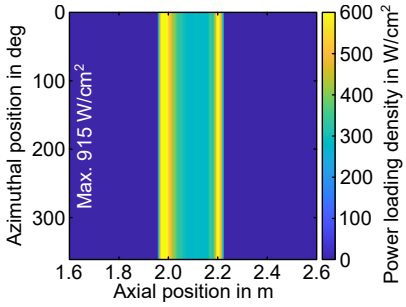

(d) LMFS time average

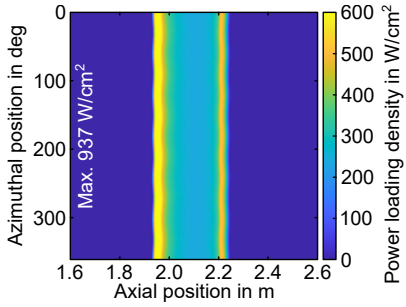

(e) TMFS time average

Figure 1.6: Magnetic field sweeping systems used in gyrotrons with LMFS (a left) and TMFS (a right) (deviated from [40]). Snapshots of the electron beam intersection with the collector wall for LMFS (b) and TMFS (c) as well as time average collector wall loading for LMFS (d) and TMFS (e).

to the LMFS coil(s), while advanced sweeping functions such as triangular waveforms are also possible [41]. However, higher frequency components are introduced with advanced sweeping functions, as can be demonstrated by the Fourier transformation. Those higher frequency components are more influenced by the shielding effect of eddy currents, reducing their efficiency of reduced time spent by the electron beam at the hotspot positions.

A snapshot of the collector wall loading with only LMFS is shown in Fig. 1.6b with the axial position on the x-axis, the azimuthal position on the y-axis, and the power loading density as color information. The electron beam is distributed on a thin line with a constant axial position and a power loading density of 4240 W/cm^2. The integrated collector wall loading, as shown in Fig. 1.6d, is achieved with a simple sinusoidal sweeping current and the axial movement of the electron beam. Hot spots are visible at the upper and lower turning points due to the reduced speed of the sinusoidal sweeping function at those positions with a maximum power loading density of 915 W/cm^2. Such behavior can be improved with advanced sweep functions for a reduction of the thermal stress. In addition to time varying current, constant current can be used in the LMFS to decrease or increase the axial position of the electron-wall intersection area.

Transverse Magnetic Field Sweeping

The tilt and rotation of the electron beam in the collector by application of the TMFS is achieved with a radial magnetic field at the entrance of the collector [42]. Typically, it is implemented by a set of six coils to drive the coils with simple transformers connected to a three-phase current. The coils of the TMFS system are arranged around an additional stainless steel section below the copper collector, which reduces the shielding effect of eddy currents, thus allowing a higher sweep frequency. However, the less conductive stainless steel section still generates eddy currents with an estimated magnetic field attenuation of 20 % at a sweeping frequency of 50 Hz [38].

A snapshot of the collector wall loading with only TMFS is shown in Fig. 1.6c. The electron beam is distributed on a thin line with a variation in axial position due to the tilted electron beam and a power loading density of 4240 W/cm^2 is obtained.The integrated collector wall loading, as shown in Fig. 1.6e, is

achieved with sinusoidal currents in all six coils with an offset in the phase of 60° between neighboring coils. The homogeneous rotation of the tilted electron beam at the collector wall is the optimal motion due to the constant sweeping speed of the electron beam over the collector wall. However, the angle of the electron beam on the collector wall is steeper for lower axial positions, increasing the thermal loading. In this example, the maximum power loading density of the time averaged wall loading is at 937 W/cm^2, similar to the LMFS itself.

Combination of Both Sweeping Systems

Both sweeping methods are equipped with water-cooled normal-conducting coils with a resistance loss of several kilowatts. The structure of an SDC with both the copper electrode and the stainless steel section is shown in Fig. 1.7a without any cooling system or collector coils. The SDC of the ITER gyrotron is shown in Fig. 1.7b. The TMFS coils are visible at the entrance of the collector. The water cooling jacket is located below the LMFS coil with a black layer of lead on the outside for shielding from X-rays. The integrated collector wall loading of the combined LMFS and TMFS system is shown in Fig. 1.7c. It is important to note that the maximum power loading density with the combination of both sweeping systems is successfully reduced to less than 500 W/cm^2 from originally more than 4000 W/cm^2. The pattern in the wall loading is a result of a simplified simulation setup for a reduced calculation time. In simulation, the frequencies of the sweeping systems are set to 7 Hz and 49 Hz instead of 7 Hz and 50 Hz for the LMFS and TMFS, respectively. This way, only $1/7$ s of the sweeping had to be calculated instead of 1 s.

Concepts for Active Cooling of Collectors

A high-power is deposited at the inner surface of the collector wall. In Short-Pulse (SP) operation, a cooling is not required due to the low total energy transferred as heat to the collector material. However, a collector cooling must be considered for LP operation and must be significantly improved towards CW operation. The simplest characterization of a cooling system is with the heat transfer coefficient between the heated material and the cooling medium. Air-free convection, as used for SP operation, has a heat transfer coefficient of

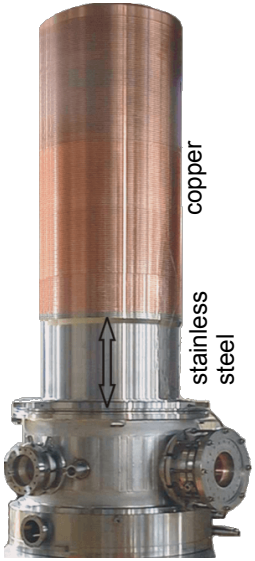

(a) Collector structure

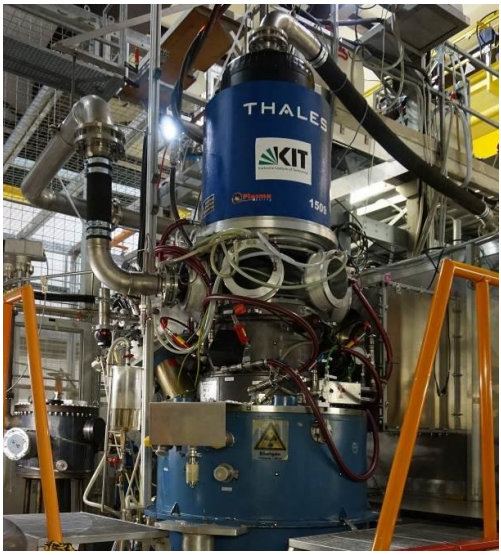

(b) Complete collector system

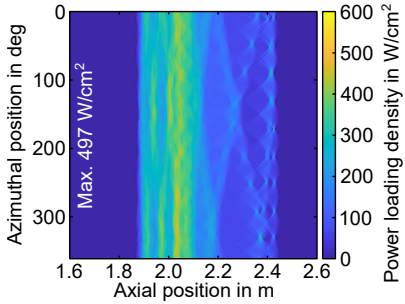

(c) Time average collector wall loading

Figure 1.7: (a) Structure of an SDC without the cooling jacket and sweeping systems [43]. (b) Completely assembled gyrotron with SDC ready for CW operation [44]. (c) Time average collector wall loading of the combined LMFS and TMFS system.

up to 0.0028 W/cm^{2}K, while single phase water forced convection, as used for LP operation, is between 0.027 W/cm^{2}K to 1.14 W/cm^{2}K and cooling systems with boiling water are between 0.27 W/cm^{2}K to 5.7 W/cm^{2}K [45]. One of the candidates with boiling water is the HyperVapotron (HV) cooling [46, 47] with corrugations on the outside of the high heat flux surface where the spent electron beam is collected. In the corrugations, the liquid is heated until it vaporizes, is extracted from the corrugation and condenses. The resulting void is wetted with new sub-cooled liquid and the cycle starts again. The HV cooling is used in the Thales gyrotron collectors for W7-X and ITER.

The maximum thermal loading at the inner surface of a collector wall with HV cooling is considered to be 500 W/cm^2 if a magnetic field sweeping system is implemented at the same time [48]. Two factors are responsible for this limitation:

- The maximum heat flux which can be removed by the cooling method. It is the product of the heat transfer coefficient with an allowed difference between the average temperature of the heated surface and the cooling medium. This point is not addressed in this work.
- The maximum temperature of the heated surface due to the relatively slow frequencies of the magnetic field sweeping systems. A proposal to reduce the maximum temperature by a new sweeping method is given in chapter 5.

If gyrotrons with even higher output power are to be built and the current cooling systems are to be used, only two options are possible to keep the maximum thermal loading constant:

- The collector must become larger to provide more surface area.
- The efficiency of the collector must increase.

The inner collector radius of the EU 1 MW CW gyrotron for ITER as well as of the 1.5 MW W7-X upgrade gyrotron is at 225 mm [49]. Today's SDC for the CW KIT 2 MW 170 GHz coaxial-cavity gyrotron has an inner radius of 300 mm [39], whereas an SDC of a 4 MW gyrotron would require an inner collector radius of 400 mm with today's technology [50]. The approach of an increased collector efficiency is discussed in more detail in section 1.5.

1.4.3 Influences of Stray Magnetic Fields on Gyrotron Operation

The sources of a Stray Magnetic Field (SMF) range from ferromagnetic structures nearby the gyrotron magnet to neighboring gyrotrons in ECRH systems, the fusion plasma vessel in form of the tokamak and even the earth magnetic field. The following subsections will present the gathering of data in form of calculation and measurement of SMFs as well as the influence and fundamental challenges in gyrotron collector operation. In analyses performed on EU gyrotron configurations for ITER, it is shown that the collector is the most sensitive component when SMFs are introduced to the gyrotron environment [51, 52]. The reason for this sensitivity lies in the weak magnetic field present in the collector and not in any interaction with the electromagnetic wave. The disturbance may simply cause the electron beam to strike parts that are not designed for high loads or are not sufficiently cooled.

Calculation of Stray Magnetic Fields

The first step in the simulation of SMF influences to the gyrotron operation lies in the calculation of the magnetic field itself. Different methods and approximations can be utilized to get the magnetic field of field sources close to and from far away. The most accurate calculation of the magnetic field is done by applying Maxwell's equations directly, or alternatively by application of the Biot-Savart law for magnetostatic calculations [53]. The in-house software Ariadne uses an extrapolation of the magnetic field from the axis of symmetry for increased performance. Ariadne is a parallel, two- and three-dimensional, electrostatic, self-consistent and trajectory code for the simulation of electron beam optics in gyrotrons [54, 55]. Ariadne uses the finite element method to solve the Laplace and Poisson equations on a curvilinear cubic mesh for three-dimensional simulations and on a curvilinear quadrilateral mesh for two-dimensional simulations. The required mesh is automatically generated by a parametric mesh generator based on the mapping technique.

A direct comparison of the magnetic field calculated with Maxwell's equations in COMSOL Multiphysics® (COMSOL) software and that of Ariadne show an excellent agreement in simulation. First, the SMF of the neighboring gyrotrons is calculated using the exact calculation in Ariadne. Second, the

magnetic field of the tokamak has been approximated by a magnetic dipole, due to the relatively large distance to the gyrotron under investigation and the time variant behavior of the plasma current.

The computational effort to calculate the SMF of neighboring gyrotrons with Ariadne is large considering the large number of gyrotrons, a growing number of ECRH installations, and operation possibilities. A reduction of the computational effort is important to be able to calculate new magnetic field constellations efficiently. One suitable method could be the already mentioned representation of a magnetic field source by a magnetic dipole, as used for the tokamak. In that case, the magnetic field $\vec{B}$ of a dipole is defined by [56]

$$\vec{B}\left(\vec{d}\right) = \frac{\mu_0}{4\pi} \frac{3\,\vec{d}\left(\vec{m}\cdot\vec{d}\right) - \vec{m}\,|\vec{d}|^2}{|\vec{d}|^5} \tag{1.13}$$

with the vacuum permeability μ_0, the distance vector $\vec{d}$ and the magnetic moment vector $\vec{m}$.

Major SMF sources, such as tokamak central and poloidal field coils and gyrotron magnets are aligned with the z-axis in a 2-D cylindrical coordinate system. The magnetic moment is then simplified to a single component in the z-direction m_z. As a result, the radial and axial magnetic field components B_r and B_z of a magnetic dipole in the center of the coordinate system are derived from equation 1.13 as follows

$$B_\mathrm{r} = \frac{\mu_0 m_\mathrm{z}}{4\pi} \frac{3rz}{\left(r^2+z^2\right)^{5/2}} \tag{1.14}$$

$$B_\mathrm{z} = \frac{\mu_0 m_\mathrm{z}}{4\pi} \frac{2z^2-r^2}{\left(r^2+z^2\right)^{5/2}} \tag{1.15}$$

at the radial position r and the axial position z. Both equations 1.14 and 1.15 do not contain any integral like the Biot-Savart law or derivatives as the method of field extrapolation from the magnet axis. The direct analytical definition of the magnetic field at all places allow for a very efficient calculation of the magnetic field.

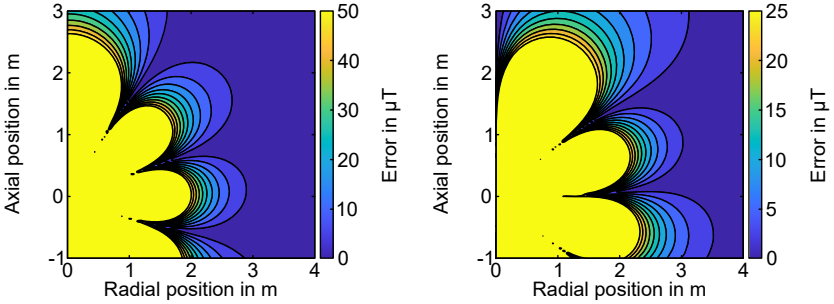

(a) axial B_z **(b)** radial B_r

Figure 1.8: Error in the magnetic dipole approximation for a 170 GHz gyrotron for (a) the axial magnetic field B_z and (b) the radial magnetic field B_r.

However, the simplified form of a cylindrical solenoid as a magnetic dipole limits the accuracy. The error of the magnetic field dipole approximation of a 170 GHz gyrotron magnet is shown in Fig. 1.8 for the axial and radial magnetic field components. The error of each component is calculated with the absolute value of the difference between the exact calculation of the magnetic field and the approximation. The maximum magnetic field in the figures is set to roughly the earth's magnetic field in Central Europe which is about 44 µT (B_z) in the vertical and about 20 µT (B_r) in the horizontal component [57]. The error of the magnetic dipole approximation is less than half the earth's magnetic field for distances larger than 2.5 m. That distance is approximately 10 times the radial dimension of the main coil of the gyrotron magnet.

For the DEMO tokamak SMF approximation, the minimum distance required to achieve the same error limit is approximately 110 m. In the current DEMO ECRH building design [58], the distances from the gyrotron to the tokamak (160 m) and between gyrotrons (7 m) exceed this limit, allowing the magnetic field calculation to be simplified using the magnetic dipole approximation.

The computational effort to simulate the influence of ferromagnetic SMF sources to the operation of the gyrotron is significantly higher compared to the SMF of the tokamak or neighboring gyrotrons. In most cases, where the distances to active SMF sources are large enough. Hence, it is sufficient to use the dipole approximation to represent the tokamak and neighboring gyrotrons in ECRH assemblies for a simple analytical definition of the SMF. However, the magnetic field of a passive SMF source like ferromagnetic structures must

be calculated by using 3-D software such as COMSOL. The challenge in those calculations is to include the ferromagnetic structure and also the magnetic field sources in its proximity. The structure size and with that the number of mesh cells significantly increases, if compared to a 3-D simulation setup of a gyrotron magnet.

Measurement of Stray Magnetic Fields

The alternative option to get information of the SMF at the position of the gyrotron is a measurement. This approach is especially useful for ferromagnetic structures nearby the gyrotron and to identify existing objects that are not taken into account yet. It is useful, when gyrotrons are added to existing operation sites that are grown over time and not specifically designed for gyrotron operation, or in ECRH installations with many gyrotrons at different states of operation. The challenging part in the SMF measurement is that the superconducting magnet of the device under test must be excited with current to attain a magnetization of the disturbing ferromagnetic material to produce the SMF. However, given the typical field strength in the range of 100 mT in the collector region of the gyrotron magnet, the measurement of small disturbances in the range of several tens to hundreds of µT requires special care in the selection of the measurement sensor.

In frame of this thesis a Printed Circuit Board (PCB) is designed and built with eight 3-D Hall effect sensors [59], a socket for a microcontroller board and a multiplexer to increase the number of possible Hall sensors. The PCB is shown in Fig. 1.9a. The master PCB can be expanded with multiple identical slave PCBs for an increased number of sensors on the measurement axis. The PCBs are mounted on a moving table to change the x and y coordinate in the horizontal plane as shown in Fig. 1.9b. The position of the PCBs in axial direction is not modified due to the multitude of Hall sensors that measure the magnetic field at different axial positions simultaneously. The measurement data is collected by the microcontroller, averaged over a small time frame of a few milliseconds and send to a computer running MATrix LABoratory (MATLAB) software. Multiple measurements are taken at each coordinate and combined in post-processing on the computer. The presented measurement system could be used as a basis for a future intelligent SMF compensation system for gyrotron collectors in closely packed ECRH installations.

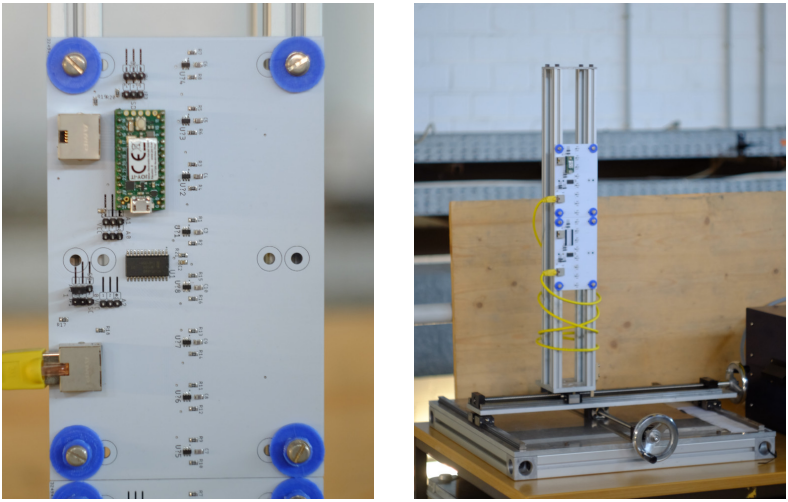

(a) PCB **(b)** Measurement system

Figure 1.9: (a) PCB of the measurement system with eight 3-D Hall effect sensors and (b) measurement assembly for controlled movement in the horizontal plane and two PCBs.

Sensitivity of Collectors in Environments of Stray Magnetic Fields

The SMF sensitivity is directly related to the nominal magnetic field, which is weak in the collector region. The shape of the electron beam is more influenced when the relative SMF is high and when the disturbance is accumulated over a long path. However, the strength of the magnetic field is also connected to the electron beam radius as shown by modification of the Bush theorem according to equation 1.10 and conversion to

$$B_{\mathrm{z,col}}\, {r_{\mathrm{gc,col}}}^2 = B_{\mathrm{z,cvt}}\, {r_{\mathrm{gc,cvt}}}^2 \tag{1.16}$$

Here $r_{\mathrm{gc,cvt}}$ and $r_{\mathrm{gc,col}}$ are the guiding center radii of the electron beam in the cavity and the collector, respectively, instead of the beam thicknesses $\Delta r_{\mathrm{b,cvt}}$ and $\Delta r_{\mathrm{b,col}}$ at both positions. In order to collect the electron beam at the collector wall instead of the top plate, it is required that the collector radius is equal to $r_{\mathrm{gc,col}}$ at the position where the beam should be collected (not considering the beam thickness). The right side of equation 1.16 is constant

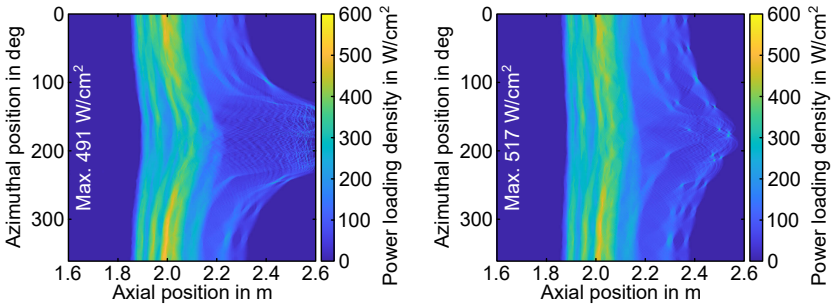

(a) 4 m **(b)** 5 m

Figure 1.10: Collector wall loading under the influence of a neighboring gyrotron in (a) 4 m and (b) 5 m distance.

if the gyrotron is kept identical and only the collector is modified. It can be seen that an increase of the collector radius by $\sqrt{2}$ will reduce $B_{\mathrm{z,col}}$ to half and in consequence increasing the relative SMF of the surrounding sources by a factor of two. The opposite applies for a decrease of the collector size by the same factor. However, a large collector is required for high-power applications due to the limited power loading density at the collector wall introduced with the cooling and sweeping method.

The most predictable source of SMF in an ECRH assembly are neighboring gyrotrons due to the static operation of their magnets, compared to the variable characteristics of the fusion plasma inside the tokamak. As an example for the sensitivity of SDCs in SMF, the ITER 170 GHz 1 MW CW gyrotron with it's 225 mm inner collector radius is used as a reference scenario. The reference without SMF is already shown in Fig. 1.7c. In this example, the effect on the collector wall loading is analyzed with a second gyrotron placed in 4 m distance and 5 m distance, respectively. The result is shown in Fig. 1.10a and Fig. 1.10b. It can be seen that the operation of two gyrotrons in 5 m distance from each other without other sources of SMF is still acceptable, as no electrons are collected at the top plate at the axial position of 2.6 m. For a distance of only 4 m, some electrons are collected at the top plate and could cause damage to the welded connection between the cylindrical collector wall and the top plate. The effect is caused by the radial magnetic field component of the neighboring gyrotron magnet, which is mostly present in the region of the collector and electron gun. In the cavity, only an axial component of SMF is present, due to the identical axial position of both magnets. But, it is possible to compensate

the radial SMF in the collector region either by a constant current in the coils of the TMFS or by dedicated compensation coils [60].

However, a detailed description of such a system is beyond the scope of this work. The SMF of the tokamak can be approximated as constant in the area of a single gyrotron, due to the relatively large distance between the two. The limit for radial SMF is considered to approximately 200 µT before electrons hit the top plate of the collector in the same configuration as before [52]. At this level, the collector wall load is comparable to the case with a neighboring gyrotron in 5 m distance.

1.5 Multistage Depressed Collectors

Multistage Depressed Collectors are widely used in different kind of vacuum electron tubes like TWTs or klystrons to increase the overall tube efficiency and decrease the thermal load in the collector [61–63]. Both of these aspects are important in applications where high output power is required, or where it is difficult to dissipate heat, and the tube is operating on a limited power supply, such as in space satellites.

In the past, it was believed that MDCs for gyrotrons would not work with the challenges discussed in the next subsections, and consequently research on this topic was reduced to a minimum. In recent years, a rise in new fusion machines with increasing ECRH power has supported research into a new class of efficient gyrotrons equipped with MDCs. The fundamental principle of MDCs is presented in section 1.5.1 on the example of a gyrotron spent electron beam. The method of electron beam separation as used in other vacuum electron tubes is shortly discussed in section 1.5.2 whereas a promising concept for electron separation based on $\vec{E} \times \vec{B}$ drift is discussed in section 1.5.3.

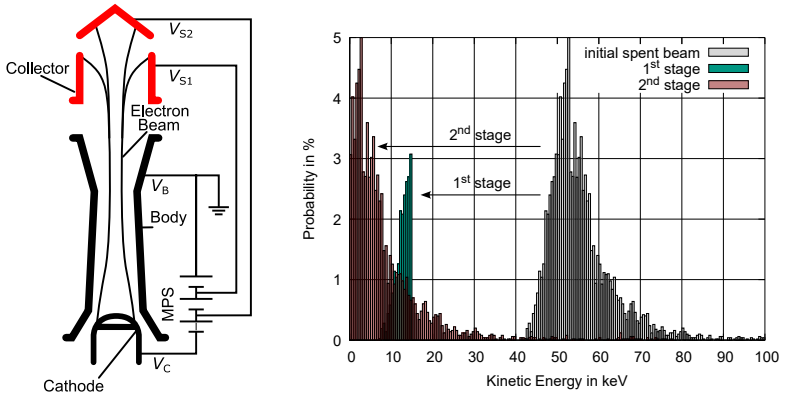

(a) Potentials **(b)** Energy distribution

Figure 1.11: Schematic view of an MDC with the electric potential connection to the PSU (a) and energy distribution of the spent electron beam before and after deceleration in the MDC (b).

1.5.1 Fundamental Principle of the Energy Recuperation in MDCs

Theoretically, the spent beam electrons in an MDC are sorted according to their initial kinetic energy increasing the collector efficiency. The schematic view of a gyrotron with an MDC is shown in Fig. 1.11a. A 2-stage collector is selected as a representation of the method. The use of an additional PSU or an additional module in a Modular Power Supply (MPS) is assumed for every stage, increasing the complexity of the system. The beam energy distribution of the KIT 2 MW 170 GHz coaxial-cavity gyrotron [33] before and after deceleration in a 2-stage collector is shown in Fig. 1.11b. The slow electrons are decelerated by 35 kV whereas the faster electrons are decelerated by additional 15 kV in this example. In consequence of the additional deceleration in the MDC, the remaining energy of the electron beam is reduced thus increasing the collector efficiency.

The maximum theoretical collector efficiency with two stages is at 86.6 % with depression potentials of 42.35 kV and 51.6 kV for the first and second stage, respectively. No reflected current is allowed in the simple investigation, space charge effects are ignored and all spent beam electrons have to be distributed optimal onto both stages. In comparison, the theoretical maximum collector

efficiency of an SDC with the same energy distribution is at 75.4 % and the same depression potential as the first stage of the MDC. However, due to space charges it is not possible to achieve such high depression potentials on the first collector stage. The limit for the depression potential of this gyrotron with an SDC is at 35 kV [64, 65], while the calculated theoretical collector efficiency is reduced to 62.3 %. In an MDC, only the potential of the first electrode is limited by the space charge effect and a higher depression potential can be applied to the second stage. A maximum theoretical efficiency of 83.5 % could be achieved with the limited potential on the first stage of 35 kV and a potential of 49.7 kV at the second stage. The remaining kinetic energy of the decelerated spent electron beam would be reduced to less than half.

1.5.2 Non-Adiabatic Separation of Electrons

The presence of a high magnetic field at the collector region of a gyrotron confines the electrons of the spent beam. Therefore, the electrostatic approach used in TWTs and kystrons for the separation of the electron trajectories according to their initial energy is not applicable in gyrotrons. In non–adiabatic electron separation, the beam electrons are separated by a dominant electric field in the collector region for the axisymmetric concept as proposed in 1998 [66]. The magnetic field must be smaller than 1 mT in order to achieve a strong demagnetization at the collector entrance using extra coils or ferromagnetic material. A design of such a collector system was shown for a 1 MW 110 GHz gyrotron [67, 68]. An increase in the gyrotron frequency would result in an increase in the SMF of the superconducting gyrotron magnet in the collector region. The length and radius of such a type of collector have to be increased to maintain the small magnetic field in the collector region. The major disadvantage of this approach is the influence of secondary electrons. It has been shown [69] that the secondary electrons emitted from one stage are traveling to the neighboring electrodes. This significantly decreases the efficiency of such a system. Despite the limitations of the design, a prototype was manufactured with all subassemblies. Unfortunately, due to a lack of experimental equipment, the collector was never tested.

1.5.3 Fundamental Concept of an MDC using *E×B* Drift

The $\vec{E}\times\vec{B}$ concept, proposed in 2008 [70], is based on the $\vec{E}\times\vec{B}$ drift for the separation of the electron trajectories according to their kinetic energy. In this frame, several design approaches have been studied for the annular gyrotron beam such as:

- Transformation to sheet beam [71, 72].
- Azimuthal magnetic field [73, 74].
- Azimuthal electric field. The concept with an azimuthal electric field is divided into the coaxial approach with an outer and inner structure, where half of the electron beam is collected by the inner part and the other half by the outer part [70, 75] and the cylindrical approach, where the majority of the spent electron beam is collected at the outside [18, 76, 77].

The $\vec{E}\times\vec{B}$ drift concept is considered as the most promising method for separation of the spent beam electrons in a high-power gyrotron MDC [69, 78, 79]

The electrons inside a gyrotron are confined by the strong magnetic field of the gyrotron magnet. Hence, their trajectories follow the magnetic field lines in axial direction. An additional electric field component $\vec{E}_{\parallel}$ parallel to the magnetic field would slow down the spent electron beam. This field component is also generated at the entrance of the SDC by the depression potential applied to the collector wall. The spent beam electrons would be decelerated until their kinetic energy is zero, if $\vec{E}_{\parallel}$ is present in the entire collector region, and then reflected backward. The position of the reflection depends on the initial kinetic energy of the electron. If an additional component of an electric field $\vec{E}_{\perp}$, perpendicular to the magnetic field, is applied, then it is possible to separate the trajectories of the spent beam electrons as shown schematically in Fig. 1.12. The transverse electric field $\vec{E}_{\perp}$ causes a drift velocity $\vec{v_{\mathrm{d}}}$ in the orthogonal direction to the movement of the electrons. The drift velocity is given by the equation [70]

$$\vec{v_{\mathrm{d}}} = \frac{\vec{E}\times\vec{B}}{B^2} \tag{1.17}$$

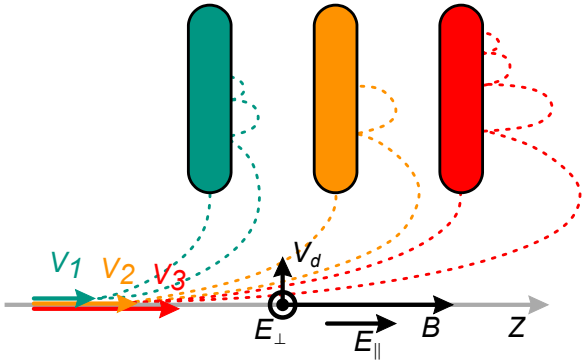

Figure 1.12: Beam electron separation based on their initial kinetic energy.

where $\vec{E}$ and $\vec{B}$ are the electric and magnetic field vectors in the collector region, respectively. As an example Fig. 1.12 includes three different electrodes. The electrodes are placed at positions where the kinetic energies of the electrons are at their minimum. Electrons with kinetic energies between two electrodes will be collected by the electrode with the lower potential.

The main advantage of this idea is that the secondary electrons generated by the spent beam electrons are exposed to the $\vec{E}\times\vec{B}$ drift in the same direction as the primary beam electrons and are pushed deeper into the region between the electrodes. Therefore, it is unlikely that those electrons move either backward to electrodes with lower voltage, reducing the collector efficiency, or toward the cavity, affecting the electronic efficiency. Only electrons that hit the side of an electrode are likely to generate secondary electrons that can go to stages with a lower depression potential, thus reducing the collector efficiency.

1.6 Outline

In this chapter an overview of gyrotrons with the key aspects for efficiency relevant parameters is presented. The motivation to design and build the first MDC for a high-power fusion relevant gyrotron is highlighted and the basic principle of MDC operation is introduced. In the following chapters, the fundamental design decisions for the MDC prototype are discussed and the most promising design is presented in detail. It starts with chapter 2 where the fundamental considerations in the development of the MDC are presented. This includes the requirements on the high voltage PSU in section 2.1, and the application to gyrotron designs at KIT in section 2.2. Different $\vec{E}\times\vec{B}$ MDC designs are presented in section 2.3 and concrete design concepts which are relevant for the development of the MDC prototype are presented in section 2.4.

In chapter 3, a systematic step-by-step approach of the development of the MDC prototype is illustrated. The fundamental electromagnetic configuration is shown in section 3.1. The final design for manufacturing and assembly is described in section 3.2 with the modular mechanical design, the fabrication of individual parts and assembly of the prototype. At the end of that chapter, a short summary is given in section 3.3 to evaluate the development of the prototype.

The following chapters 4 and 5 provide an outline future collector concepts based on the $\vec{E}\times\vec{B}$ drift. The first is a CW compatible MDC design approach which is based on the SP MDC prototype. The second is a new concept of electron beam sweeping for SDCs with electric instead of magnetic field to eliminate the cyclic fatigue of the collector. Finally, the conclusion of the entire study is presented in chapter 6.

2 Fundamental Considerations in the Development of Multistage Depressed Collectors

The development of an initial MDC prototype for a high-power gyrotron must be adapted to existing equipment, to limit the engineering and financial effort. Related key aspects of the MDC development are discussed in the following sections starting with the requirements on the high voltage PSU in section 2.1, the possible $\vec{E}\times\vec{B}$ collector geometries in section 2.3, the application at KIT in section 2.2 and concrete design concepts in section 2.4.

2.1 Requirements on the High Voltage Power Supply

A gyrotron can be represented as a constant current to time varying current converter and therefore requires a constant voltage and current source to generate the electron beam. However, there are two important points to note:

- The power grids typically operate with time varying current.
- The constant voltage for the gyrotron must be properly controlled to ensure safe startup and reliable operation.

Therefore, a Power Supply Unit (PSU) is needed that converts time varying current to a precisely controlled constant current. In addition, the PSU should operate as efficiently as possible, using the recovered power from a depressed collector to save power instead of wasting it.

It is important to understand the applied voltages and currents in different gyrotron configurations to understand the power saving in a PSU with recovered

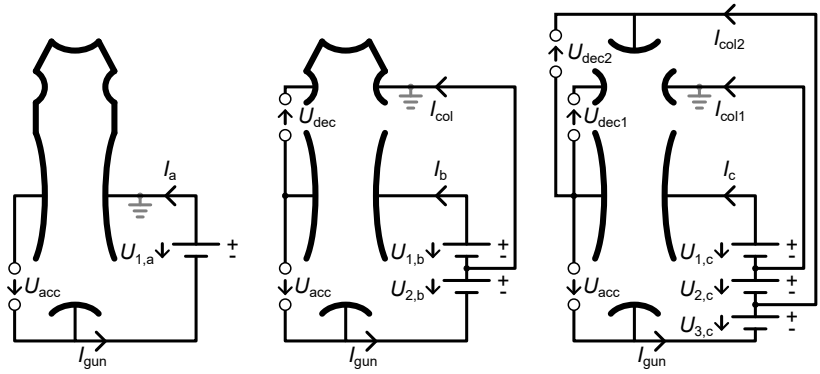

(a) Non-depressed **(b)** SDC **(c)** 2-stage MDC

Figure 2.1: Schematic views of different PSU configurations. Operation with a non-depressed collector and single PSU (a), operation with an SDC and two PSUs and operation with an MDC with 2-stages and three PSUs.

power. The classical scheme of the PSU potential setup of a gyrotron with SDC operation, where the collector potential is set to GND, is briefly mentioned in section 1.4.1. For an MDC only one collector electrode or the body of the gyrotron can be connected to GND potential. However, the potential reference point of the PSU is less important than the voltages and currents as shown in Fig. 2.1.

In all examples, the most negative potential is connected to the cathode or electron gun, where the electrons are emitted, accelerated and formed to an electron beam. All electrons are accelerated by an acceleration voltage U_{acc} between the cathode and the gyrotron body, hence the energy of all accelerated electrons is very similar. In all examples, the body potential is the most positive potential. The current of the complete electron beam is defined to I_{gun}, defining the power of the accelerated electron beam (without space charge effect) to

$$P_{\mathrm{acc}} = U_{\mathrm{acc}}\, I_{\mathrm{gun}} \tag{2.1}$$

After interaction with the microwave, electrons are collected at the anode. The remaining power of the spent electron beam is converted into heat at the collector surface.

The non-depressed collector represents the simplest case for gyrotron operation and is shown in Fig. 2.1a. This configuration involves the utilization of a single PSU and allows for the description of the gyrotron with a single circuit. The gyrotron body and anode are electrically connected to the same potential. Hence, the voltage of the single PSU $U_{1,\mathrm{a}}$ is identical to the acceleration voltage U_{acc} and the current of the anode I_{a} is identical to the beam current I_{gun}. The PSU delivers the full power to the accelerated electron beam P_{acc}.

In an SDC configuration, the gyrotron body and anode are electrically isolated to apply a deceleration voltage U_{dec} before the electrons hit the single collector stage as shown in Fig. 2.1b. Ideally, all electrons are collected at the anode to obtain the two approximations for the body current $I_{\mathrm{b}} \approx 0\,\mathrm{A}$ and the collector current $I_{\mathrm{col}} \approx I_{\mathrm{gun}}$. The PSU for the SDC configuration is divided into two modules that together provide the acceleration voltage for the electron gun $U_{\mathrm{acc}} = U_{1,\mathrm{b}} + U_{2,\mathrm{b}}$. The deceleration voltage at the collector entrance $U_{\mathrm{dec}} = U_{1,\mathrm{b}}$ is limited by the slowest electron as discussed in section 1.4.1. The power P_{SDC} of the PSU of a gyrotron with an SDC is reduced to

$$P_{\mathrm{SDC}} = U_{1,\mathrm{b}}\, I_{\mathrm{b}} + U_{2,\mathrm{b}}\, (I_{\mathrm{b}} + I_{\mathrm{col}}) \approx U_{2,\mathrm{b}}\, I_{\mathrm{gun}} < P_{\mathrm{acc}} \tag{2.2}$$

and is always smaller than P_{acc} under the condition that $U_{1,\mathrm{b}} > 0\,\mathrm{V}$.

An additional deceleration voltage U_{dec2} and an additional PSU are introduced in the example of the 2-stage MDC as shown in Fig. 2.1c. The collector is split into two individual anodes with different potentials to achieve two different deceleration voltages. Only the smaller deceleration voltage U_{dec1} is limited by the slowest electron and the second deceleration voltage U_{dec2} can be increased. The body current in the MDC configuration is identical to the SDC configuration and approximated to $I_{\mathrm{c}} \approx 0\,\mathrm{A}$, whereas the beam current is split due to the two anodes $I_{\mathrm{gun}} = I_{\mathrm{col1}} + I_{\mathrm{col2}}$. For simplicity, it is assumed that U_{dec1}, U_{dec}, $U_{1,\mathrm{c}}$ and $U_{1,\mathrm{b}}$ are identical and $U_{\mathrm{dec1}} < U_{\mathrm{dec2}} = U_{1,\mathrm{c}} + U_{2,\mathrm{c}}$ for a simple power analysis. However, in section 2.3.3 it is shown that the deceleration voltages have a higher degree of freedom in the design of MDCs compared to SDCs. The acceleration voltage is again the sum of all PSU modules $U_{\mathrm{acc}} = U_{1,\mathrm{c}} + U_{2,\mathrm{c}} + U_{3,\mathrm{c}}$. The required power that the PSU has to deliver to the gyrotron is reduced to

$$\begin{aligned} P_{\mathrm{MDC}} &= U_{1,\mathrm{c}}\, I_{\mathrm{c}} + U_{2,\mathrm{c}}\,(I_{\mathrm{c}} + I_{\mathrm{col1}}) + U_{3,\mathrm{c}}\,(I_{\mathrm{c}} + I_{\mathrm{col1}} + I_{\mathrm{col2}}) \\ &\approx U_{2,\mathrm{c}}\,(I_{\mathrm{gun}} - I_{\mathrm{col2}}) + U_{3,\mathrm{c}}\, I_{\mathrm{gun}} \\ &= (U_{2,\mathrm{c}} + U_{3,\mathrm{c}})\, I_{\mathrm{gun}} - U_{2,\mathrm{c}}\, I_{\mathrm{col2}} < P_{\mathrm{SDC}} \end{aligned} \tag{2.3}$$

and is always smaller than P_{SDC} under the conditions that $U_{2,\mathrm{c}} > 0\,\mathrm{V}$, $I_{\mathrm{col2}} > 0\,\mathrm{A}$ and $U_{2,\mathrm{b}} = U_{2,\mathrm{c}} + U_{3,\mathrm{c}}$.

It can be concluded that a gyrotron equipped with an SDC will always consume less power than a gyrotron without a depressed collector, and that a gyrotron equipped with an MDC will always consume less power than a gyrotron equipped with an SDC, if the first deceleration voltage is identical. The complexity of PSU modules is dependent on voltage and current. It is more obvious when the first collector stage, the one with the lower deceleration voltage, is set to GND as reference potential. The PSU module(s) responsible for the potential of the gyrotron body are only required to deliver a voltage with no or only a very small current, whereas only the module(s) for the cathode and second collector stage potential deliver a voltage and significant current.

2.2 Application to Gyrotron Designs at KIT

For experimental verification of the MDC it is required to mount the collector on an existing gyrotron and place it in an available magnet in the appropriate teststand at KIT. In the next paragraphs, the available hardware at KIT that can be used for the first MDC experiments is listed and analyzed for its compatibility with the current collector design.

2.2.1 KIT Gyrotron Teststand

There are two gyrotron teststands with a total of three places for gyrotron operation at the Institute for Pulsed Power and Microwave Technology (IHM) KIT. The older teststand has two places with a 5.6 T and another 6.87 T SC magnet. Both places share one thyristor based PSU with up to 90 kV and 80 A [80]. The PSU is suited for gyrotron operation with output powers of 0.5 MW

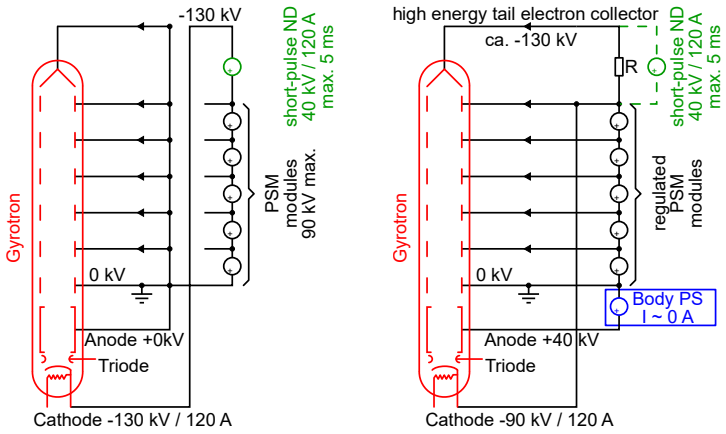

(a) Non-depressed **(b)** Depressed

Figure 2.2: Operation modes of the modular FULGOR PSU in SP operation with pulsed power supply (a) and LP operation without pulsed power supply but with body power supply (deviated from [81]).

in CW, 1 MW for up to 3 min and 2 MW for up to 10 s. The cathode power supply is combined with a low current body PSU to operate gyrotrons with an SDC. The gyrotron collector potential must be at GND potential since no other potential in the PSU is designed to accept current. Consequently, operation with an MDC on this PSU is not possible without using another PSU as a sink.

The third gyrotron teststand at IHM KIT is the new **Fu**sion **L**ong Pulse **G**yrotron Lab**or**atory (FULGOR) teststand with a modular 10 MW PSU [82–84]. The maximum current is at 120 A, while the maximum voltage at the cathode is at 90 kV in CW and up to 130 kV in SP operation. An additional body PSU is installed with a voltage of up to 40 kV for the operation of conventional SDCs. Two schematics of pulsed non-depressed and depressed CW operation modes are shown in Fig. 2.2a and Fig. 2.2b, respectively. The high-power components of the modular PSU, capable of 90 kV during CW operation, are built from 80 individual modules and are represented by a few modules in Fig. 2.2. Each module is equipped with an intermediate connection point to provide potential to individual MDC electrodes. This PSU is the only available option to use for the first MDC experiments at KIT.

2.2.2 Available Gyrotron Magnets at KIT

The FULGOR teststand is prepared for the use of cryogen free superconducting magnets in mind, and it is not compatible with magnets that need supply lines for liquid helium and nitrogen. Both the 5.6 T and 6.87 T magnets at IHM KIT are not compatible with FULGOR due to the need for liquid helium and nitrogen. A high-voltage connection from the FULGOR PSU to one of these magnets is considered, however, the idea is rejected due to significant cost and limitations in available human resources. The remaining option is to place a cryogen free superconducting magnet in the FULGOR teststand. A new 10.5 T SC magnet will complete the teststand by 2025.

The maximum magnetic field strength is one of the differences between the magnets listed. Other variations include the geometry and number of solenoids inside the magnet housing, additional coils to adjust the magnetic field profile, and different dimensions of the magnet housing itself. From a mechanical point of view, the most important parameters for operating a gyrotron in a specific magnet are the diameter of the bore and the axial position of the gyrotron cavity at the maximum magnetic field. Once the mechanical conditions are fulfilled, the magnetic field profile at the MIG has to be adjusted to obtain the correct beam radius in the cavity and the correct electron pitch factor. As a result, it is not possible to operate every gyrotron in every magnet. The replacement of single components, such as the anode of the MIG, is used to adapt an individual gyrotron to a different magnet. Nevertheless, such adaptations are not universally applicable.

2.2.3 Available Gyrotrons at KIT

The gyrotrons available at KIT for MDC experiments are SP pre-prototype devices that can be opened and where individual parts can be easily replaced modularly. Those gyrotrons are the 140 GHz 1.5 MW W7-X Upgrade SP gyrotron, the 170 GHz 1 MW ITER SP gyrotron and the KIT 2 MW 170 GHz coaxial-cavity gyrotron. Since MDC technology is most relevant for future fusion machines like DEMO, it is decided to optimize the MDC for operation for the 2 MW coaxial-cavity gyrotron as shown in Fig. 2.3a. This gyrotron is compatible to the new 10.5 T SC magnet by applying a slightly modified anode for the MIG and a modified coaxial insert.

(a) SP pre-prototye

(b) LP prototype

Figure 2.3: Comparison between (a) SP and (b) LP 2 MW coaxial-cavity gyrotron [65].

In SP gyrotrons, only a simple cooling is implemented for some parts of the tube, which is in contrast to LP and CW gyrotrons. Even in SP gyrotrons, the MIG is always oil cooled due to the heated emitter to achieve controlled electron emission. Individual components of the gyrotron, particularly the collector, are significantly increased in size with the pulse length due to the high-power load. The increased size and complexity of a LP gyrotron is shown in Fig. 2.3b with the larger collector and cooling pipes at the mirror box for the LP prototype of the 2 MW coaxial-cavity gyrotron taken as an example.

2.3 Concepts of MDCs Based on *E×B* Drift

All design concepts presented in this section did exist at the beginning of the research presented here and are used as a basis for the following designs. All designs presented after this section are developed and optimized in frame of this work. The created concepts, which have already been published, have been referenced accordingly at the beginning of each section.

In this work, the concept of electron beam separation based on the $\vec{E}\times\vec{B}$ drift is deployed for all MDC designs to achieve a spacial separation of their trajectories based on the kinetic energy. Two different approaches exist that use the $\vec{E}\times\vec{B}$ drift as mentioned in section 1.5.3. In this work, both approaches are presented in the form of three distinct realizations, as outlined in table 2.1 with the axial electric, coaxial and cylindrical design. The approach with an axial electric field E_z can be implemented with an azimuthal magnetic field B_θ in both rotation directions.

The approach with an azimuthal electric field E_θ is separated in the coaxial design where the azimuthal electric field must be implemented with both rotation directions and the cylindrical design where the majority of the azimuthal electric field must be implemented with one rotation direction. The limitation in the basic designs with azimuthal electric field is due to Faraday's law [56] which is defined as

$$\oint_{\partial\Sigma} E\,\mathrm{d}l = -\int_{\Sigma}\frac{\partial B}{\partial t}\,\mathrm{d}A \tag{2.4}$$

Table 2.1: Concepts of MDCs based on $\vec{E}\times\vec{B}$ drift.

Section	Name	Axial Field	Azimuthal Field	Azimuthal Direction
2.3.1	axial electric	E_z and B_z	B_θ	↺ **or** ↻
2.3.2	coaxial	B_z	E_θ	↺ **and** ↻
2.3.3	cylindrical	B_z	E_θ	↺ **or** ↻

where E and B are the electric and magnetic fields, Σ is an arbitrary surface with the boundary curve $\partial\Sigma$ and A and l are the corresponding infinitesimal element vectors, respectively. The right side of equation 2.4 is zero as a result of the magnetostatic field. The sign of the azimuthal electric field in a cross-section of the collector must flip to satisfy the physical limitation of Faraday's law. A reversal of the azimuthal electric field will automatically lead to the presence of electrons that drift in and out in radial direction. In consequence, half of the electrons are deliberately intended to drift inward for the coaxial design, while the amount of electrons that drift inward is kept to a minimum for the cylindrical design. As the names of the two principles suggest, the coaxial design requires an internal structure to collect part of the spent electron beam where this is not necessary in the cylindrical design.

2.3.1 Application of an Axial Electric Field

A collector with an axial electric field and an azimuthal magnetic field is developed, built and verified in parallel to the work presented here by Peter the Great St. Petersburg Polytechnic University for a 74.2 GHz, 100 kW gyrotron [73, 74, 85–89]. A schematic representation of the MDC developed is shown in Fig. 2.4. The collector design uses the axisymmetric electrodes marked with "S1" to "S4", which only have to produce an axial electric field as the electrodes in MDCs of TWTs and klystrons. The axial symmetry provides a proper scalability of the number of collector stages as presented in the schematic with a four stage design. However, the simple electrode layout for the axial electric field must be complemented with a complex magnetic coil layout to generate an azimuthal magnetic field B_θ.

Two different set of coils are used in the MDC: (i) traditional cylindrical coils marked with "C1" to "C7" to shape the electron beam radius, and (ii) the toroidal solenoid marked with "2" to produce the azimuthal magnetic field B_θ. According to Ampère's law, a current must be enclosed by the electron beam, which requires the toroidal solenoid to run through the center of the collector and radially outward with bundles marked with "3". A segmented electron gun must ensure that the electron beam does not intersect with the toroidal solenoid bundles at the collector entrance. In addition to the azimuthal magnetic field B_θ, an axial magnetic field B_z is present in the collector region due to the stray field of the gyrotron magnet. The addition of B_z results in a decreased angle

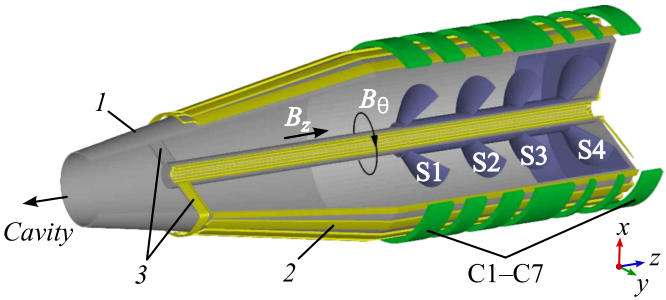

Figure 2.4: Schematic representation of an MDC with azimuthal magnetic field [88].

between the electric and magnetic field, decreasing the efficiency of the $\vec{E}\times\vec{B}$ drift. For a CW compatible MDC design for a fusion gyrotron, two critical aspects are introduced:

- The magnetic flux enclosed by the electron beam is increased in the collector region, due to an increased beam radius, which is required for higher gyrotron power levels and an increased magnetic field, which is required for increased operation frequency of the gyrotron. To keep a high $\vec{E}\times\vec{B}$ drift efficiency, the azimuthal magnetic field B_θ has to increase to keep the angle between the electric and magnetic field similar. The toroidal solenoid bundles must increase in size to create a high B_θ.
- Radial electric fields between the electrodes and the vacuum housing, in combination with the axial magnetic field B_z, create an azimuthal electron drift. This effect is also present in a configuration where the electrodes are on the exterior and the coil bundle is on the interior [86]. The azimuthal electron drift may be considered uncritical due to the axisymmetric design; however, it must be taken into account when considering reflected electrons as it might lead to electron collisions with the coil bundle at the collector entrance.

2.3.2 Approach Using a Discrete Electrode Design

This section is a summary of the results published in Ref. [75] which have been derived in frame of this doctoral research.

The idea of a coaxial MDC for gyrotrons is first presented in 2008 [70] with a design featuring an analytically defined potential distribution on the collector surface. A design with infinite number of electrodes is chosen for the demonstration of the $\vec{E}\times\vec{B}$ concept. In this section, the transition from an analytically defined potential distribution to a variety of coaxial MDC designs with discrete stages is presented. The variations include different numbers of stages, wall geometries, and design optimization progress. The electric field in the $\vec{E}\times\vec{B}$ drift region of the coaxial MDC design is applied by two sets of electrodes, the inner and outer structure. The outer structure is placed around the electron beam, stacked from bottom to top and collects the outwards drifting electrons. The inner structure is hanging from the top inside the hollow electron beam and collects the inwards drifting electrons.

The electric field of the original design, with infinite number of electrodes, is produced by a Dirichlet type boundary condition. It defines the electrical potentials of the inner and the outer cylindrical surface of the coaxial collector. The values of the potential on those two surfaces is defined as functions of the axial position z and the azimuthal angle θ, as shown in Fig. 2.5a. The steps, which are followed to define the MDC geometry with a small number of electrodes from the theoretical design with an infinite number of electrodes, are shown in Fig. 2.5b-d. First, four equipotential lines separate the boundary condition of the electric potential into five segments, as shown in Fig. 2.5b. Then, two segments in between are removed, and constant potentials are defined on the remaining three segments, as shown in Fig. 2.5c. Finally, the potentials are mapped to the inner and outer collector surfaces, as shown in Fig. 2.5d.

The replacement of the smoothly varied boundary condition with discrete electrodes has a significant influence on the electric field. The smooth variation of the electric field along the electron trajectories is replaced by a stronger electric field in the gap between neighboring electrodes. However, as discussed in Ref. [71], the electron drift due to $\vec{E}\times\vec{B}$ drift depends only on the potential and not how the electric field is varied. The electron drift distance is not changed with the transition between smooth potential distribution and discrete and finite number of electrodes.

A common characteristic of the coaxial design using an infinite number of stages and the coaxial design using a finite number of stages is that they aim for an equal split of the electron beam to the inner structure and outer structure. The division of the electron beam to the inside and outside is achieved in all

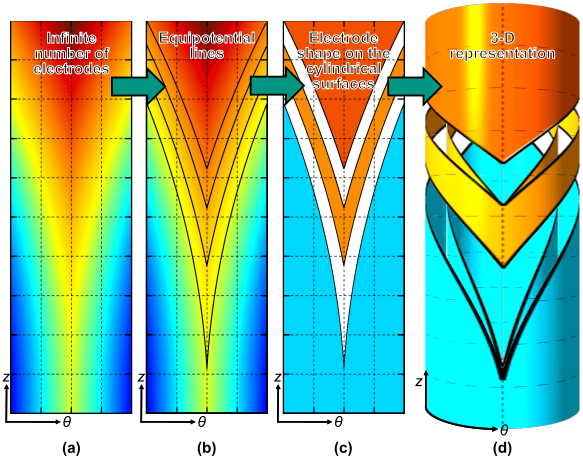

Figure 2.5: Electric potentials at the boundaries of the coaxial cylindrical MDC with (a) smoothly varied electric potential on an unrolled cylindrical surface, (b) four equipotential lines, (c) discrete electrodes with three different potentials, (d) and a three-dimensional representation [75].

designs presented here with a finite number of electrodes. Those electrodes are further simplified in their geometry to feature a constant slope which has a helical shape in 3-D and linear on the unrolled cylindrical surface. In the most simple case, the helical surfaces of the electrodes are defined in Cartesian coordinates with two surface variables $u = [0, \infty)$ and $v = [-1, 1]$ as follows:

$$\begin{aligned} x(u, v) &= u \, \sin(\pi \, v) \\ y(u, v) &= u \, \cos(\pi \, v) \\ z(v) &= |v| \end{aligned} \tag{2.5}$$

The commercial simulation tool CST Studio Suite (CST) is used to design and optimize the MDC. In the simulation, the geometry of the complex shape of the collector electrodes is defined by a combination of Boolean operations on cylindrical, conical, and hexahedral structures. A graphical representation of the two-stage depressed collector is shown in Fig. 2.6(a), whereas a vertical cross-section of the coaxial collector is shown in Fig. 2.6(b). As shown with

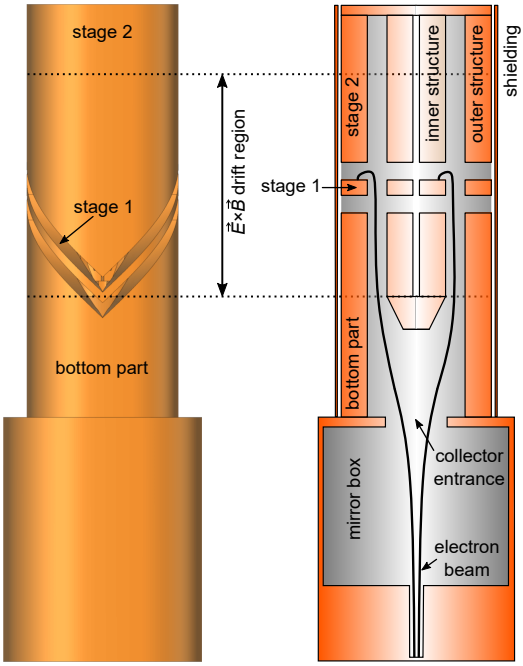

(a) CST **(b)** vertical cross-section

Figure 2.6: Basic shape of the coaxial two-stage depressed collector. (a) 3D model in CST and (b) vertical cross-section.

the horizontal cross-section in Fig. 2.7, indentations are applied on the inner and outer walls at the two azimuthal angles where the helices discontinue to minimize the probability of reflected electrons similar to Ref. [70]. In order to achieve a realistic simulation of the electron beam, the gyrotron mirror-box and the launcher are also modeled.

Initially, the material used in CST for the definition of the electrodes is a perfect electrical conductor. The spent electron beam is imported at the launcher entrance via the particle interface. A number of 100 000 electrons represent the spent electron beam. The initial kinetic energies and positions of these electrons are calculated with the proprietary tool Ariadne [55] based on the gyrotron cavity interaction. The static magnetic field in the simulation region

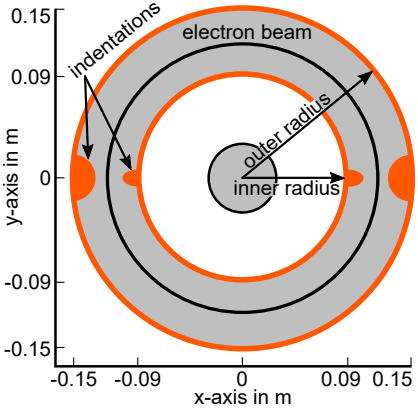

Figure 2.7: Horizontal cross-section of the coaxial two-stage depressed collector.

is also calculated by the Ariadne code and imported to CST [90]. The influence of the most important operating and geometrical parameters on the operation of the MDC system is investigated for the two-stage depressed collector. The electrode potentials are optimized for the spent electron beam to accomplish the desired behavior of the collector.

The collector efficiency increases with the number of depressed stages, which in turn increases the complexity of the mechanical construction. An additional layer of insulation (a helical gap) and high voltage and cooling feeds are necessary for every increment in the number of depressed stages. The geometries of MDCs with three- and four-stages are shown in Fig. 2.8, while the efficiencies achieved in simulation are listed in table 2.2. The efficiency of the MDC is increased with the number of stages as expected if comparing with values close to the theoretical maximum collector efficiencies. The calculation of the theoretical maximum collector efficiency is based on the spent electron beam energy distribution. On the other hand, the reflected current is not significantly influenced by the number of stages.

The size of the collector can be significantly decreased by a folded helical gap as proposed in Ref. [77]. The regions of inward and outward drifts are split into more regions with a smaller azimuthal section for each fragment. As an example, the design with a one-time folded spiral is shown in Fig. 2.9a, while the design with a two times folded spiral is shown in Fig. 2.9b. A collector

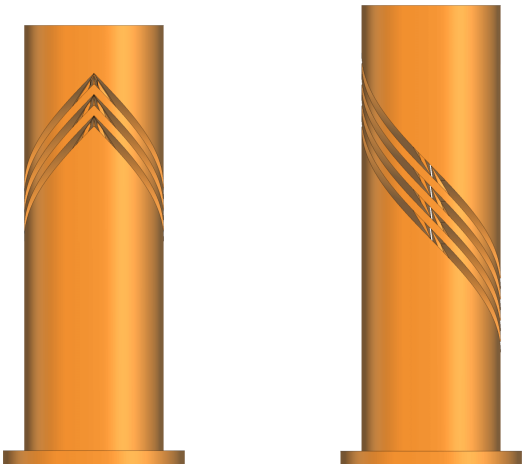

(a) Three-stage **(b)** Four-stage

Figure 2.8: Coaxial three- and four-stage depressed collectors.

with a single folded helix is defined to have twice the number of inward and outward drift regions as a collector with an unfolded helix. This number is again doubled for a collector with two-times folded helix. The initial axial position of the helical gap is given by the magnetic field constraints and the desired beam radius. The length of the $\vec{E} \times \vec{B}$ drift region is shown in table 2.3. The achieved performance of the designs with a folded helical structure is similar to the unfolded collector.

It should be mentioned that a variety of designs could be made by using the proposed approach. In particular, there is the possibility to place an insulator

Table 2.2: Results for different numbers of collector stages [75].

Collector stages	**2**	**3**	**4**
Theoretical maximum collector efficiency	83.5 %	87.3 %	90.7 %
Collector efficiency	81.9 %	83.2 %	87.4 %
Reflected current	45.5 mA	41.5 mA	38.8 mA

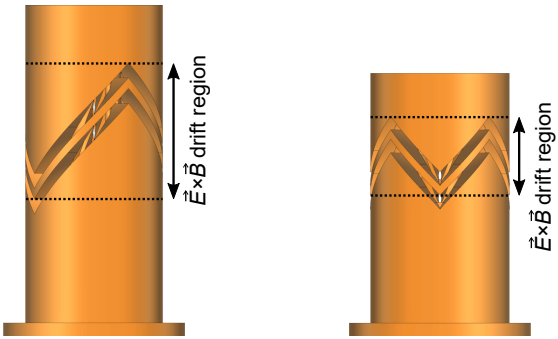

(a) One fold **(b)** Two fold

Figure 2.9: Two-stage depressed collectors with a folded helical structure.

between the gyrotron mirror-box and the collector to reduce the number of helical gaps by one. Another option is to replace the cylindrical shape of the electrodes by a conical shape. In this way, the additional collector coil system, necessary for the generation of the required magnetic field, is simplified.

2.3.3 Approach Using a Simplified Azimuthal Electric Field Concept

The second design concept of a gyrotron MDC using the azimuthal electric field approach is the cylindrical design without a coaxial insert. The removal of the coaxial insert is possible by changing the distribution of the electron beam drift directions to a design with an electron drift only towards the outer collector wall. The two design concepts based on the cylindrical concept are divided into the basic design and its improved version.

Table 2.3: Axial dimensions of different types [75].

Number of helix folds	**0**	**1**	**2**
Length of the *E*×*B* drift region	805 mm	464 mm	286 mm

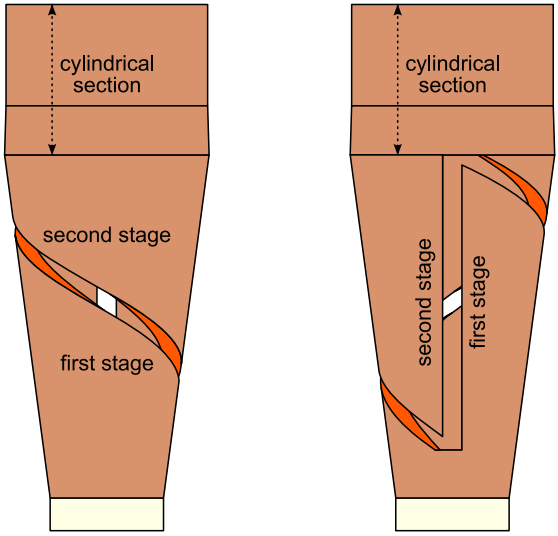

(a) Back view **(b)** Front view

Figure 2.10: Basic design of the cylindrical design approach with back and front view.

Basic cylindrical design

The layout of the cylindrical MDC design bases on a single helical separation of both electrodes. Both ends of the helix are connected with a straight cut [76]. In the simplest case, this helical surface is defined as the helical surface of the discrete electrode design shown by equation 2.5 in section 2.3.2. The only difference is the limitation of the surface parameter in the second direction to positive values $v = [0, 1]$. The first stage is positioned at the bottom of the collector and the second stage at the top with a cylindrical top section, as shown in Fig. 2.10.

The electrons at the azimuthal position of the helix will drift to the outside and are collected at the helical surface of the bottom electrode. A small amount of electrons, at the azimuthal position of the straight cut, will drift to the inside of the collector, where no electrode is placed. The guiding center radius of the faster electrons is only slightly influenced by the $\vec{E}\times\vec{B}$ drift before the collection on the second stage, due to the significantly higher axial velocity

compared to the drift velocity. The basic cylindrical design is shown in Fig. 2.10 with a back and front view. This design bases on two electrodes separated by the aforementioned helical and straight gap and insulated from the mirror-box by a ceramic ring at the bottom. The conical shape of the electrodes follows the magnetic field lines and significantly simplifies the requirements for the additional collector coils.

The collector is axially divided into three sections:

- **Lower section** at the entrance of the collector with adaption to the gyrotron. The spent electron beam radius is widened to the desired radius for electron separation in the $\vec{E}\times\vec{B}$ drift region. The electron beam is decelerated at the end of the initial section by the potential of the first electrode.
- **Center section** of the $\vec{E}\times\vec{B}$ **drift region** with electron separation. Region where both stages overlap in axial direction and an azimuthal electric field E_θ is created. Slow spent beam electrons are collected in the helical gap on top of the first stage while fast electrons are decelerated by the potential of the second stage.
- **Upper section** at the top of the collector. Fast spent beam electrons are collected at the cylindrical surface of the second stage.

Improved cylindrical design

The improved cylindrical design is based on the fundamental cylindrical MDC design presented earlier. It is improved to be smaller while the reflected current is decreased. The improved design is presented as the final design in Ref. [18] and as upgraded design in Ref. [77].

The three improved and upgraded key areas compared to the basic cylindrical design are:

- **Multiple helical repetitions** for reduced length as best shown in the back view of the MDC in Fig. 2.11a. The helical separation between both electrodes is modified from the single helix and straight cut of the basic design to multiple helices, in this example to a three-fold structure. The

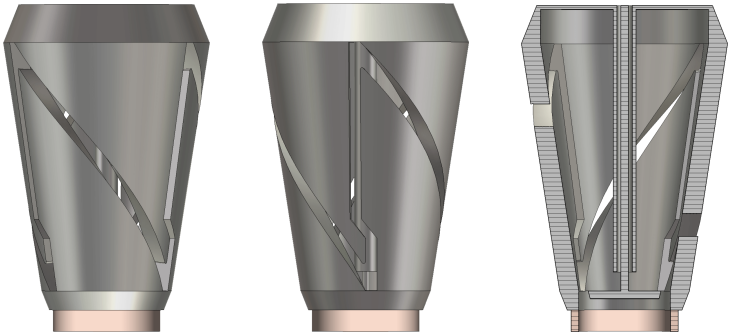

(a) Back view **(b)** Front view **(c)** Cut view

Figure 2.11: Improved version of the cylindrical design approach with back (a), front (b) and cut view(c).

slope of the helix is increased with the number of repetitions, allowing for a reduced length on the $\vec{E} \times \vec{B}$ drift region.

- **Increased angular range** of the helical gap as best shown in the front view of the MDC in Fig. 2.11b. In a design without helical overlap, the angular range of a single helix is approximately 360° divided by the number of multiple helices (minus the angle of the straight cut). The increased angular range is larger and the straight cut is split in a short part at the bottom and a larger part at the top. Slow electrons at the azimuthal positions of the short straight cut are only slightly influenced by it and collected by the first electrode at a higher axial position. The slow electrons at the azimuthal positions of the long straight cut are collected before they reach it. The result of this modification is a reduced reflected current.

- **Coaxial disk** to collect reflected electrons, as shown in the cut view of the MDC in Fig. 2.11c. Slow electrons, which are intended to be collected by the first electrode, experience an inward drift at the azimuthal positions of the straight cuts. Those electrons are subsequently collected by the coaxial disk instead of reflected back to the cavity, thus the reflected current is reduced.

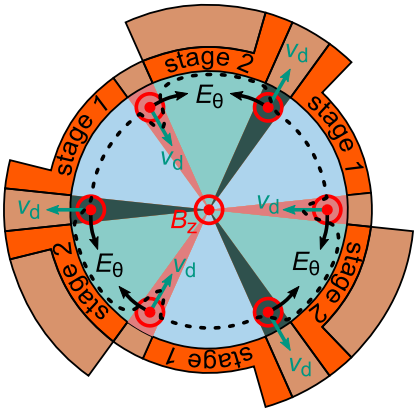

Figure 2.12: A representative cross-section showing the principle in the center of the $\vec{E}\times\vec{B}$ drift region of a simplified MDC design [91].

The drift directions and field components in the axial center of the $\vec{E}\times\vec{B}$ drift region of a simplified geometry, without helical extensions, are shown in Fig. 2.12 for a three-fold helical structure. Though the sectors with clockwise E_θ are unwanted, they are unavoidable due to Faraday's law. Fortunately, these sectors can be kept small in the design. The majority of the spent beam electrons is influenced by the counterclockwise E_θ in the larger part of the cross–section and is accelerated by a radial drift to the outside of the collector. The length of the $\vec{E}\times\vec{B}$ drift region is reduced by the number of helical repetitions, while the number of sectors with clockwise E_θ is increased. The increase of sectors with clockwise E_θ will increase the reflected current from the collector back to the cavity. The benefit in reduced collector size in axial direction for a collector system with a three-fold helical structure is promising while the reflected current is still within an acceptable limit, when the increased angular range of the helical gap, and optionally the coaxial disk, are implemented.

2.4 Design Concepts of Cylindrical MDCs

The first MDC prototype at KIT for verification of the $\vec{E}\times\vec{B}$ principle requires a decision on a design concept for optimization and manufacturing. The cylindrical design presented in section 2.3.3 is chosen due to its mechanical simplicity compared to the coaxial design with double the number of electrodes, and its simplicity of the magnetic field setup compared to the axial electric concept with the coils inside the vacuum housing. However, both cylindrical MDC designs presented, with the basic and improved design, are limited in some points that are addressed in this section.

The basic cylindrical design may seem simple at first glance however, there are significant drawbacks to this design. First, this collector is developed for a 170 GHz 1 MW hollow cavity gyrotron, which is operated in the 6.87 T gyrotron magnet at KIT. In this work, the goal is the development of an MDC for the KIT 2 MW 170 GHz coaxial-cavity gyrotron operated in the new 10 T magnet as described in section 2.2. The collector design is simplified with the lower output power and the faster diverging magnetic field of the 6.87 T magnet, due to the smaller magnet coils. Still, the physical dimensions of the collector are large with a length of 1.6 m, an inner radius at the bottom of the spiral of 135 mm and an inner radius at the top of 300 mm, not considering a vacuum housing which is required for operation. Second, even at this size, the collector is still a SP design as the power loading density is too high for CW operation. Third, the reflected current, the electrons which are not collected at the first electrode and have too little kinetic energy to be collected by the second electrode, is too high with around 700 mA for the 45 A electron beam of the 170 GHz 1 MW hollow cavity gyrotron [76].

The improved design offers a similar collector efficiency, while the reflected current is significantly reduced from 700 mA to around 40 mA and the size is considerably smaller [77]. However, the design still has drawbacks that had to be addressed. First, it is still optimized for the 170 GHz 1 MW hollow cavity gyrotron operated in the 6.87 T magnet at KIT. Second, the cylindrical top section of the second stage is too small to collect the remaining spent electron beam. Third, the coaxial disk is a difficult part to install and isolate. Fourth, the conical shape will be too large for a 2 MW gyrotron. An upscaled collector for a 2 MW gyrotron in the 6.87 T magnet with this design will be approximately 900 mm tall with an inner radius at the bottom of the spiral of

120 mm and 220 mm at the top, again without a vacuum housing. Lastly, the electron beam is positioned close to the inner collector wall making it sensitive to misalignment's and SMFs. A larger distance of the electron beam to the collector wall is required to increase the length of the collector.

Two new design concepts based on the cylindrical concept are developed in frame of this work. The efficiency optimized design is optimized to the most efficient depression potentials for the KIT 2 MW 170 GHz coaxial-cavity gyrotron based on the energy spectrum of the spent electron beam. The size optimized design is made as a compromise to still achieve a high collector efficiency with less optimal depression potentials, while the size is much better manageable for production of a first prototype. For both designs, an internal structure is not required due to the small fraction of spent beam electrons drifting inward. The majority of those electrons are also affected by an azimuthal electron drift, reflected by the magnetic field and collected at a different position at the collector. Only a fraction of the inward drifting electrons are finally observed as a reflected current.

2.4.1 Efficiency Optimized Design

The majority of the drawbacks for the previous designs are addressed by an efficiency optimized version of the cylindrical design approach with straight walls, which is shown in Fig. 2.13. This version is optimized for the KIT 2 MW 170 GHz coaxial-cavity gyrotron however, it is still developed with the 6.87 T magnet in mind. To achieve an optimized efficiency it is decided to apply the nominal SDC depression potential of 35 kV [65] to the first stage of the MDC. Higher depression potential at the first electrode would result in reflections of slow electrons, while the efficiency would be decreased for lower depression potentials. The theoretical optimum depression potential for the second stage is calculated based on the spent electron beam energy spectrum to 49.6 kV, giving a potential difference of 14.6 kV and up to 83.5 % collector efficiency [92]. The most complicated component of the improved design is the coaxial disk, as shown in Fig. 2.11c. It is mounted from the top and electrically insulated to the second electrode, while the potential of the first electrode is applied. The angular range of the helical gap is extended for the efficiency optimized design, to avoid the implementation of a coaxial disk. The reflected

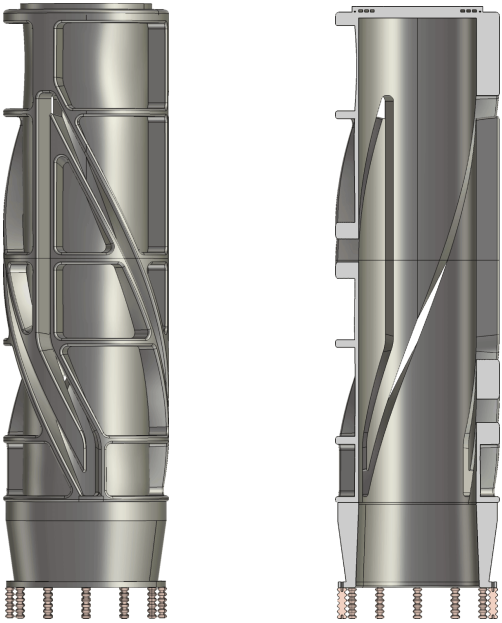

(a) Side view **(b)** Cut view

Figure 2.13: Efficiency optimized version of cylindrical design approach with straight walls.

current is kept at similar values, while the mechanical setup is significantly improved.

In consequence of the rather low potential difference between both collector electrodes, it is necessary to increase the length of the $\vec{E}\times\vec{B}$ drift region to achieve a strong $\vec{E}\times\vec{B}$ drift due to the steep helical incline with a high azimuthal electric field component. A length of 1 m is chosen for the $\vec{E}\times\vec{B}$ drift region resulting in a collector length of 1.6 m excluding the vacuum housing.

Collector walls with a conical shape are not reasonable at such a length due to the massive size in the radial dimension. For the basic design presented previously the inner collector radius is at 300 mm and would be similar for this collector design, which is too large for a SP collector. Straight collector walls have the disadvantage of the need for additional collector coils however, the mechanical design of the collector is significantly simplified combined with a

more manageable smaller radial dimension. The additional collector coils can be normal conducting and have a simple axisymmetric geometry, thus are easy to built and operate.

In the straight wall design, the challenging factor with additional collector coils is the strength of the magnetic field that has to be produced to keep a constant beam radius in the $\vec{E}\times\vec{B}$ drift region. In the first prototype, normal conducting coils should be used, which are increased in weight with the magnetic field strength. In the efficiency optimized collector design, a beam radius of 130 mm is chosen as compromise between the collector coil demands and the size of the collector electrodes. An inner collector radius of 152 mm is possible. The bottom position of the $\vec{E}\times\vec{B}$ drift region is placed at an elevated position due to the confinement of the electron beam by the gyrotron magnet. The spent electron beam is slowly increased in its radial dimension while a fast increase by an additional coil or ferromagnetic structure would result in a non-adiabatic transition of the electrons. A non-adiabatic transition is observed when the slow electrons manage to further follow the magnetic field lines, while the fast electrons continue their previous trajectory with only little disturbance. The result is an increased beam thickness in the $\vec{E}\times\vec{B}$ drift region which complicates the optimization of the collector design.

Mechanical Optimization

The collector designs with azimuthal electric field shown so far are only electrically optimized and mechanical design considerations are not done. From the electrical point of view, it is important to keep the correct inner radius at the electrode and depth of the helical gap. The simplest idea is a cylindrical pipe with a thick wall, that is separated with the desired shape. In Ref. [18], a mechanical design for the cylindrical design with conical wall for a 1 MW 170 GHz is presented that is planed with a construction of metal sheets. However, the fabrication tolerances of a welded sheet metal structure are difficult to estimate and would require a great effort in the construction process, not speaking about the increased size of a collector for a 2 MW gyrotron. The efficiency optimized version shown in Fig. 2.13 is based on a thick wall pipe with hollowed recesses to reduce the weight of the electrodes. The downside of

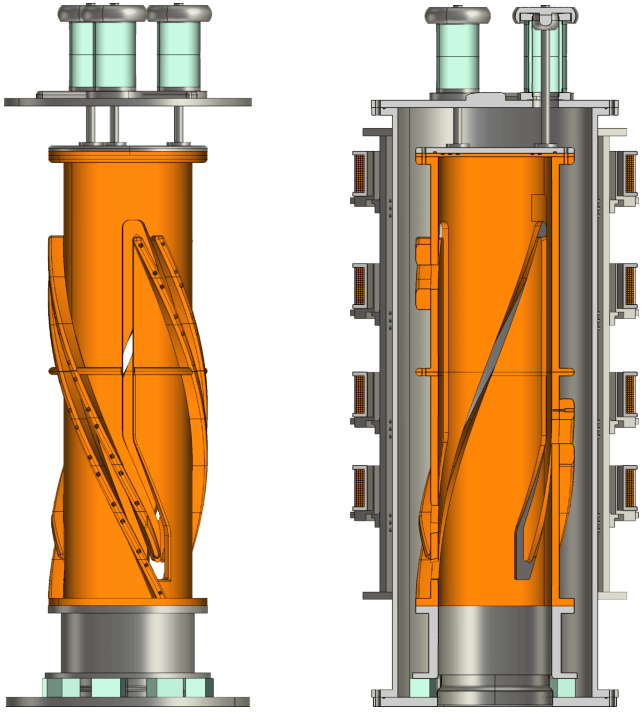

(a) Side view **(b)** Cut view

Figure 2.14: Mechanical design considerations of the efficiency optimized version.

this method is a high waste in material and processing time on the Computerized Numerical Control (CNC) machine which contributes to an unnecessary increase of the cost of the prototype.

The mechanical design consideration shown in Fig. 2.14 is based on a much thinner wall for the electrode pipe where helical extensions are screwed on to achieve the desired depth of the helical gap. The same applies for the flanges at the bottom, middle and top. The waste in material is significantly reduced by this solution. A vacuum housing is included in the design with an inner radius of 260 mm which is double the beam radius in the $\vec{E}\times\vec{B}$ drift region. The outer radius of the vacuum housing is set to 330 mm however, an outer radius

of 325 mm as the top flange of the mirror-box is sufficient to use the identical bolt-hole circle and vacuum seal as for the top of the mirror-box.

The inner radius for the additional collector coil core is set to 350 mm. It shall fit over the vacuum flanges at the top with their winding body. The height of each coil is set to 100 mm, while the thickness is not optimized. The total current of 35.5 kA·t (ampere-turn, current in single wire times the windings of the coil) is required to achieve the desired shape of the electron beam in the $\vec{E}\times\vec{B}$ drift region. At this point, an important parameter of the collector design is the weight of the additional collector coils. It is proportional to the volume of the copper coil core. The volume of the copper coil core V_{coil} is calculated to

$$V_{\mathrm{coil}} = \pi\ h\ d_{\mathrm{coil}}(2\ r_{\mathrm{in}} + d_{\mathrm{coil}}) \tag{2.6}$$

where the copper coil core has a height of h with an inner radius r_{in} and a radial thickness of d_{coil}. The thickness of the coil d_{coil} is directly proportional to the ampere-turns of each coil if the current density is kept constant and is much smaller than the factor of $2\ r_{\mathrm{in}}$.

2.4.2 Size Optimized Design

The collector size of the efficiency optimized design in the axial dimension is required, due to the voltage operation point of the collector with relatively small potential difference between both electrodes. The radial dimension of the collector is a consequence of the limitation of the normal conducting collector coils which would increase in size for a smaller beam radius and identical axial dimensions. The priority for the size optimized collector design, presented in this section, is a reduction of the radial dimensions in combination with a different voltage operation point to reduce both the weight of the collector electrodes and the additional collector coils. The fundamental designs for the mechanical design of the efficiency optimized design are also implemented for the size optimized design.

The electron drift velocity is increased with both, the potential difference between the electrodes and with the slope of the helical cut, thus with the length of the $\vec{E}\times\vec{B}$ drift region. An increase in the potential difference between

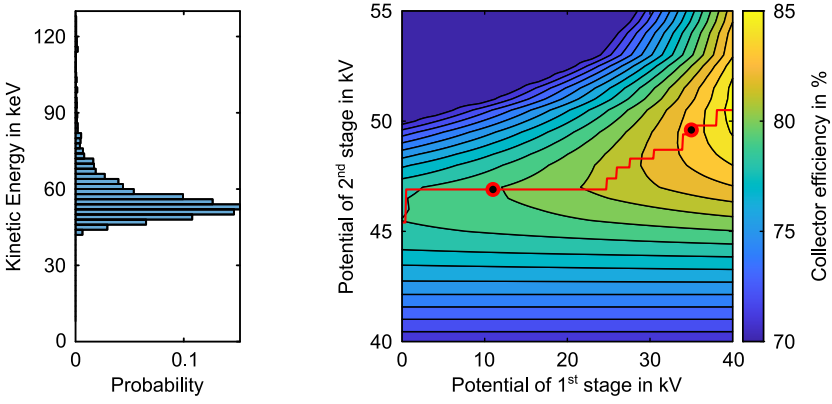

(a) **(b)**

Figure 2.15: (a) Kinetic energy spectrum of the spent electron beam of the KIT 2 MW 170 GHz coaxial-cavity gyrotron. (b) Theoretical maximum collector efficiency for different voltage operation points of a two-stage MDC based on the kinetic energy distribution.

both electrodes is compensated by a decrease in length of the $\vec{E}\times\vec{B}$ drift region, hence with a reduction in size of the overall collector. The maximum collector efficiency is calculated based on the kinetic energy spectrum of the spent electron beam as shown in Fig. 2.15a for an ideal two-stage MDC and is independent on a specific separation principle or collector geometry. It is shown in Fig. 2.15b over the applied potentials of the two stages. The voltage operation point of the efficiency optimized MDC is represented with the point on the right with depression voltages of 35 kV and 49.6 kV, giving a potential difference of 14.6 kV with a maximum theoretical collector efficiency of 83.5 %. On the other hand, for a size optimized collector design, a voltage of 11 kV at the first stage and 46.9 kV at the second stage would result in a potential difference of 35.9 kV and close to 80.0 % collector efficiency and is represented by the point on the left in Fig. 2.15a. This operation point is chosen to keep the maximum theoretical collector efficiency at around 80.0 %. The mechanical design considerations of the size optimized MDC are shown in Fig. 2.16 with a side and cut view. This version is optimized for the KIT 2 MW 170 GHz coaxial-cavity gyrotron operated in the 6.87 T magnet at KIT.

The length of the $\vec{E}\times\vec{B}$ drift region is significantly reduced for the second operating point with a potential difference of 35.9 kV down to approximately 0.6 m. For the efficiency optimized design with the first operation point,

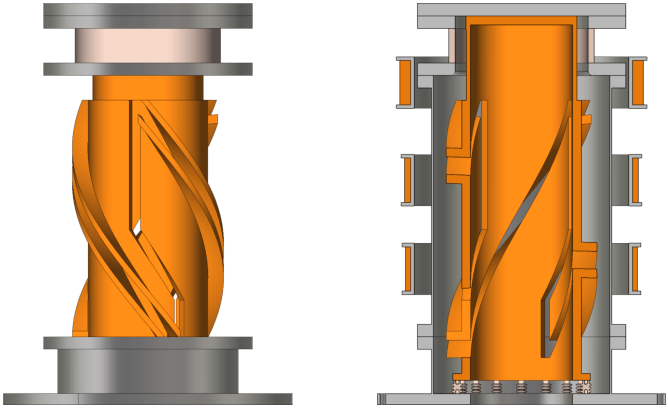

(a) Side view **(b)** Cut view

Figure 2.16: Mechanical design considerations of the size optimized version.

the length of the $\vec{E}\times\vec{B}$ drift region is at 1 m and the potential difference is at 14.6 kV, while the strength of the electron drift is in the same order of magnitude. The ratio of the electron beam radius to the inner radius of the collector wall is kept constant in both the efficiency and size optimized designs to avoid affecting the strength of the $\vec{E}\times\vec{B}$ drift. The strength of the $\vec{E}\times\vec{B}$ drift varies with distance from the electrodes due to changes in the electric field, being strongest in the helical gap and decreasing towards the axial center of the collector. The sensitivities against SMF and misalignment are also influenced by the ratio between electron beam radius and inner collector wall radius.

On one hand, the reduction in length of 40 % of the $\vec{E}\times\vec{B}$ drift region provides the possibility to increase the magnetic field strength in the MDC prototype without exceeding limits for the normal conducting coils. The result is a decreased beam radius and electrode radius. On the other hand, with the reduced beam radius, the start of the $\vec{E}\times\vec{B}$ drift region can be placed at a lower axial position, due to the fact that the beam radius is reached earlier in the diverging magnetic field of the gyrotron magnet. The result is a decreased axial length of the collector as the lower section is significantly reduced in size.

As a result of the decreased length of the collector from the efficiency to the size optimized design, it is possible to reduce the number of the additional collector coils from 4 to 3. The homogeneity of the magnetic field in the $\vec{E}\times\vec{B}$

drift region is not sacrificed, despite the smaller number of coils, due to the reduced length. The additional collector coils are also reduced in their radial dimensions from an inner radius of 350 mm to 250 mm, while the total current is only slightly reduced from 35.5 kA·t to 31.9 kA·t. The result are significantly lighter coils for the size optimized design as less material is required according to equation 2.6.

The insulator for the second electrode is placed around the cylindrical top section of the second collector electrode, while it is on the top for the efficiency optimized design. This change is possible due to the smaller electrode radius of the size optimized design. This design uses a single, larger insulator, which is more expensive. However, the cost is still acceptable, and the design is smaller and more robust. The total length of the size-optimized MDC with the single insulator is reduced to 0.9 m.

2.5 Summary

In this chapter, investigations on the requirements for the PSU configuration and design candidates for the first SP MDC prototype for high-power gyrotrons are presented. The size-optimized MDC is identified as the most promising concept for development and experimental validation. The size-optimized MDC offers a strategic balance between efficiency and practical design requirements, with a reduced collector size that allows easier fabrication and assembly compared to its efficiency-optimized counterpart.

The size reduction is achieved by optimizing the voltage operating point from previously a potential difference of 14.6 kV to now 35.9 kV. While maintaining a strong $\vec{E}\times\vec{B}$ drift, significant reductions in both axial and radial dimensions are achieved. The length of the $\vec{E}\times\vec{B}$ drift region is reduced from 1 m down to 0.6 m which is combined with a lower axial position of the $\vec{E}\times\vec{B}$ drift region to a reduced overall collector length of less than 1 m from over 1.6 m before. The reduced radial dimensions allow for a reduction of the inner coil radius from 350 mm down to 250 mm. The size-optimized design maintains a collector efficiency close to 80 %, which is comparable to the efficiency-optimized design. The choice of the size-optimized design is further justified by its lower requirement for additional collector coils and the reduced weight of the coils.

The focus on a size-optimized approach aligns with the experimental goals of KIT by providing a highly adaptable, less complex, and robust gyrotron MDC prototype. This orientation promises improved ease of implementation and cost-effectiveness, making it a viable and strategic choice for advancing gyrotron technology within existing infrastructure constraints.

3 A First Short-Pulse Multistage Depressed Collector Prototype

Experimental validation of the MDC concept in gyrotron operation is of utmost importance to provide a basis for the further development of improved MDCs. The physical principle of different designs with an azimuthal electric field is presented in chapter 2, while the design for the first MDC prototype is presented in this chapter. The complexity of the MDC is strongly dependent on the size of the electrodes, the manufacturability of individual parts, and the electric fields inside the collector. Considering all those factors, an MDC system is optimized in order to significantly reduce the manufacturing complexity of the first prototype. The theoretical design is discussed in section 3.1 starting with a breakdown of the individual design decisions for the electromagnetic configuration. It is followed by the magnetic field setup for MDC operation in section 3.1.1. The performance optimization of the electrodes is presented in section 3.1.2 with the power loading on the electrodes as a performance indicator for the optimization in section 3.1.3. The design of the thermal management is presented in section 3.1.4. The final step for the theoretical MDC design is the demonstration of the flexibility with the presentation of operation with different gyrotrons and frequency operation points in section 3.1.5.

The design for manufacturing and assembly is presented in section 3.2 with the modular mechanical design in section 3.2.1. The fabrication of the prototype is shown in section 3.2.2, followed by the assembly of the prototype in section 3.2.3. In the end of this chapter a summary is presented to conclude the design of the SP MDC prototype in section 3.3.

3.1 Electromagnetic Design

The fundamental physical design of a collector that is making use of an azimuthal electric field to separate electrons is presented in section 2.3.2 and 2.3.3 for the coaxial and cylindrical approach, respectively. It is concluded that the coaxial design has significant advantages from a physical point of view. However, for the realization of a first prototype the design is far more complex compared to the cylindrical approach. The fundamental characteristic of the coaxial approach is that half of the beam electrons drift inward and must therefore be collected in the inner structure. Hence, the design and construction of the inner structure must consider a substantial current and power delivered in combination with electrical insulation under vacuum condition. Therefore, the simpler cylindrical design is preferred for the first prototype to demonstrate the electron beam separation.

For the coaxial design in section 2.3.2, it is shown that multiple collector stages can be implemented in an MDC design with azimuthal electric field. However, in the course of simplifying the first SP MDC prototype, the number of depressed stages is also reduced to a minimum in order to keep the mechanical complexity within a reasonable limit. With each additional stage, the additional theoretical gain in collector efficiency is reduced as shown in the theoretical investigation in table 3.1. In result, the largest efficiency gains are achieved for the steps from non-depressed to one- and two-stage collectors. Collectors with three or more stages may provide benefits for a CW MDC due

Table 3.1: Theoretical maximum collector efficiency over the number of collector stages, based on the spent electron beam of the KIT 2 MW 170 GHz coaxial-cavity gyrotron.

Collector stages	**1**	**2**	**3**	**4**
Max. collector efficiency	62.3 %	83.5 %	88.6 %	91.3 %
Potential stage 1	35.0 kV	35.0 kV	35.0 kV	35.0 kV
Potential stage 2	-	49.6 kV	46.9 kV	46.9 kV
Potential stage 3	-	-	54.0 kV	52.1 kV
Potential stage 4	-	-	-	61.1 kV

to reduced cooling requirements with the increased efficiency. The most challenging part in the design of an $\vec{E}\times\vec{B}$ MDC with, for example 3, or 4 stages, can be seen in the differences of the theoretical optimum potentials. Those potential differences are decreasing, reducing the $\vec{E}\times\vec{B}$ drift, and are irregular between the different stages. A variation in the helical slope in between the electrodes would be required to achieve a constant $\vec{E}\times\vec{B}$ drift for all collector electrodes.

Another fundamental simplification concerns the shape of the electrodes. As mentioned in the previous chapter, the shape of the electrodes depends on the chosen magnetic field in the collector region in order to achieve a constant relative distance between the electron beam and the collector wall. For compactness in the radial direction, a cylindrical electrode shape is preferable if compared to a conical shape. The collector size in the axial direction depends on the minimum electrode radius, since the spent electron beam must first be expanded to the appropriate radius in order to achieve the desired relative distance from the collector wall. Therefore, a conical collector can be more compact in the axial direction than a cylindrical collector with the average radius of the conical collector. A mixture of a conical lower part and a cylindrical upper part is also possible and would be a promising concept for a CW MDC. The inner radius of an SP collector is usually rather compact, therefore the difference in axial size from a cylindrical to a conical collector is not significant. Since simplification is the primary concern for the SP MDC, radial compactness is preferred and a pure cylindrical electrode design is chosen. An appropriate candidate for the basic collector design is already presented in section 2.3.3 with the size optimized design. However, as mentioned it is optimized for the KIT 2 MW 170 GHz coaxial-cavity gyrotronin the 6.87 T magnet. As presented in section 2.2 a new cryogen free superconducting magnet must be used for experiments in the FULGOR test-stand at KIT. In this section, the collector design is adapted and optimized for the magnetic field profile of the 10 T magnet.

3.1.1 Collector Coil Design

Normal conducting coils are used on gyrotron collectors for modification of the stray magnetic field of the superconducting magnet. In most cases, those coils are operated with time varying current to modify the position of intersection

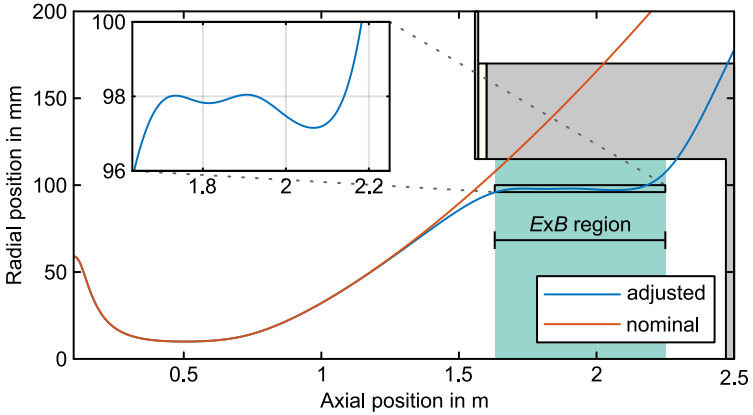

Figure 3.1: Magnetic field line of the beam center for nominal magnetic field without collector coils and for adjusted magnetic field with collector coils starting at the emitter.

of the spent electron beam with the collector wall over time (electron beam sweeping presented in section 1.4.2).

A constant beam radius in the $\vec{E}\times\vec{B}$ drift region is required for operation. It is achieved by applying a constant magnetic field. However, the stray magnetic field of the gyrotron magnet is reduced as the axial distance to the cavity increases. The reduced magnetic field results in an increase of the beam radius as it is calculated by applying the Bush theorem in equation 1.16. For the SP MDC prototype, three normal conducting homogeneous cylindrical coils around the collector provide a homogeneous magnetic field in the collector region. The freedom of the magnetic field profile is quite limited with a set of just three coils, and thus the coils are manually optimized based on the magnetic field line of the beam center starting at the emitter. The nominal magnetic field line and the adjusted magnetic field line are shown in Fig. 3.1.

The initial axial position of the $\vec{E}\times\vec{B}$ drift region is increased with the desired beam radius as long as no strong compensation coils and no magnetic shielding are implemented, due to the increasing radial position of the magnetic field line in axial direction. In section 2.3.3 in which the transition of the efficiency optimized design to the size optimized design is described, this effect is briefly mentioned as a result of the reduction in beam radius from 130 mm to 98 mm. The beam radius of 98 mm is chosen arbitrarily, however with increased beam

radius all radial dimensions of the collector are increased. For all three coils, the inner coil radius is set to 250 mm for compatibility to the remaining MDC components while the coil height is set to approximately 107 mm and the coil thickness to 18 mm to 31 mm. The adjusted beam center line is achieved with a total current in the collector coils of 30.0 kA·t as shown in Fig. 3.1, which is the combination of 7.4 kA·t in the two smaller lower coils and 15.2 kA·t in the larger upper coil. The current density in the two lower and thinner collector coils is at 3.84 A mm^{-2} while for the thicker upper coil it is at 4.55 A mm^{-2} if a solid rectangular copper block is assumed for the cross-section. Such current densities are too high for continuous operation of an uncooled normal conducting coil. This is addressed in the thermal management in section 3.1.4.

3.1.2 Tolerance Analysis of the Parametric Collector Electrodes

The tolerance analysis of the SP MDC prototype geometry is divided into (i) the parametric definition of the geometry, (ii) the tolerance analysis, and (iii) the optimization of the voltage operation point.

The content of this section has already been published in Ref. [93].

Parametric Definition of the Collector Electrodes

Equation 2.5 describes the helical surface of the basic MDC design in Cartesian coordinates. The first step in the tolerance analysis of the SP MDC prototype is a parametric representation of the helical surface with a few additional parameters. The helical surface of the first electrode is defined as

$$\begin{aligned} x(u,v) &= (R + d_{\mathrm{helix}}\, u)\, \sin(v\, \theta_{\mathrm{helix}}) \\ y(u,v) &= (R + d_{\mathrm{helix}}\, u)\, \cos(v\, \theta_{\mathrm{helix}}) \\ z(v) &= z_{\mathrm{ExB}} + (h_{\mathrm{ExB}} - h_{\mathrm{helix}})\, v \end{aligned} \tag{3.1}$$

in a Cartesian coordinate system with the basis vectors x, y and z. Parameters under investigation are the inner electrode radius R, the depth of the helical

surface in radial dimension d_{helix} and the azimuthal coverage angle of the helical surface θ_{helix}. The initial axial position of the $\vec{E}\times\vec{B}$ drift region z_{ExB}, the height of the $\vec{E}\times\vec{B}$ drift region h_{ExB} and the height of the helical gap h_{helix} are required for the parameterization of the axial z coordinate of the helical surface. The axial distance between the helical surface of the first and second electrode is equal to h_{helix}. The range for the surface parameters u and v is set to [0, 1]. The azimuthal coverage angle of the helical surface is defined as

$$\theta_{\mathrm{helix}} = \frac{2\pi}{3} + \theta_{\mathrm{over}} - \theta_{\mathrm{straight}} \tag{3.2}$$

with the azimuthal overlap angle of the helical surface θ_{over} defines the extension of the helix and the azimuthal coverage angle of the straight cut $\theta_{\mathrm{straight}}$. The division of the complete circular angle of 2π by 3 is done for a collector design with a three-fold helix as it is described in the references [76, 77, 91, 94] and in section 2.3.3. The initial electron beam radius in the $\vec{E}\times\vec{B}$ drift region is set to 98 mm, primarily as a compromise in the required magnetic field, and an acceptable size of the collector electrodes and coils. It is discussed in section 3.1.1. The magnetic field profile in the $\vec{E}\times\vec{B}$ drift region is, according to the desired electron beam radius, constant for the design optimization of the prototype. The electron beam radius at the entrance of the $\vec{E}\times\vec{B}$ drift region must be at the nominal design value. Hence, z_{ExB} is constant for a constant magnetic field profile. The helical depth d_{helix} is not important for electrical performance. However, it must be ensured that the slow electrons are collected on it and do not escape the helical gap. This is discussed in section 3.1.3. The last parameter for the parametric definition of the SP MDC prototype, which is not included in equation 3.1, is the height of the bottom straight cut h_{straight}. All parameters of the geometric study are shown graphical in Fig. 3.2.

Tolerance Analysis

The design of the SP MDC prototype is achieved with empirical optimization due to the high degree of freedom. However, a systematic parametric investigation of the geometry based on equation 3.1 is performed for validation of the design decisions and tolerance analysis of individual parameters. For simplification of the analysis, only a single parameter is changed at a time with

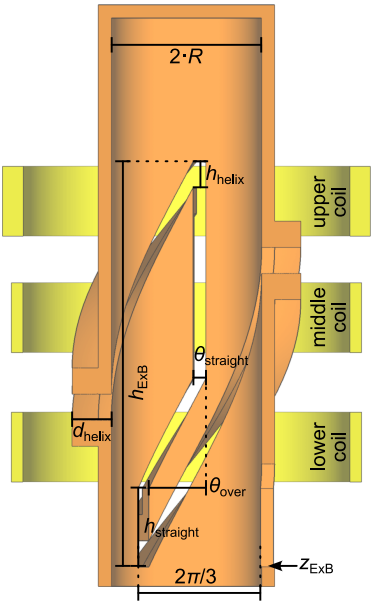

(a) 2D view

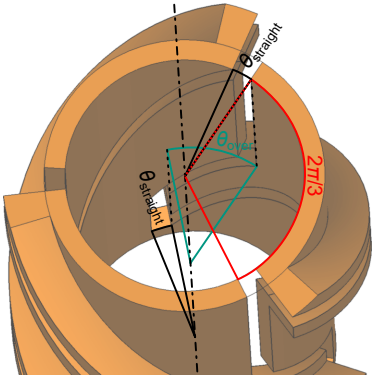

(b) 3D view

Figure 3.2: Graphical representation of the parametric definition [93].

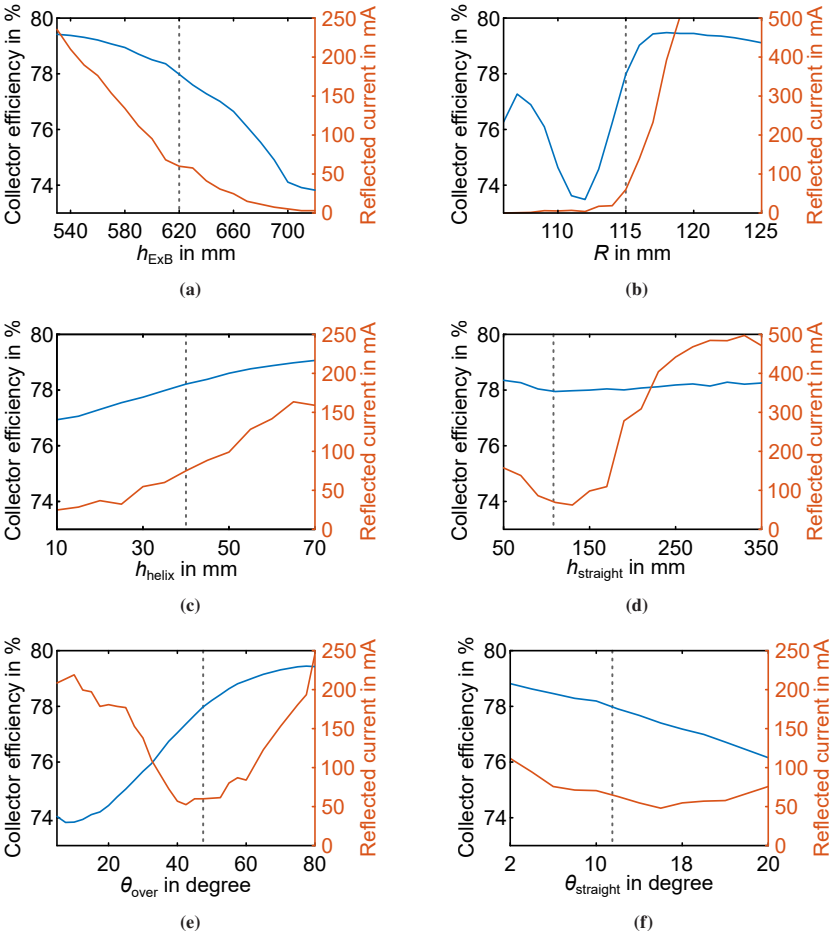

Figure 3.3: Parametric optimization for the SP MDC prototype with nominal values marked by gray dotted lines. (a) Variation of the height of the $\vec{E}\times\vec{B}$ drift region h_{ExB}, (b) the inner electrode radius R, (c) the height of the helical gap h_{helix}, (d) the height of the bottom straight cut h_{straight}, (e) the azimuthal overlap angle of the helical surface θ_{over} and (f) the azimuthal coverage angle of the straight cut $\theta_{\mathrm{straight}}$ [93].

all other parameters at their nominal value. The voltage operating point of the collector is considered constant for the parametric analysis and is based on a theoretical analysis of the spent electron beam. The goal is a maximum $\vec{E}\times\vec{B}$ drift, thus potential difference between the electrodes, while the theoretical collector efficiency is at approximately 80 %, based on the kinetic energy spectrum of the spent electron beam. The closest voltage tabs of the PSU at the KIT FULGOR test-stand [82] to meet those requirements, while the gyrotron body is at ground potential, are 11.25 kV and 46.125 kV for the first and second electrode, respectively. A depression potential of the first electrode close to the kinetic energy of the slowest electron could introduce two limitations, one related to the voltage depression of the electron beam and the other related to a reduced potential difference between both electrodes.

The results of the parametric investigation are shown in Fig. 3.3 with values for the collector efficiency and the reflected current. The collector efficiency η_{col} is defined in equation 1.7. The reflected current is a result of the parasitic behavior of the straight connection of the two helical ends and should be kept to a minimum. Reflected electrons are most likely to return to the cavity where they could gain energy from the electromagnetic wave [35], are reflected again, and are collected at a collector electrode. However, the interaction might be disturbed or parts of the gyrotron might be bombarded for which they are not intended. The reflected current presented in this paper is recorded in the lower launcher region at the boundary of the simulation, as the simulations do not include cavity interactions.

In case of the height of the $\vec{E}\times\vec{B}$ drift region h_{ExB} as shown in Fig. 3.3a, both, the collector efficiency and the reflected current are increased with reduced height of the $\vec{E}\times\vec{B}$ drift region. For h_{ExB} a compromise is chosen for which the reflected current is acceptable, and the collector efficiency is at an optimum level. This last parameter depends on the voltage operating point of the collector, more specifically, on the difference in the voltages between both electrodes. However, the voltage operating point is considered constant and is investigated in section 3.1.2 for the final design.

In case of the inner electrode radius R, as shown in Fig. 3.3b, the reflected current increases quickly for a radius larger than the nominal value. For smaller electrode radii, the collector efficiency is decreased, and the sensitivity to misalignment and SMF is increased. This parameter is strongly influenced by the electron beam radius in the $\vec{E}\times\vec{B}$ drift region.

In case of the height of the helical gap h_{helix} as shown in Fig. 3.3c, the opposite behavior as for h_{ExB} is observed. A compromise is chosen to limit the reflected current and still achieve an acceptable collector efficiency. On one hand, a minimum distance between both electrodes is required to limit the electric field and to prevent arcing during operation. On the other hand, sufficient strength of the electric field is desired to collect the electrons at fixed positions and prevent escaping of (secondary) electrons to the outside.

The height of the bottom straight cut h_{straight} is one of two parameters presented here which are introduced together with the helical extension. The influence of h_{straight} on the performance of the MDC is shown in Fig. 3.3d. It can be seen that the reflected current is minimized without a significant influence to the collector efficiency. The azimuthal overlap angle of the helical surface θ_{over} as shown in Fig. 3.3e is the second parameter which is introduced together with the helical extension. Here, a minimization of the reflected current is observed. However, a larger influence on the collector efficiency exists. The influence to the collector efficiency and rising reflected current with increased azimuthal overlap angle is a result of the single parameter observation. With increased overlap, the overall helical slope is decreased, resulting in a similar behavior as a reduced height of the $\vec{E}\times\vec{B}$ drift region.

In case of the azimuthal coverage angle of the straight cut $\theta_{\mathrm{straight}}$ as shown in Fig. 3.3f, a compromise between a low reflected current and high collector efficiency is chosen. In summary, all geometrical parameters are set to a compromise and show a wide resilience against geometrical tolerances. Manufacturing tolerances in the range of mm are uncritical. It can be concluded that all parameters studied are not sensitive to the collector performance and a variation of mm up to cm is acceptable for prototype operation. The most sensitive parameter is the inner electrode radius R which can be compensated with the electron beam radius in the $\vec{E}\times\vec{B}$ drift region by modification of the magnetic field in the collector.

Optimization of the Operation Point

After parametric analysis of the MDC prototype, an investigation of the different voltage operating points for the fixed geometry is performed. The expected collector efficiency and reflected current are subject to change if the depression

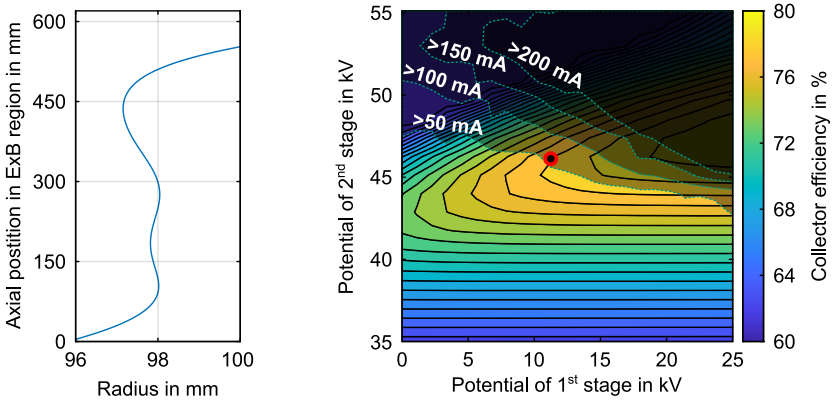

Figure 3.4: Analysis of voltage operating point of the optimized MDC prototype geometry. (a) Magnetic field line of the beam center in the $\vec{E}\times\vec{B}$ drift region. (b) Simulated collector efficiency with nominal voltage operating point [93].

potentials are varied. The collector potentials and magnetic field in the collector can be changed during experiments. The magnetic field line of the beam center in the $\vec{E}\times\vec{B}$ drift region as shown in Fig. 3.4a is used for the analysis of the collector potentials with the results shown in Fig. 3.4b. The range of the axial position of the bottom helix is between 0 mm to 580 mm, while it is between 40 mm to 620 mm for the upper helix. The collector efficiency is represented by iso-efficiency-lines while the reflected current is represented with an overlay of a few iso-reflected-current-lines and shadows. The region below a reflected current of 50 mA is considered safe for operation, while a reflected current above 200 mA should be avoided. The nominal voltage operating point with depression potentials of 11.25 kV and 46.125 kV is not optimal. A slight adjustment of the potentials to 13.5 kV and 45 kV could be considered to increase the collector efficiency to 78.8 % and decrease the reflected current to 51 mA. However, it should be noted that the difference in the voltages between both electrodes and with it the strength of the $\vec{E}\times\vec{B}$ drift is decreased by around 10 % by using the more optimal voltage operating point.

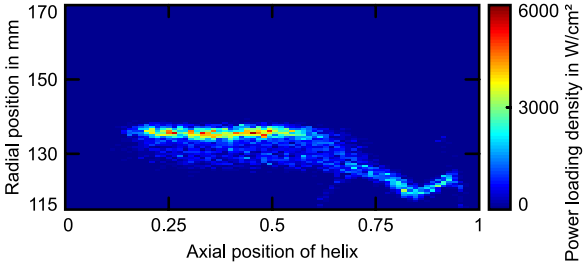

(a) First stage

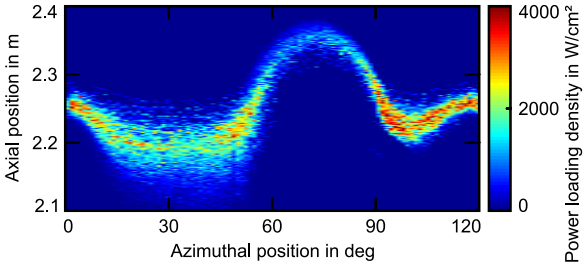

(b) Second stage

(c) 3D sketch of first stage

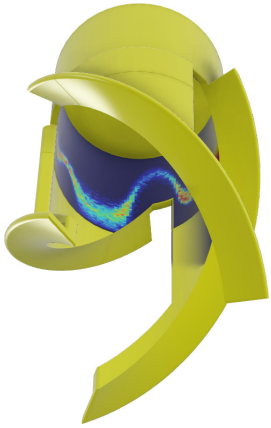

(d) 3D sketch of second stage

Figure 3.5: Power loading densities at the first stage (a) and second stage (b) of the SP MDC [91]. The helical surfaces of the first stage are projected to a 2D plane with their radial and axial positions. The unwrapped cylindrical surface of the second stage is only shown in a 120° segment due to the symmetry condition of the threefold design. Representation of the power loading on a 3D model for first (c) and second stage (d).

3.1.3 Thermal Loading of the Electrodes

At first glance, the power density of the collected electron beam on the surface of a SP collector seems to be irrelevant since a significant temperature change will not occur during SP operation. However, the power loading densities on the electrodes of an MDC with an azimuthal electric field can be used for a visual representation of the optimization of a collector design to different gyrotron operation scenarios. It is also important to ensure that the electron beam is not concentrated and that the peak power loading of the wall is within the limits of current SDCs. For a later comparison, the maximum power loading density of the verified SP SDC for the KIT 2 MW 170 GHz coaxial-cavity gyrotron is at 6 kW/cm^2 with a depression potential of -35 kV and a maximal acceptable pulse length of 50 ms [91].

While the power loading of the electrodes of classic collectors can be easily calculated by 2D tools due to the symmetry condition, it is more complicated for an MDC considering the complex 3D structure. In the past [75], a built-in function of CST was used to import the result of the trajectory simulation into a heat transfer simulation. However, this method depends on the mesh size of the trajectory simulation which limits the resolution of the power loading at the collector surface. A MATLAB tool is developed which extracts the raw trajectory data from CST and is used to calculate the power loading on both stages. In this way it is possible to achieve stable results, independent of the mesh of the tracking solver.

The power loading density on the first stage of the SP MDC prototype is generated on three identical helical surfaces, which are projected to one 2D plane as shown in Fig. 3.5a. The thermal loading is concentrated on a thin line with a thickness of only a few millimeters from bottom to top of the helical surface. The radial position of the electrons hitting point on the electrodes depends on the strength of the $\vec{E}\times\vec{B}$ drift. The long line with constant radial position is a good indication of a well optimized design as the electron drift and beam radius must be constant in the $\vec{E}\times\vec{B}$ drift region. The thickness of the line, is the result of the geometric optimization of the MDC design to the voltage between the two electrodes. The radial position of the power loading on the helical surface proofs that a sufficient depth of the helical surface d_{helix} is required. In the case that the helical depth is excessively wide, the outer radial dimension of the electrodes increases, thereby increasing the dimensions

of the vacuum housing and collector coils. Conversely, in the event of a helical depth that is excessively narrow, the electrons would be unable to be collected in the helical gap, while in a less extreme case, this would only affect secondary electrons. Fortunately, the most critical slow secondary electrons are collected close to the origin point due to the high electric field in the helical gap. For d_{helix} of the final design, a value of 55 mm is chosen for a compromise in compact dimensions and a safety margin for secondary electrons.

The power loading density on the cylindrical surface of the second stage is shown in Fig. 3.5b. A 120° segment is shown due to the symmetry condition of the triple helix design. The axial position of the thermal loading varies azimuthally due to the different directions of the radial electron drift caused by the azimuthal electric field component E_θ of the helical and straight cut as well as the helical extension at the bottom of the $\vec{E}\times\vec{B}$ drift region. The power loading at both collector electrodes are projected onto the corresponding surfaces of a 3D model to provide a direct visual interpretation of the results and are shown in Fig. 3.5c and Fig. 3.5d. The maximum power loading density on the first and second stage is below 6 kW/cm^2 and 4 kW/cm^2, respectively. In comparison, the power loading density of the SP SDC for the KIT 2 MW 170 GHz coaxial-cavity gyrotron is also at 6 kW/cm^2. The MDC power loading density is in a safe range for SP experimental verification.

3.1.4 Thermal Management of the SP MDC

Usually, the thermal management of SP gyrotron components is not a concern in operation. On the other hand, the MDC SP prototype is more restricted in the thermal capabilities despite the fact of a significantly increased efficiency and thus lower thermal losses at the electrodes. The restrictions are caused by the simplification of the design considering the separated vacuum housing to ensure vacuum tightness and cost saving measures to avoid increasing costs. The first point is addressed by the thermal management of the collector electrodes while the second point is addressed by the thermal management of the additional collector coils.

Collector Electrodes

Even though the planned maximum SP operation time of the MDC prototype is only in the range of 3 ms, some energy is deposited in the collector electrodes in the form of heat. In contrast to today's SDCs, where the outside of the collector electrode is exposed to the surrounding air, the electrodes of the MDC prototype are either completely or for the majority surrounded by vacuum. It is inevitable that the energy deposited in the collector electrodes had to be considered in the design of the MDC and in the future experiments. During operation at the optimal operating point with the KIT 2 MW 170 GHz coaxial-cavity gyrotron, at depression potentials of −11 kV and −46 kV for the first and second stage, the power at the first stage is at 110 kW, while at the second stage it is at 750 kW. Taking 3 ms as target for the maximum pulse length, the total energy that is deposited in the first stage and second stage of the MDC are 0.33 kJ and 2.25 kJ, respectively. Simplifications are made for the estimation of the temperature increase of the electrodes during the experiments:

- Homogeneously temperature rise of the electrodes, due to the low pulse repetition rate.
- Perfect thermal contact between copper parts.
- Thermal isolation of copper from stainless steel, due to the low thermal conductivity of the steel.
- Negligible thermal radiation and convection.

According to the 3D model of the MDC prototype, of all copper parts of the first electrode have a volume of $6.7{\times}10^3$ cm^3, while all copper parts of the second electrode have a volume of $1.4{\times}10^4$ cm^3. The weight of both electrodes is calculated with the density of CuCr1Zr of 8.91 g/cm^3 [30] to 60 kg and 125 kg for the first and second electrode, respectively. The temperature increase of the electrodes depends on the repetition rate of the pulses and the specific heat capacity of the material. The specific heat capacity of CuCr1Zr is 0.37 kJ/kgK at 20 °C. It increases with temperature. At 20 °C, the temperatures after a single 3 ms shot are increased by 0.015 K on the first and 0.049 K on the second electrode. The temperature increase is accumulated after 10 min of operation with a 1 Hz pulse repetition rate to approximately 8.9 K on the first

and 29 K on the second electrode, which is far from any critical limit. However, it is crucial to ensure a thermal contact with the surrounding air.

Collector Coils

The collector coils are considered to be normal conducting multi-turn coils made from copper. Thermal losses of these collector coils have to be considered for a cost-effective and practical design due to the high current density of the coils. Thermal simulations of the multi-turn coils are performed in COMSOL to get the limiting factor in the coil design. The model of the coil is assumed to be rotational symmetric, which results in a single rectangular torus for each turn. Given the coil geometry, a 2D setup would be the choice for a significant reduction of the computational effort. However, due to the boundary conditions in COMSOL, a 3D geometry is required, although a small angular segment is sufficient and extended with the periodic boundary condition. A segment of 1° is chosen for an optimized mesh size. A larger angular segment would result in additional mesh cells, while a smaller segment would result in a smaller minimum mesh cell. The electrical insulation around a copper wire has a thickness of 60 µm to 85 µm on each side. For a wire with a thickness of a few millimeters, this results in a noticeable difference in cross sectional area and is included in the model. The electrical insulation is usually done with polyesterimide and/or polyamide-imide [95], with a thermal conductivity in the range of 0.24 W/(mK) to 0.54 W/(mK) [96]. For the worst case consideration, the thermal conductivity of the insulation is set to 0.24 W/(mK). The multi-physics *Joule Heating* is used in COMSOL which automatically includes the physics of electric currents and heat transfer in solids. The resistance in the wire is calculated by a linearized resistivity model based on the material properties. A current terminal is applied to one cutting surface of the coil segment and a ground boundary to the other cutting surface. This way it is possible to define a specific current of the complete coil. The heat source of the heat transfer physics is a volumetric loss density based on the result of the electromagnetic simulation.

The coil model for the $\vec{E}\times\vec{B}$ MDC SP prototype is inspired by the transverse sweeping coil of the W7-X gyrotron [38]. The sweeping coil is used for a simulation setup in order to get realistic values for the heat transfer coefficients. A rectangular wire is used with a cross-section of 2.24 mm times 3.55 mm

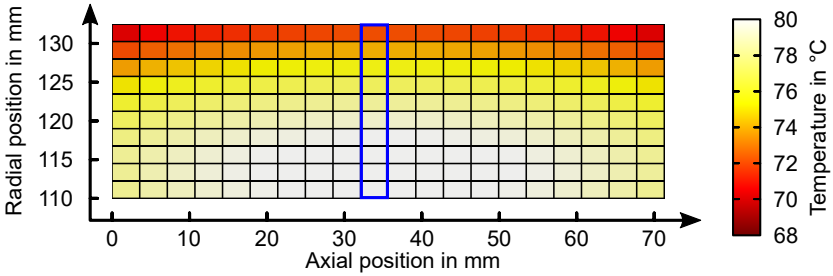

Figure 3.6: Temperature distribution in the transverse sweeping coil with one segment in the center of the coil marked in blue.

including the electrical insulation resulting in a copper cross-sectional area of 7.4 mm^2. This coil is built with 200 turns in 10 layers and is water cooled from the outer radial surface.

In the simulation, the elliptical coil is simplified to a round coil with an inner radius of 110 mm (average of the two radii of the ellipse) to obtain azimuthal symmetry in the simulation setup. The total resistance of the built coil is 0.36 Ω at 20 °C. The total resistance of the simplified coil is 0.3745 Ω at the initial temperature of 20 °C and increases to 0.459 Ω in stable cooled operation. The ohmic losses at 20 °C of the measured and simplified coils are 162 W and 164 W, respectively. In the model, the water-cooled and other outer boundaries are represented by two heat flux boundaries. The maximum operating temperature of the coil is 80 °C in the cooled configuration and 200 °C in the uncooled configuration. The two different heat transfer coefficients are tuned in the simulation to achieve the results of the experiments. The stable uncooled operation at 200 °C is achieved with a heat flux coefficient of 11 W/(m^{2}K) at all boundaries and an external temperature of 20 °C. The heat flux boundary at the cooled surface is changed to 50 W/(m^{2}K) to achieve a maximum temperature of 80 °C in cooled operation. These values are consistent with convective heat transfer and the heat transfer of simple water cooling [45].

The temperature distribution in the simplified transverse sweeping coil is shown in Fig. 3.6. The temperature in the cross-section of each winding is nearly constant, as it can be expected due to the high thermal conductivity of copper 385 W/(mK) [28]. The thermal gradient in the coil is concentrated in the thin layers of the electrical insulator. The maximum temperature in the stable

operation is 80.5 °C whereas the minimum temperature is 69.1 °C, resulting in a temperature difference of 11.4 K.

The limiting factor in the operation of a normal conducting coil is its maximum allowed operating temperature. The electrical insulator is most of the time the limiting material with a maximum acceptable temperature of 200 °C. The maximum temperature of the coil is in the mid-plane of the axis of symmetry at one of the inner layers of the coil. The temperature is slowly decreasing towards lower and higher axial positions.

The additional collector coils for the MDC SP prototype are designed to operate at a significantly higher current density than the transverse sweep coils of the W7-X gyrotron. The advantage is material savings with reduced weight and cost. The disadvantages are higher power consumption, lower thermal capacity and therefore shorter operating life time for similar cooling capabilities. The additional collector coils are considered only for pulsed operation and not for continuous operation as the transverse sweep coil. An air-cooled coil would also be possible, since the temperature rise during operation is more dependent on the thermal capacity than the relatively primitive water cooling. However, even simple water cooling can significantly reduce the cool down time and increase the duty cycle. The same principle of water cooling as for the transverse sweeping coil is considered for the additional collector coils.

All three additional collector coils are planned with the same inner radius of 250 mm and the same height of 106.5 mm, given by 30 windings times 3.55 mm. The three coils base on one thicker coil and two identical smaller coils, which only differ in the number of layers. This study will concentrate on the largest coil with the higher thermal loss and the reduced cooling capabilities due to the increased thickness. This coil will be operated between 13.0 kA·t to 17.0 kA·t depending on the gyrotron magnet and gyrotron operation point. The maximum and minimum temperatures after 15 min of operation in the coil with 13.0 kA·t and different number of layers are shown in Fig. 3.7a. A coil with 13 layers (390 turns) would be not sufficient for 15 min of operation at a starting temperature of 20 °C, due to the maximum acceptable temperature of the electrical insulator of 200 °C. Therefore, it is reasonable to set the minimum number of layers to 14 (420 turns) in order to achieve a 15 min operation time of the coils.

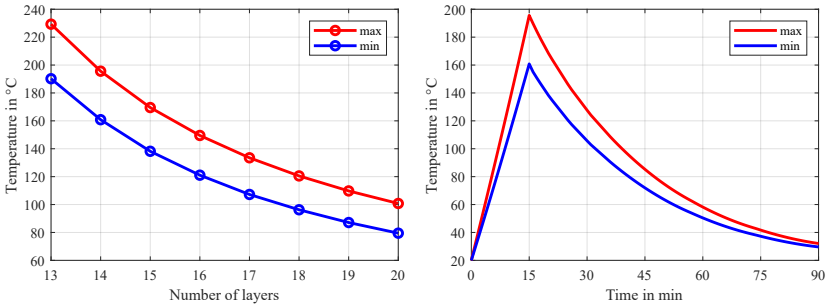

(a) Variation of layers **(b)** 14 layers over time

Figure 3.7: Minimum and maximum temperature in different coils for (a) variation of the number of layers and (b) for a coil with 14 layers over time (b).

The minimum and maximum temperatures in a coil with 14 layers over an operation time of 15 min and a cool down time of 75 min are shown in Fig. 3.7b. The temperature is increased nearly linearly during the operation due to the setup of the cooling. The power loss inside the coil linearly increases with the temperature starting with 3.3 kW at the initial 20 °C and going up to 5.5 kW after 15 min of operation at a maximum temperature of 196 °C. The cooling capabilities are dependent on the temperature difference ΔT between the coil and the outer boundaries (20 °C). The temperature decrease during the cool down is therefore faster for a large ΔT (directly after operation) and slower for a small ΔT.

3.1.5 Adaption of the SP MDC to Different Gyrotrons

The content of this section has already been published in Ref. [93].

The modular structure of the SP MDC prototype is a promising concept for future modifications of individual subcomponents without the need for reproduction of the complete MDC. Another benefit of the modular design is the adaptability of the MDC to a variety of different gyrotrons that are operated at various frequencies. With increased flexibility of the MDC, an earlier experimental campaign is feasible in case of unavailability of the optimized equipment as other non-optimized components like gyrotrons or magnets can be used for an enlargement of the possible experimental setups.

Table 3.2: Operation possibilities of the SP MDC prototype on different gyrotrons [93].

Operation Scenario	Gyrotron with Nominal Frequency	Operation Frequency	Magnet Nominal Field	Magnet Applied Field	Collector Beam Radius	Total Coil Current	Lower Coil Current	Middle Coil Current	Upper Coil Current
# 1	2 MW 170 GHz coaxial-cavity	170 GHz	10 T	6.9 T	98 mm	30 kA·t	7.4 kA·t	7.4 kA·t	15.2 kA·t
# 2	1.5 MW 140 GHz W7-X	105 GHz	4.2 T	4.2 T	98 mm 100 mm	24 kA·t 22 kA·t	5.6 kA·t 5.1 kA·t	6.7 kA·t 5.8 kA·t	11.4 kA·t 11.4 kA·t
# 3	1.5 MW 140 GHz W7-X	140 GHz	5.6 T	5.6 T	100 mm	22 kA·t	3.5 kA·t	6.0 kA·t	12.2 kA·t
# 4	2 MW 170 GHz coaxial-cavity	136 GHz	10 T	5.5 T	98 mm	27 kA·t	7.5 kA·t	6.2 kA·t	13.4 kA·t
# 5	2 MW 170 GHz coaxial-cavity	204 GHz	10 T	8.3 T	98 mm	34 kA·t	7.8 kA·t	8.6 kA·t	17.5 kA·t
# 6	2 MW 170 GHz coaxial-cavity	170 GHz	6.87 T	3.5 T	99 mm	17 kA·t	5.1 kA·t	3.0 kA·t	9.3 kA·t

The flexibility and robustness of the MDC is demonstrated through its adaptation from the KIT 2 MW 170 GHz coaxial-cavity gyrotron to the W7-X Upgrade SP gyrotron for 140 GHz operation in the designated 5.6 T SC magnet. However, it is also compatible with 105 GHz operation of the W7-X Upgrade SP gyrotron in a 4.2 T SC magnet, and multi-frequency operation as well as at different harmonics with the KIT 2 MW 170 GHz coaxial-cavity gyrotron. All operation scenarios which are investigated in this work are listed in table 3.2 and are described in detail in the following subsections.

Operation of the W7-X SP Pre-Prototype at 105 GHz

One possibility of SP MDC prototype operation is the adaptation to the 1.5 MW 140 GHz W7-X SP pre-prototype gyrotron operated in a 4.2 T SC magnet at a frequency of 105 GHz. The mechanical adaption is possible with a second version of the lower assembly with matching dimensions to the mirror-box, as shown in section 3.2.2. Due to the availability of other suitable magnets, it is decided to use this non-optimized mode because it is the first possibility at KIT for MDC verification with a MW-class gyrotron. The operation of the W7-X gyrotron in the 4.2 T magnet is possible however, the operation mode is limited to co-rotating modes with a magnetic field in the positive z-direction. Counter-rotating modes (against the electron rotation) with the same direction of the magnetic field are not possible due to the launcher design of the W7-X gyrotron, while a magnetic field in the negative z-direction is not possible due to the $\vec{E}\times\vec{B}$ drift. According to the $\vec{E}\times\vec{B}$ drift principle, the same collector geometry cannot be utilized for both magnetic field directions due to the change of drift direction. The majority of electrons would then drift to the inside with exception to the electrons at azimuthal position of the straight gap. An operating point with a less optimized co-rotating mode is chosen therefore to achieve a spread in the kinetic energy distribution of the spent electron beam for MDC experiments, which is shown in Fig. 3.8a.

Based on the kinetic energy distribution an analytic investigation is carried out to calculate the maximum collector efficiency at a range of depression potentials applied to both electrodes. The result is shown in Fig. 3.8b. In the investigation, reflected currents are neglected, and all electrons are collected with the least kinetic energy remaining. In the regime of a low depression potential of the second electrode, where no electrons are collected at the first electrode, the

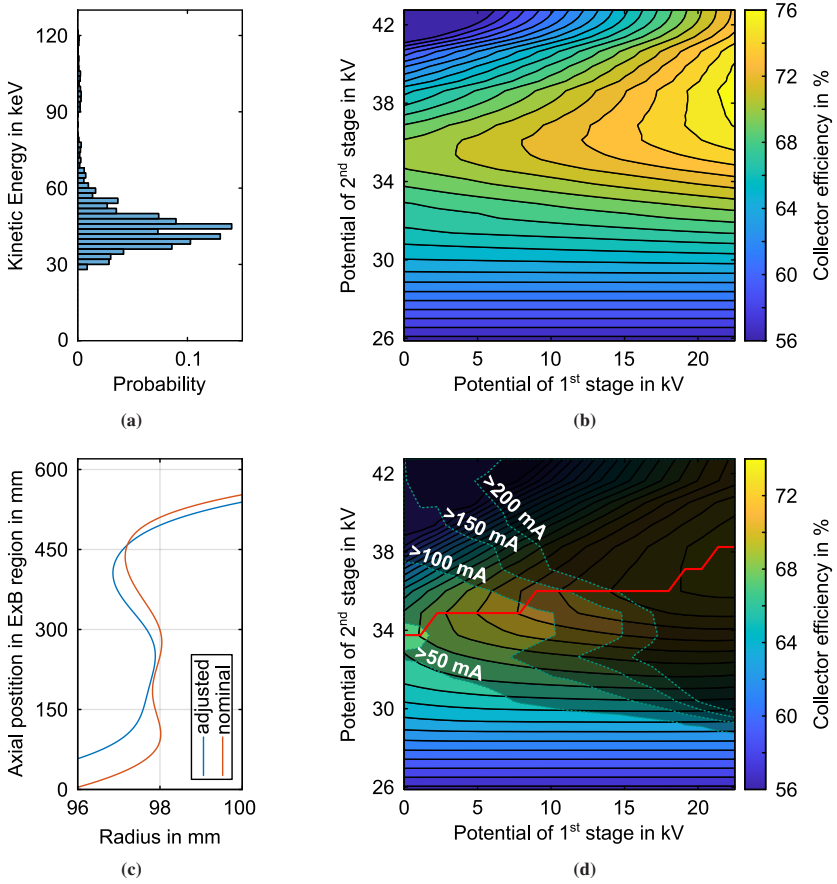

Figure 3.8: Adaption of the SP MDC to the W7-X Upgrade SP gyrotron operated in a 4.2 T magnet. (a) Kinetic energy spectrum of the spent electron beam. (b) Theoretical collector efficiency based on the kinetic energy distribution. (c) Magnetic field line of the beam center in the $\vec{E}\times\vec{B}$ drift region. (d) Simulated collector efficiency [93].

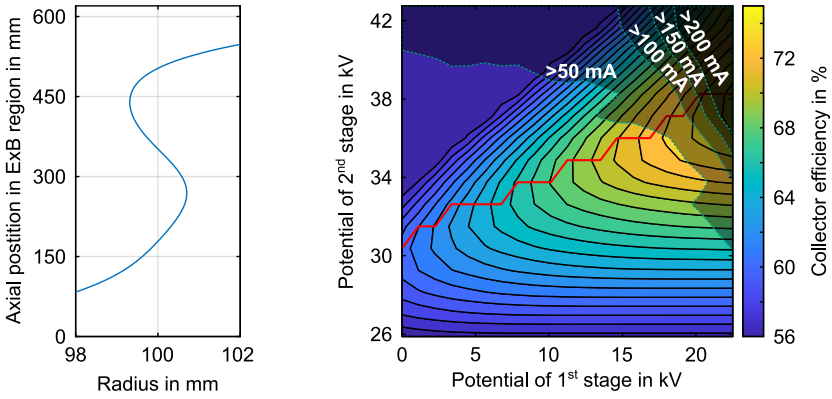

Figure 3.9: Optimization of the SP MDC operation with the W7-X Upgrade gyrotron at 105 GHz. (a) Magnetic field line of the beam center in the $\vec{E}\times\vec{B}$ drift region. (b) Simulated collector efficiency [93].

collector efficiency is not influenced by the potential of the first electrode. As the potential of the second electrode increases, a larger number of electrons is collected at the first electrode. Consequently, the collector efficiency is also influenced by the depression potential of the first stage.

A beam radius in the $\vec{E}\times\vec{B}$ drift region of 98 mm is considered for operation with the W7-X pre-prototype, which is identical to the KIT 2 MW 170 GHz coaxial-cavity gyrotron. The adjusted center line of the beam is shown in Fig. 3.8c and is achieved with the coil currents listed in table 3.2. It should be mentioned that a flat beam line as for the nominal case is not achievable with the fixed coil geometry and magnetic field profile of the 4.2 T SC magnet. The simulated results with a 98 mm beam radius are shown in Fig. 3.8d. Unfortunately, the majority of collector voltage operating points show a reflected current above 50 mA and a significant amount reach a reflected current above 200 mA. The expected collector efficiency is limited, as the most promising voltage operating points are probably not achievable in operation. Hence, the operation of the SP MDC with this magnetic field profile is not beneficial and must be optimized.

In order to optimize the magnetic field profile in the collector, it is essential to identify the limiting factor of the previous profile. A fixed potential of

the second electrode at a level where the potential of the first electrode does influence the collector efficiency, as indicated by the value of 34 kV, results in an increase in reflected current with the depression potential on the first electrode. In other words, the reflected current is reduced with an increased potential difference between both electrodes. For the case of mechanical optimization, a few options are possible to counteract the weak performance with an increase in the strength of the $\vec{E}\times\vec{B}$ drift. However, for electromagnetic optimization, a simple increase in the beam radius solves the issue. The improved magnetic field profile is adjusted to a beam radius of 100 mm, an increase of 2 mm to the nominal operation. The adjusted beam center line from Fig. 3.9a is achieved with the coil currents listed in table 3.2. The results with significantly reduced reflected current are shown in Fig. 3.9b. Collector efficiencies of 70 % to 71.5 % are achievable with maximum reflected currents between 50 mA up to 100 mA.

Operation of the W7-X SP Pre-Prototype at 140 GHz

The operation of the SP MDC in the W7-X Upgrade SP gyrotron at the nominal frequency of 140 GHz [49, 97, 98] is another possibility for MDC experiments at KIT. The gyrotron offers a microwave output power of 1.5 MW with a hollow cavity design and dense kinetic energy spectrum of the spent electron beam as shown in Fig. 3.10a. The theoretically calculated collector efficiency based on the kinetic energy spectrum is at high levels for a two stage MDC design as shown in Fig. 3.10b. The mechanical adaption of the MDC is identical to section 3.1.5.

The critical aspect of adaption of the MDC prototype to the W7-X Upgrade SP gyrotron is the magnetic field profile in the $\vec{E}\times\vec{B}$ drift region due to the faster diverging magnetic field lines of the different magnet and fixed positions of the additional collector coils. A beam center radius of 100 mm is chosen for this investigation as the reflected current of the collector is increased with a beam radius of 98 mm, similar to the operation at 105 GHz. The adjusted beam center line from Fig. 3.10c is achieved with the coil currents listed in table 3.2. The simulated collector efficiencies for a variety of collector potentials are shown in Fig. 3.10d. A collector efficiency of up to 77 % is achievable with a reflected current below 50 mA, while a collector efficiency of 80 % is achievable with a reflected current under 150 mA.

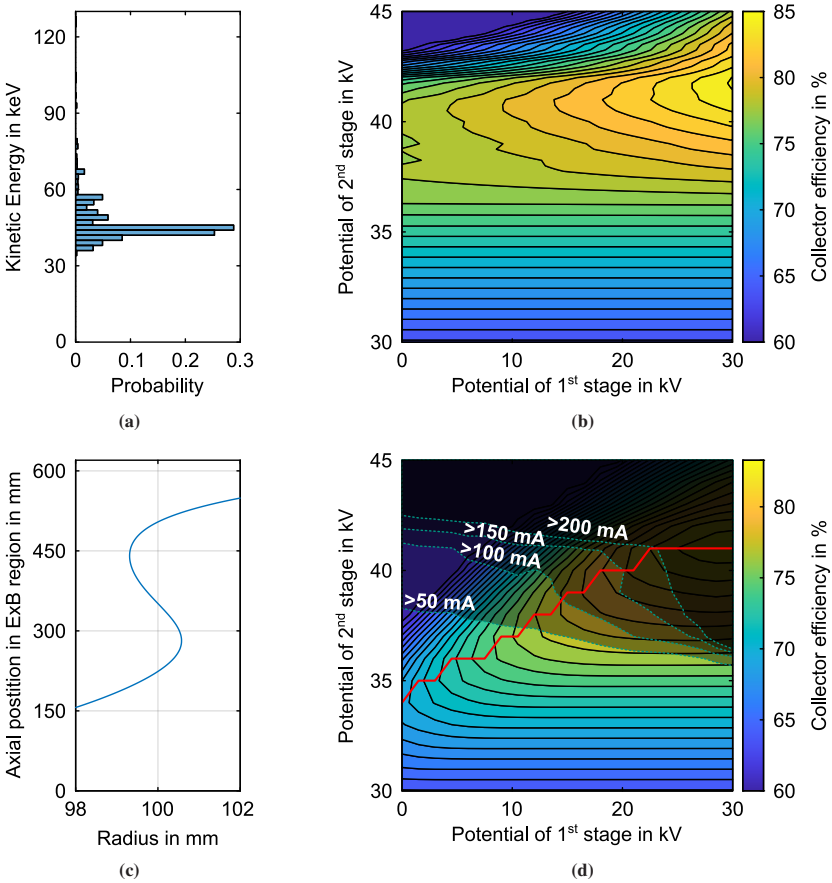

Figure 3.10: Adaption of the SP MDC to the W7-X Upgrade SP gyrotron operated at the nominal frequency of 140 GHz. (a) Kinetic energy spectrum of the spent electron beam. (b) Theoretical collector efficiency based on the kinetic energy distribution. (c) Magnetic field line of the beam center in the $\vec{E}\times\vec{B}$ drift region. (d) Simulated collector efficiency [93].

Operation in a Coaxial-Cavity Setup at 136 GHz

The KIT 2 MW 170 GHz coaxial-cavity gyrotron was studied in the past for extension to multi-frequency operation [99]. One of the considered frequencies is 136 GHz with the $TE_{28,15}$ mode which is co-rotating with the magnetic field in the positive axial direction. A switch to counter-rotating modes with a magnetic field in the negative axial direction is not possible with the fixed geometry of the SP MDC as described earlier and counter-rotating modes with a magnetic field in the positive axial direction would require a new launcher geometry. The advantages of a multi-frequency gyrotron is on one hand the universal application to different kinds of fusion machines and on the other hand, a possibility to modify the heating position in the plasma without moving parts.

Operation of the multi-frequency coaxial-cavity gyrotron at 136 GHz is foreseen in the 10 T SC magnet at KIT in the FULGOR test-stand. No mechanical adaption of the MDC is required due to operation with the nominal gyrotron and magnet. The kinetic energy distribution of the spent electron beam is shown in Fig. 3.11a and the theoretical maximum collector efficiency is shown in Fig. 3.11b. The spread in the kinetic energy distribution is higher compared to the nominal operation at 170 GHz and is a limiting factor in the maximum achievable collector efficiency. The identical beam radius of 98 mm as for the nominal operation is chosen for operation at 136 GHz with the beam center line shown in Fig. 3.11c. A close match of the beam line to the nominal operation is achieved due to the identical gyrotron magnet which is just operated with different currents. The coil currents are listed in table 3.2.

The simulated collector efficiencies for a variety of collector potentials are shown in Fig. 3.11d. A collector efficiency of up to 73 % is achievable with a reflected current below 50 mA, while a collector efficiency over 77 % is achievable with a reflected current below 150 mA.

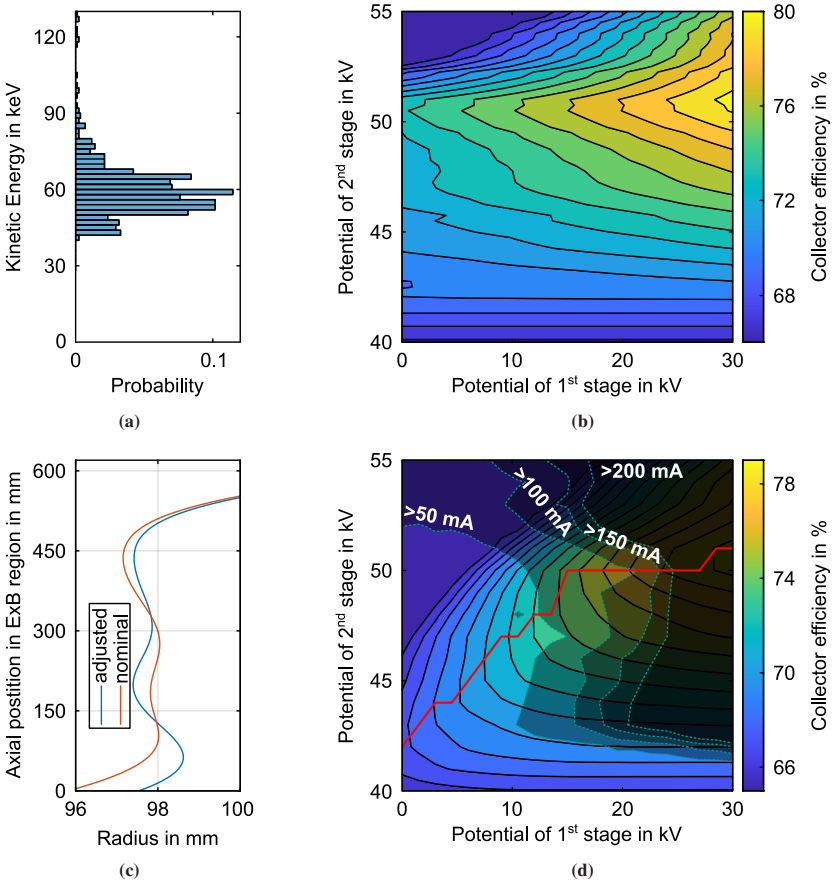

Figure 3.11: Adaption of the SP MDC to the 136 GHz coaxial cavity multi-frequency gyrotron operated in the 10 T magnet at KIT. (a) Kinetic energy spectrum of the spent electron beam. (b) Theoretical collector efficiency based on the kinetic energy distribution. (c) Magnetic field line of the beam center in the $\vec{E}\times\vec{B}$ drift region. (d) Simulated collector efficiency [93].

Operation in a Coaxial-Cavity Setup at 204 GHz

Similar to the operation of the KIT 2 MW 170 GHz coaxial-cavity gyrotron at 136 GHz multi-frequency operation was studied with extension to 204 GHz [99]. The co-rotating $TE_{40,23}$ mode was chosen as prime candidate for the coaxial-cavity gyrotron due to similar relative caustic radius of the mode compared to the nominal $TE_{34,19}$ mode. Operation is also foreseen in the 10 T SC magnet at KIT in the FULGOR test-stand, which eliminates the need for mechanical adaptation. A major difference of this operation point compared to the other cases are the characteristics of the spent electron beam kinetic energy spectrum as shown in Fig. 3.12a. The spectrum is widely spread and has a high probability of the slowest electrons in contrast to the reduced probability of the slowest electrons in other gyrotrons. Such an energy spectrum would require high collector depression potentials in order to achieve a high collector efficiency as shown in Fig. 3.12b. However, when both collector potentials of a two-stage collector are close to each other, the strength of the $\vec{E}\times\vec{B}$ drift is reduced.

A close match of the beam center line to the nominal operation is achieved due to the identical gyrotron magnet as shown in Fig. 3.12c. However, due to the increased magnetic field in the cavity, a higher magnetic field must be also applied in the $\vec{E}\times\vec{B}$ drift region to achieve the desired beam radius of 98 mm, again reducing the strength of the $\vec{E}\times\vec{B}$ drift. The coil currents are listed in table 3.2 and are significantly higher compared to the other gyrotrons presented in this work.

Despite the limitations of the kinetic energy spectrum and the increased magnetic field in the $\vec{E}\times\vec{B}$ drift region, a collector efficiency of 77 % is achievable with a reflected current below 50 mA and is not significantly improved if a higher reflected current is acceptable. All simulated voltage operating points are shown in Fig. 3.12d. It can be seen that the most optimum operation points can not be used with the existing MDC design, due to not strong enough $\vec{E}\times\vec{B}$ drift as expected from the theoretical investigation. The electron beam radius in the $\vec{E}\times\vec{B}$ drift region could be increased to increase the depression potential of the first electrode without affecting the reflected current, however, the expected improvement is not high when the theoretical maximum collector efficiency in Fig. 3.12b is considered.

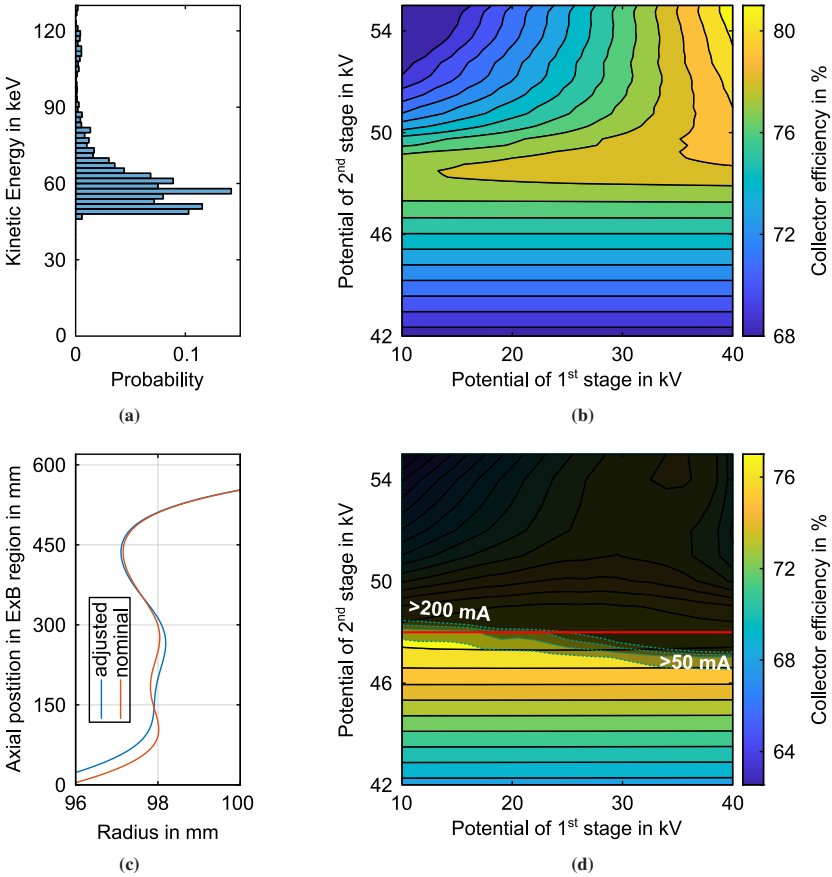

Figure 3.12: Adaption of the SP MDC to the 204 GHz coaxial cavity multi-frequency gyrotron operated in the 10 T magnet at KIT. (a) Kinetic energy spectrum of the spent electron beam. (b) Theoretical collector efficiency based on the kinetic energy distribution. (c) Magnetic field line of the beam center in the $\vec{E}\times\vec{B}$ drift region. (d) Simulated collector efficiency [93].

3.1.6 Adaption of the SP MDC to Higher Cyclotron Harmonics

Operation of a vacuum electron tube at the second harmonic of the electron cyclotron resonance frequency is a possibility for reduction of the required magnetic field in the cavity. Until now, high-power MW-class gyrotrons are operated at a fundamental mode however, investigations are currently ongoing for a gyrotron operated at the second harmonic with at least 1 MW output power at a frequency above 100 GHz [100–102]. The most significant disadvantage of gyrotron operation at a harmonic mode is a decreased interaction efficiency between the electron beam and the microwave. In order to compensate for this disadvantage, the utilization of an MDC is key to boost the overall tube efficiency to competitive values in comparison to gyrotrons operated at the fundamental frequency. As an example, based on equation 1.8 with an efficiency of the Quasi-Optical (QO) system of $\eta_{\mathrm{RF}} = 90\,\%$ and a collector efficiency of $\eta_{\mathrm{col}} = 80\,\%$, a total gyrotron efficiency of $\eta_{\mathrm{total}} = 50\,\%$ is achieved with an interaction efficiency of only $\eta_{\mathrm{int}} = 20\,\%$. Considering an increased interaction efficiency close to $\eta_{\mathrm{int}} = 25\,\%$, the total gyrotron efficiency would be at $\eta_{\mathrm{total}} = 56\,\%$.

At KIT it is currently studied to operate the 2 MW 170 GHz coaxial-cavity SP pre-prototype with slight modifications in the 6.87 T SC magnet at half magnetic field at 170 GHz. Gyrotron operation in the 6.87 T SC magnet is at the moment not foreseen in the FULGOR test-stand due to the cryogenic operation, which would be required for MDC implementation. However, from a physical point of view, there is no limitation, this operation point is the most up-to-date and most promising so far, and no mechanical adaptation of the MDC is required.

The kinetic energy distribution of the spent electron beam is shown in Fig. 3.13a and the theoretical maximum collector efficiency is shown in Fig. 3.13b. The minimum kinetic energy is much higher compared to the other gyrotrons shown in this work due to an increased acceleration potential and decreased interaction efficiency which results in increased collector efficiencies compared to fundamental gyrotrons. A beam radius of 99 mm is chosen for the first investigation with the beam line shown in Fig. 3.13c. The adjusted beam center line is achieved with the coil currents listed in table 3.2.

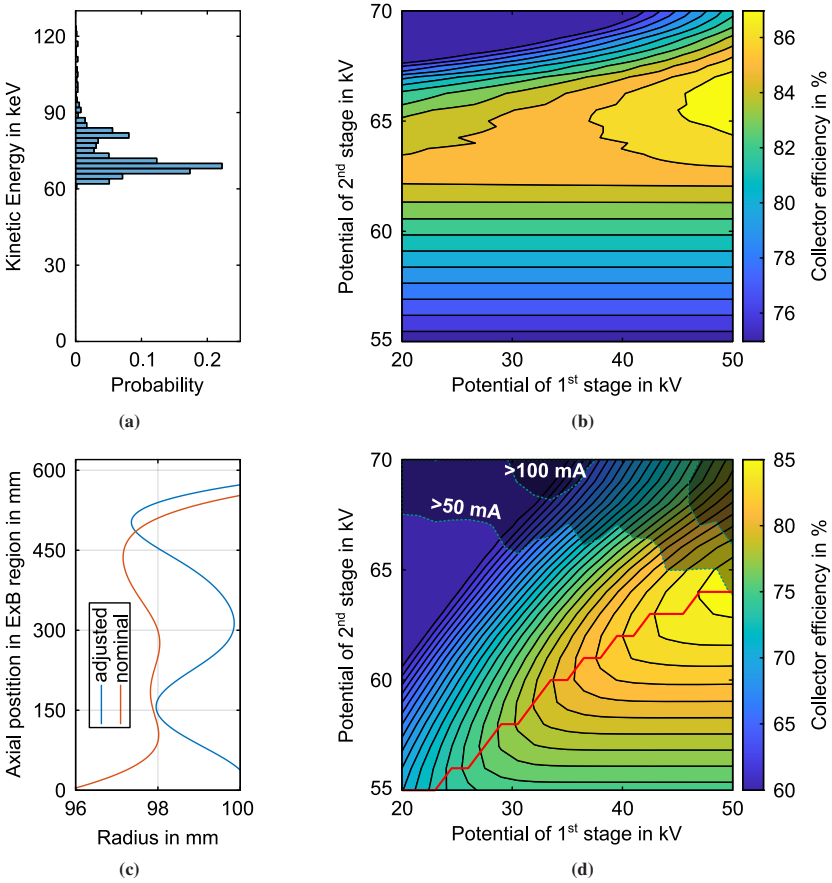

Figure 3.13: Adaption of the SP MDC to the 170 GHz coaxial cavity gyrotron operated in the 6.87 T magnet at KIT at the 2nd harmonic. (a) Kinetic energy spectrum of the spent electron beam. (b) Theoretical collector efficiency based on the kinetic energy distribution. (c) Magnetic field line of the beam center in the $\vec{E}\times\vec{B}$ drift region. (d) Simulated collector efficiency for different voltage operating points with different limits for reflected current [93].

In simulation, collector efficiencies of up to 85 % are achieved with low reflected currents below 50 mA which is close to the theoretical maximum. The results are shown in Fig. 3.13d. With reduced magnetic field in harmonic gyrotron operation a different MDC behavior is observed at high potential differences between both electrodes above 30 kV. At such operation points, the $\vec{E}\times\vec{B}$ drift is too strong and fast electrons (with kinetic energies above the deceleration potential of the second electrode) are collected at the first electrode with significant remaining energy, thus reducing the collector efficiency and significantly increasing the current collected by the first electrode. In order to operate the SP MDC prototype at such voltage operating points a decreased beam radius could be used with the disadvantage of increased levels of reflected current for the high efficiency operation points.

3.1.7 Stray Magnetic Field

Sources of SMFs in the proximity of gyrotrons in operation are avoided but not totally eliminated as already mentioned in section 1.4.3. In the operation with SDCs, a simple investigation of the magnetic field lines during a sweeping cycle is sufficient for a prediction of the influence of SMF to avoid electron collision at the top plate. The investigation of SMF in MDC operation is different, since the trajectories of the electrons are also influenced by the electric field in the $\vec{E}\times\vec{B}$ drift region. Electrons could be allowed to hit the top plate of the SP MDC, due to SP operation, however, the influence to the reflected current and collector efficiency must be studied. The influence on both parameters is not existent for an SDC in first assumption of primary electrons without space charge and is unavoidable in an MDC with azimuthal electric field based on the geometry.

The simulated collector performance of the SP MDC prototype is shown in Fig. 3.14 for constant radial magnetic field in the complete simulation volume. This approach is taken as worst-case approximation and is relevant for considerations of gyrotron placement nearby a tokamak. On one hand, the collector efficiency is only slightly influenced with the SMF in x- and y-direction of up to 500 µT. On the other hand, the reflected current is much more influenced by the SMF and exceeds the safe limit of 200 mA for radial magnetic field over 500 µT. In comparison, the limit of radial magnetic field for the EU CW ITER gyrotron is considered to approximately 200 µT [52]. If necessary, a different

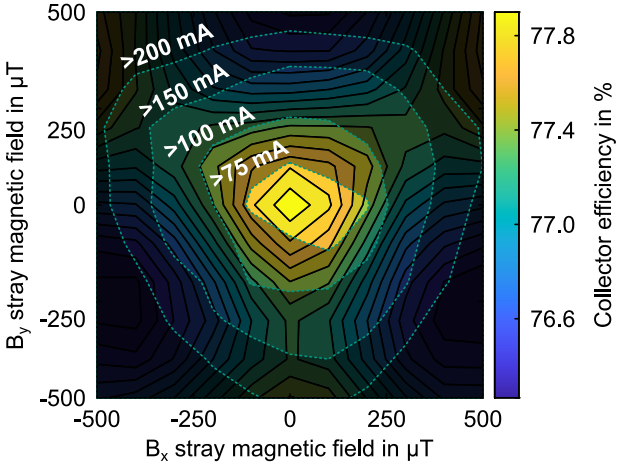

Figure 3.14: Simulated MDC prototype performance under the influence of a radial stray magnetic field.

voltage operation point of the collector could be used to further reduce the reflected current. It should be noted that even at a SMF of 500 µT in x- and y-direction no electrons where collected at the top plate.

Another source of SMF are neighboring gyrotrons in ECRH installations with a few to many tens of gyrotrons. The minimum distance between two gyrotrons is crucial for the efficient placement of the tubes, while the operation must not be influenced. A few key results of the MDC prototype operation with a second gyrotron at identical magnetic field profile placed in 3 m, 4 m and 5 m distance are shown in table 3.3. The safe limit of a reflected current of 200 mA is exceeded for a neighboring gyrotron in 3 m and the collector efficiency is slightly reduced, however even at this level, no electrons are collected at

Table 3.3: Simulated MDC prototype performance with the SMF of neighboring gyrotrons at different distances.

Distance	3 m	4 m	5 m
Collector efficiency	75.3 %	76.5 %	77.2 %
Reflected current	386 mA	104 mA	56 mA

the top plate. A gyrotron placed in 4 m could be operated and the option of a different collector voltage operation point with reduced reflected current also exists. The magnetic field of the neighboring gyrotrons is approximated as a single magnetic dipole according to section 1.4.3. The 10 T magnet is operated at reduced field for operation of the KIT 2 MW 170 GHz coaxial-cavity gyrotron and is modeled as a magnetic dipole with a magnetic moment of 410 kA m^2.

3.2 Design for Manufacturing and Assembly

Design for manufacturing and assembly represents a unified approach to product design that integrates two distinct methodologies: Design For Manufacturing (DFM) and Design For Assembly (DFA). DFM is the design of parts for ease of manufacture [103], while DFA is the design of a product for simple assembly [104]. Both approaches had to be considered for the mechanical design of the first $\vec{E}\times\vec{B}$ SP MDC prototype with helical electrodes due to the complex electrode geometry to ensure a reliable and robust prototype to make experiments.

3.2.1 Modular Mechanical Design

Basic ideas for the mechanical design of the SP MDC prototype are considered during the theoretical electrode design and optimization phase. One of those ideas is the implementation of a standardized ultra-high vacuum seal system for the modular subcomponents of the MDC. Standardized seals are a cost-effective and robust way to provide a stable vacuum for prototype components, which is on the highest priority for gyrotron operation. Due to the size of the collector, the ConFlat (CF) flange system is chosen in the size DN400 for the majority of the vacuum housing. The pipe sections for this flange size are possible with up to 400 mm inner diameter, while the outer diameter of the flange is at 469.9 mm. At those dimensions it is possible to insert the collector electrodes with an inner radius of 115 mm and an outer radius of 170 mm as well as to mount the external collector coils with an inner radius of the coil core of 250 mm minus the winding body to keep the coil wire in shape. For an example, the next smaller CF flange size of DN350 would result in a flange

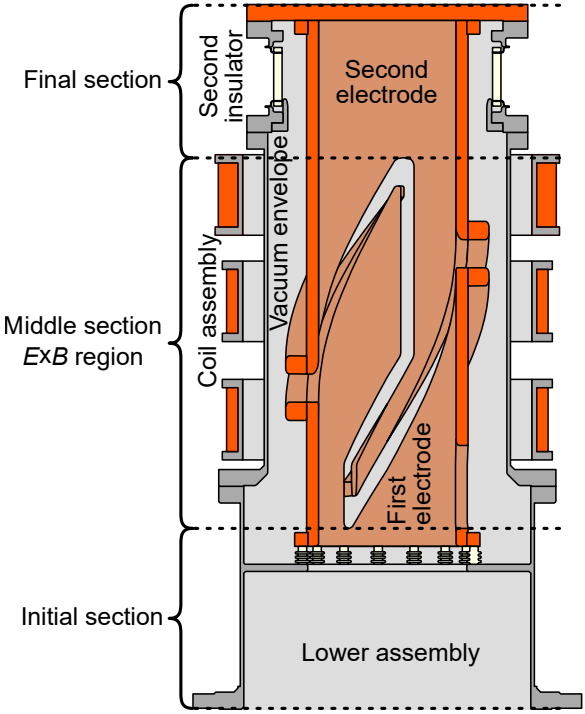

Figure 3.15: Schematic representation of the Short-Pulse MDC prototype (deviated from [105]).

diameter of 419.1 mm, an inner pipe diameter of 350 mm, an estimated outer electrode radius of 145 mm and an estimated inner electrode radius of 90 mm. The estimated beam radius would be at 77 mm if the same relative distance to the collector electrodes is considered. According to equation 1.16 this would result in an increase of the magnetic field in the $\vec{E}\times\vec{B}$ drift region by roughly 60 %, which could be simply achieved for the KIT 2 MW 170 GHz coaxial-cavity gyrotron in the 10 T magnet with a reduced axial position of the $\vec{E}\times\vec{B}$ drift region. However, adaption of the MDC to a different gyrotron with a faster diverging magnet profile would be significantly complicated with higher demands on the additional collector coils, while the outer dimensions of the vacuum housing would only be reduced by 11 %.

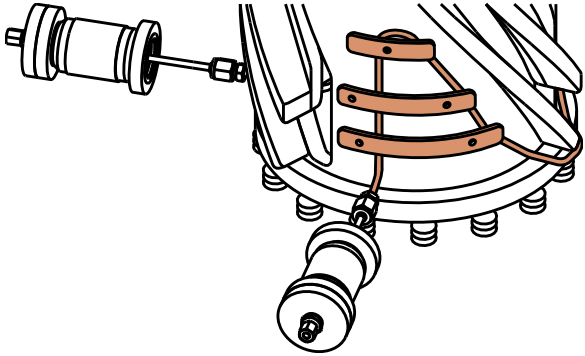

Figure 3.16: Schematic representation of the cooling system for the first electrode [105].

A scale accurate schematic representation of the final design for the SP MDC prototype is shown in Fig. 3.15. The key factors of the modular vacuum housing are the top plate to close the collector from above, the modular insulator with CF DN400 flanges on top and bottom, the middle section of the vacuum housing with a CF DN500 flange on the bottom for increased space in radial direction for assembly of the collector and the lower assembly with the sealing surface to the gyrotron mirror-box.

The lower assembly is located in the initial section and mainly responsible for the axial position of the $\vec{E}\times\vec{B}$ drift region. Since the height adjustment and mechanical adaption to the gyroton is done with the lower assembly, it is the only component of the modular MDC that is needed to be replaced when the collector is mounted on different gyrotrons. A second version of the lower assembly is produced for adaption to the 140 GHz 1.5 MW W7-X Upgrade SP gyrotron which is reduced in the axial size dimension from 370 mm to 170 mm and is equipped with a smaller flange to the mirror-box. The first electrode is mounted on top of small standard insulators that are mounted on an intermediate floor of the lower assembly, while the bottom section of the helical gap is defined as the transition from the initial section to the middle section or in other words the $\vec{E}\times\vec{B}$ drift region of the collector. Another task for the lower assembly are the high-voltage and cooling feedthroughs for the first electrode.

The cooling system for the first electrode is schematically shown in Fig. 3.16 and consists of a single pipe pressed on the outer cylindrical wall of the electrode

at three major positions with one shown in the figure. The only purpose of the cooling system is to establish a thermal contact from the first electrode to the outside for dissipation of the heat between gyrotron pulses. The performance of the cooling system is not prioritized in the mechanical design and is kept as simple as possible. The two most important simplifications of the cooling system are the implementation of standard ceramics and stainless steel as material for the pipe due to the easier and more robust welded connection.

The middle section of the vacuum housing is a closed cylindrical structure from the inside, while support brackets are welded on the outside for mechanical support of the three additional collector coils. The three coils are fixed to each other to form a single assembly and are mounted in one part to the collector. In addition to ensuring vacuum tightness and supporting the coil assembly, the middle section is also responsible for mechanical support of the parts above, including the modular ceramic and the second electrode. The modular ceramic is custom-made and symmetric for top and bottom. Mounting positions are place internally at the flanges for anti-corona-rings for reduction of the electric field at the brazed metal sheets connected to the ceramic. Based on the current implementation of the modular insulator, a single anti-corona-ring at the lower metal sheet is sufficient as the upper one is at the same potential as the second electrode. The second electrode is internally mounted on the vacuum sealing top plate and hanging through the large cylindrical ceramic from the top for electrical insulation to the vacuum housing. The insulator and the cylindrical top section of the second electrode above the helical gap are part of the final section of the MDC.

The two electrodes are constructed out of a single thick walled pipe with flanges at the top and bottom for the mechanical connection to the vacuum housing. The helical gap between the electrodes is extended in radial direction with additional helical extensions that are screwed on the side of the thick walled pipe. The height of the helical gap is adjustable to smaller values with spacers below the first electrode. An advantage of the modular construction with the electrodes completely enclosed inside the vacuum housing, is the possibility to exchange those parts for different geometries for future experimental campaigns.

Figure 3.17: 3D printed model of the prototype for verification of assembly.

3D Printed Test Assembly

A 3D printed mockup of the mechanical MDC prototype design is fabricated to visualize the assembly process of the final prototype. The model is scaled down by a factor of 2 to fit all components into a printing volume of 300 mm $\times$ 300 mm $\times$ 400 mm and to save time in the printing process. The cylindrical sections of the lower assembly, the middle assembly and the top plate are ordered in acrylic glass for visibility of the electrodes in the assembled configuration. All remaining parts (except the feedthroughs) are 3D printed and screwed in place with size accurate bolts. The finished 3D printed mockup

is shown in Fig. 3.17. No challenges appeared during the test assembly and the fabrication of the final prototype proceeded as foreseen in the mechanical design.

3.2.2 Fabrication of Individual Parts

The content of this section has already been published in Ref. [94].

In this subsection, the fabrication of the individual collector parts is presented divided in the fabrication of the inner electrodes, the vacuum housing and the external magnet coils.

Fabrication of the Inner Electrodes

The two electrodes of the MDC are the most important components in the design as their inner surfaces are the only ones represented by the theoretical design which is used for the simulation of electron separation. Other surfaces in the collector are flexible and do not affect the separation of the spent electron beam. CuCr1Zr is used for the electrodes due to the higher mechanical strength in comparison to pure copper. The raw CuCr1Zr of the pre-cut tube for the electrodes, rings for top and bottom of the electrodes and the top plate which connects the second stage with the modular ceramic are shown in Fig. 3.18a.

In the first step, the rings were fully machined, heated and put on the pre-machined tube with an interference fit. The rings are additionally secured by screws to the cylinder of the electrodes.

In the second step, a dedicated tool is attached to the top, bottom and inside of the flanged tube for mounting to a CNC machine and stabilization. Then the screw holes for the helical extensions and cooling pipes are machined, followed by the gap, separating the first and second electrode. A few bridges in the gap were kept in place until the end of the machining and were removed with hand tools after the complete gap was cut. The machined flanged tube with machined separation gap is shown in Fig. 3.18b.

In the third step, after the electrodes were separated, the surface in the gap at the positions of the bridges was smoothed out with hand tools. The inner edge

(a) Raw CuCr1Zr

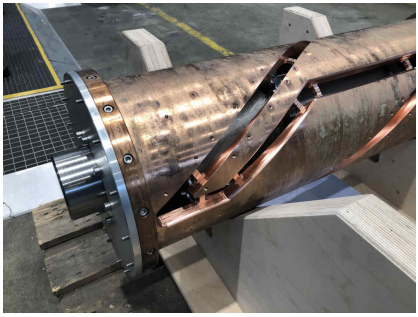

(b) Machined pipe

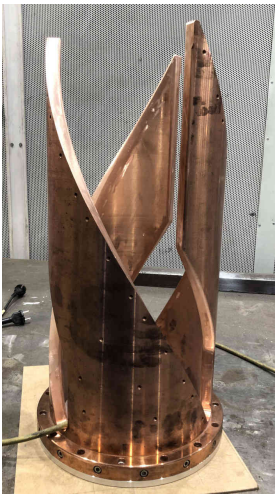

(c) First electrode

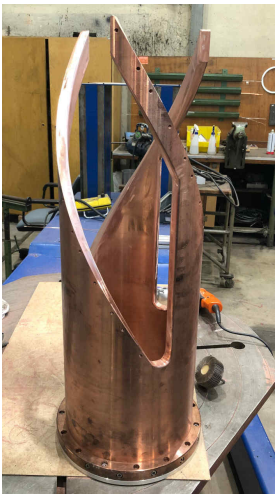

(d) Second electrode

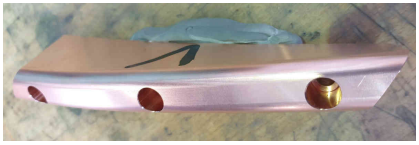

(e) Helical extension

Figure 3.18: Raw CuCr1Zr pipe and flanges for the electrodes (a), machined pipe (b), finished machined electrodes for the first electrode (c), second electrode (d) and one helical extension (e).

of the gap after machining was a sharp 90° edge, as a radius at this position would have required huge effort in programming of the CNC machine and would not have been possible at the positions of the bridges. Fortunately, the separation of the spent electron beam is not sensitive to a specific roundness of the inner edge. However, it is important to reduce the maximum electric field in order to avoid arcing in between the electrodes. The softening of the inner edge was done with hand tools. The finished machined electrodes of the first and second stage are shown in Fig. 3.18c and Fig. 3.18d, respectively.

In the fourth step, the modules for extension of the helical surface are pre-cut out of a solid CuCr1Zr block. The pre-cut module is then machined at the surface which mounts to the cylinder of the electrodes together with the holes for mounting. It is then mounted on a dedicated tool to machine the remaining surfaces on a 5-axis CNC machine. The finished module is shown in Fig. 3.18e. The MDC SP prototype is a triple helix design with two stages, giving in total six helices. These six helices are divided for the extensions into five modules each, for a total of 30 identical modules. The modules at top and bottom of a helix are afterwards cut and machined to fit the shape of the cylindrical electrode.

Fabrication of the Vacuum Housing

The vacuum housing of the MDC SP prototype consists of four parts:

- The **lower assembly** which is mounted on top of the mirror-box and supports the first stage of the collector. All cooling and voltage feedthroughs for the first stage are also located in this assembly.
- The **middle assembly**, which is mounted on top of the lower assembly and on which the external coils are mounted.
- The **modular ceramic**, which is mounted on top of the middle assembly to provide electrical isolation between the gyrotron mirror-box and the second collector stage.
- The **top plate**, which is mounted on top of the modular ceramic and connected to the cylindrical part of the second stage.

(a) Material for vacuum housing

(b) Machined vacuum housing

(c) Lower assembly W7-X

Figure 3.19: Pre-machined stainless steel material for lower and middle assembly, machined lower assembly for KIT 2 MW 170 GHz coaxial-cavity gyrotron(foreground) middle assembly (background) and lower assembly for W7-X gyrotron.

(a) Coil **(b)** Cooling jacket

Figure 3.20: One of three external coils and cooling jacket for increased operation time.

The lower assembly described here is the version for the KIT 2 MW 170 GHz coaxial-cavity gyrotronfor demonstration of the more complicated fabrication process. The lower assembly for the W7-X upgrade SP gyrotron is much smaller and milled out of a solid block of stainless steel. Majority of the material for the lower and middle assembly are shown in Fig. 3.19a. Both cylindrical parts are produced by rolled and welded sheets of stainless steel, which is machined on a lathe to achieve the desired accuracy.

In the first step, the pre-machined flanges are welded on the ends of both cylinders. In the second step, the sealing edges and screw holes of the flanges are machined to ensure correct planar alignment between top and bottom of the cylinder. In the third step, additional feedthroughs, mounting blocks and the finished machined intermediate floor of the lower assembly are welded in place. Both versions of the finalized lower assemblies and the finalized middle assembly are shown in Fig. 3.19b and Fig. 3.19c.

Fabrication of the Coil Assembly

Three additional external magnet coils are required for the MDC SP prototype to modify the spent electron beam inside the $\vec{E}\times\vec{B}$ drift region to a constant beam radius. The coils will be operated with a constant current, hence no eddy currents are induced in the winding body of the coil during operation. A non-slotted aluminum winding body is chosen for all coils. On the outer side of the winding body are screw holes to mount brackets for fixation of the coils to each other and to the middle assembly as well as lifting brackets for easier handling during assembly. The electrical connection of the coils is realized with commercially available ceramic clamps on the side of the coils. Winding

of the coils was done on a dedicated winding machine for a dense packaging of the rectangular copper wire. A summary of the coil winding processes with the correct number of turns per layer is given in Tab. 3.4. The maximum operation temperature of the coils is at 200 °C, due to the insulation coating on the individual wires. Additional cooling jackets have been produced to increase the operation time of the coils. A finished coil is shown in Fig. 3.20a and a cooling jacket is shown in Fig. 3.20b.

3.2.3 Assembly of the MDC SP Prototype

The content of this section has already been published in Ref. [94].

Two different assemblies of the MDC SP prototype have been done until end of 2023 and are presented in the next two sections. The first assembly of the vacuum housing is in a configuration for the KIT 2 MW 170 GHz coaxial-cavity gyrotron, while the second assembly of the complete collector is in a configuration for the W7-X upgrade SP gyrotron.

Assembly of the Vacuum Housing in 2 MW Coaxial-Cavity Gyrotron Configuration

The first assembly was done after all components for the vacuum housing and the external coils were fabricated. This includes a cover flange for the bottom to seal the collector and pump vacuum without a gyrotron attached to

Table 3.4: Number of turns per layer and total number of turns for each coil.

Layer	**1**	**2**	**3**	**4**	**5**	**6**	**7**	**8**	**total**
Coil A	28.25	28.25	28.31	28.31	28.50	28.00	28.04	28.00	→
Coil B	28.25	28.00	28.19	28.19	28.00	28.19	28.00	28.50	225.33
Coil C	28.75	27.50	28.75	28.50	28.50	28.75	28.75	28.25	227.75
Layer		→	**9**	**10**	**11**	**12**	**13**	**14**	**total**
Coil A		→	28.00	28.00	28.00	28.00	28.00	29.00	394.65

(a) (b) (c)

Figure 3.21: Assembly of the vacuum housing in 2 MW coaxial-cavity gyrotron configuration.

it, the lower assembly for the KIT 2 MW 170 GHz coaxial-cavity gyrotron, the middle assembly, the modular ceramic, the top plate and the coils. The electrodes and the lower assembly for the W7-X upgrade SP gyrotron were not finished at this stage and therefore not included in the first assembly. No internal components were mounted in the housing, significantly simplifying the process. The individual components were installed from bottom to top, starting with cover flanges to the bottom and feedthrough flanges of the lower assembly. Next, the middle assembly was mounted on the lower assembly as shown in Fig. 3.21a, followed by the modular ceramic and the top plate to close the vacuum housing as shown in Fig. 3.21b. The assembly of the external parts started with mounting the lifting brackets to the coils and combining them with the mounting brackets to a single assembly. The coil assembly was then lifted over the vacuum housing and lowered to the support mounts on the middle assembly. In the final step, the transport protection was put on the ceramic and the lifting brackets for the complete collector were mounted on the bottom flange of the modular ceramic. It is important to note that the lifting of the collector is only supported by these lifting brackets and not from any point above the ceramic to avoid damage to the ceramic. The process of assembly of the vacuum housing and external parts proceeded as planed without

interruptions due to incorrectly produced parts. The partly assembled collector achieved an excellent vacuum leaking rate of between $1.0{\times}10^{-12}$ mbar L s^{-1} to $1.0{\times}10^{-10}$ mbar L s^{-1} at a pressure of $1.1{\times}10^{-7}$ mbar after pumping, which was limited by the Fluorine rubber (german: Fluorine Kautschuk Material) (FKM) seal to the bottom plate. The closed vacuum housing is shown in Fig. 3.21c.

Assembly of the Complete MDC in W7-X Upgrade SP Gyrotron Configuration

The second assembly of the MDC SP prototype was done after all parts were fabricated. This time the second version of the lower assembly was used to make the collector compatible with the W7-X upgrade SP gyrotron at KIT. It is currently planned to make the world's first MDC experiments with a fusion relevant gyrotron with this tube due to the availability of equipment. The MDC can only be operated with the modular power supply from AMPEGON in the new FULGOR test stand at KIT. Experiments at the old KIT gyrotron test stand are currently not possible, as no high voltage connection between both test stand exist. The FULGOR test stand is designed with cryogen free magnets in mind, limiting the available experimental equipment further. The next available cryogen free magnet at the FULGOR test stand is a 4.2 T SC magnet from Commissariat à l'énergie atomique et aux énergies alternatives (CEA) Tungsten (chemical symbol "W") Environment in Steady-state Tokamak (WEST) and it is possible to operate the W7-X upgrade SP gyrotron in this magnet at 105 GHz.

The second assembly started with the lower assembly and the ceramic insulators of the first stage which are screwed onto the intermediate floor. Then the cylindrical part of the first electrode is lowered on the insulators and fixed with screws. In the next step, the cooling pipe is mounted on the outside of the first electrode and the mount for the high voltage connection is mounted on the bottom flange of the electrode. Snapshots of the assembly progress are shown in Fig. 3.22a and Fig. 3.22b. Finally, the feedthroughs, as shown in Fig. 3.22c, and helical extensions are mounted to the first electrode, finalizing this part of the MDC. The completed first electrode is shown in Fig. 3.22d.

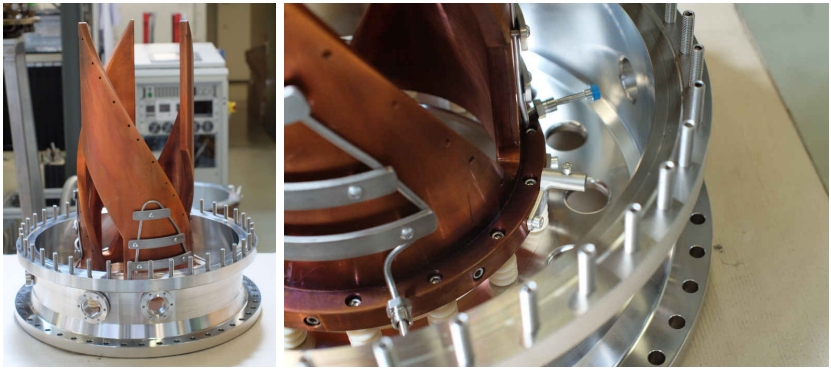

(a) (b)

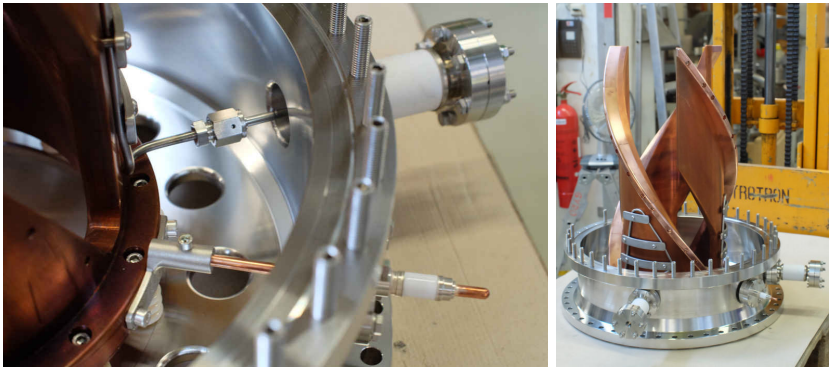

(c) (d)

Figure 3.22: Assembly of the first electrode in W7-X upgrade configuration.

Assembly of the second electrode started with mounting the top plate to the cylindrical part of the second electrode, as shown in Fig. 3.23a. In the next step, the anti-corona ring was mounted inside at the lower flange of the modular ceramic to avoid increased electric field at the welded metal which connects the ceramic to the metal flanges. Then the cylindrical part of the second electrode was lowered through the modular ceramic and the top flanges were bolted together. In the final step of assembly of the second electrode, the helical extensions are mounted on the outside of the cylinder. The final step was performed in this order to allow a smaller ceramic to be made to provide

(a) (b)

Figure 3.23: Assembly of the second electrode.

potential isolation for the second collector stage. The finished assembly of the second electrode is shown in Fig. 3.23b.

The final step in assembly of the MDC electrodes is the combination of both electrode assemblies as shown in Fig. 3.22d and Fig. 3.23b with the middle assembly of the vacuum housing. To demonstrate the fit of both electrodes and to train for the final and most complicated assembly step, an assembly test without the vacuum housing was performed. Note that due to the extension of the helical gap in axial direction, the second electrode must be rotated as it is lowered to avoid collision with the first electrode and potential damage. A view of the MDC electrodes without the vacuum housing is shown in Fig. 3.24. The assembly test and the process of simultaneous lowering and rotation of the second electrode was successfully practised.

The easiest approach to continue with the last step in the assembly process is to mount the middle assembly on the lower flange of the modular ceramic and lower the part onto the assembly with the first electrode. The process of rotation as the upper part of the MDC is lowered to the lower part is documented in a

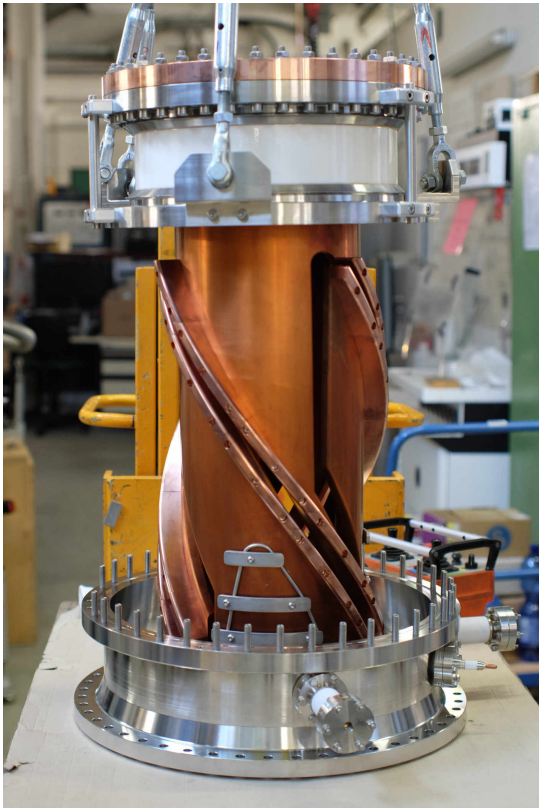

Figure 3.24: Assembly demonstration of both electrodes without vacuum housing.

few time steps in Fig. 3.25a, Fig. 3.25b and Fig. 3.25c. The assembly process was considered during the mechanical design of the MDC SP prototype and the middle assembly of the vacuum housing was deliberately made shorter than the second electrode to allow it to be viewed from the side when lowered. The lower tip of the second electrode is best visible in Fig. 3.25a for two different azimuthal positions. A view from the bottom of the assembled MDC SP prototype is shown in Fig. 3.25d. The collector bottom was closed with a flange at the bottom to pump vacuum and keep the internal parts of the collector clean while waiting for the experimental equipment to become available.

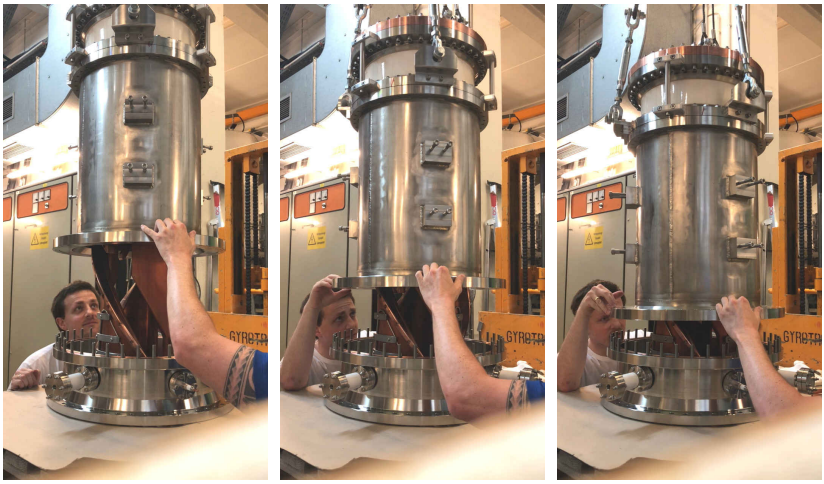

(a) **(b)** **(c)**

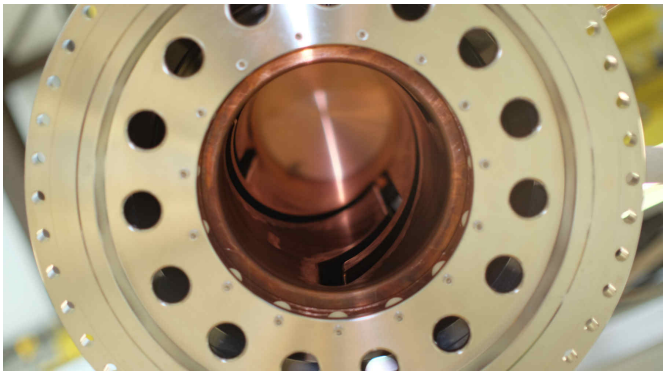

(d) Bottom view

Figure 3.25: Closing of the vacuum housing with electrodes (a), (b) and (c). Few from the bottom of the assembled MDC prototype (d).

3.3 Summary

The development of the first SP MDC prototype for high-power gyrotrons represents a significant advancement in the field of high-power microwave devices, with the potential to enhance efficiency and performance. In this chapter, a comprehensive overview of the design, optimization, manufacturing and assembly processes is provided, emphasizing on the importance of simplifying the prototype while maintaining its functionality and effectiveness. The magnetic setup is defined at the start of the electromagnetic design for the foundation of the further optimization of the prototype. The utilization of only three normal conducting coils is achieved to modify the magnetic field of the superconducting magnet. Homogeneous cylindrical multi-turn coils are used in the design to maintain a consistent magnetic field. The optimization of these coils ensures a constant beam radius in the $\vec{E}\times\vec{B}$ drift region for stable and efficient MDC operation with the straight cylindrical design concept.

After the empirical optimization of the electromagnetic triple helix design, the tolerances are studied well beyond the manufacturing accuracy for a validation of the design and for ensuring the MDC operation despite potential imperfections of millimeters up to centimeters. A systematic investigation of various geometrical parameters is carried out, including the height of the $\vec{E}\times\vec{B}$ drift region, the inner electrode radius, the helical gap height, the bottom straight cut height, the azimuthal overlap angle, and the distance between both electrodes. For all parameters, the correct compromise is chosen to limit the reflected current to a low value of around 50 mA, while achieving a high collector efficiency of 78.8 %. This result ensured that the prototype can be operated within safe and efficient parameters, while accounting for manufacturing tolerances and potential misalignment. The design goal of a robust electromagnetic MDC design which is simple and small is achieved.

Although thermal management is not a primary concern for SP gyrotron components, it is addressed to ensure that the MDC prototype remains within safe operating temperatures. The analysis of the power loading density on the inner collector wall surface demonstrated that it is within the acceptable limit for short-pulse operation. The maximum power loading densities of 6 kW/cm^2 and 4 kW/cm^2 for the first and second stages, respectively, in combination with the shape of the profile, indicate that the design is well optimized. A thermal analysis is also performed for the additional collector coils to guide future

experimental campaigns and to safely reduce the coil dimensions without risk of damage due to overheating.

The SP MDC prototype is designed to be modular with flexibility in mind, allowing it to operate with different gyrotrons and frequency points. This adaptability is of importance for the purpose of experimental verification and future developments. The design's capacity to operate in varying magnetic field profiles and depression potentials without a significant decline in performance demonstrates its robustness. A detailed analysis of voltage operation points serves to enhance this flexibility, thereby providing a clear roadmap for the optimization of the prototype under different operational scenarios and towards experimental validation of the SP MDC prototype. The operation scenarios include 4 different magnets and 2 gyrotrons operated at frequencies of 105 GHz, 136 GHz, 140 GHz, 170 GHz (in first and second harmonic), and 204 GHz.

The modular mechanical design is presented with details on the component choices and dimensions. A cooling system for the first electrode is designed and included in the setup to achieve a thermal contact to the outside of the vacuum housing. The assembly feasibility is checked with a 3-D printed mock-up and successfully completed and followed by the fabrication of individual collector parts. After realization of all prototype components, the assembly of the MDC is successfully accomplished in two configurations, one for the KIT 2 MW 170 GHz coaxial-cavity gyrotron and one for the W7-X upgrade SP gyrotron.

4 Toward Operation at Continuous Waves

The validation of the SP MDC is the first step towards Introduction of the $\vec{E}\times\vec{B}$ drift principle in a high-power gyrotron to increase the efficiency of the complete tube. However, in SP operation with a few milliseconds, the increased efficiency is not that significant. In CW operation with a large number of gyrotrons, each small increment in the efficiency will save a lot of power. As an example, if the efficiency of a 2 MW tube is increased from the current 50 % with an SDC to over 60 % with an MDC, the power consumption during operation is reduced by almost 700 kW. In future ECRH plants, not only one but many tens to one hundred gyrotrons will be installed, yielding potential power savings in the high tens of megawatts. In addition, less heat is generated in an individual tube, reducing the size of the electrodes and the demand on the cooling system.

The following content of this chapter has already been published in Ref. [91], whereas the outlook for a mechanical CW MDC design in section 4.4 and the sensitivity to SMF in section 4.5 are added.

4.1 Up-scaled Short-Pulse Prototype Geometry

The most characteristic changes between a SP SDC and a CW SDC [39] is a larger size in radial and axial direction for a reduced overall power loading density as well as the implementation of a sweeping system for a reduced time averaged power loading density [38]. The main limitation of gyrotron collectors for LP or CW operation are the cooling capabilities. Up to now, one of the most sophisticated and established cooling techniques for large objects like a high-power gyrotron collector is the HV cooling which is already presented in section 1.4.2. The collector size is significantly increased with

the gyrotron output power, making it the largest component in a high-power gyrotron.

The same principle of an increased size of the collector stages is applied for the CW compatible MDC design approach [106]. The inner radius of the collector stages is increased from 115 mm of the SP MDC to 150 mm and the electron beam radius in the collector is raised from 98 mm to 127 mm. The initial axial position of the $\vec{E}\times\vec{B}$ drift region is moved to a higher axial position due to the increased beam radius and the identical magnetic field profile of the gyrotron magnet. The stages of an MDC system can be significantly reduced in size in comparison to a conventional SDC due to the reduced absolute power loading at the collector surface. A size comparison between the 2 MW CW SDC and CW MDC is shown in Fig. 4.1 including some of the key dimensions. The preliminary MDC design as shown here is an up–scaled version of the SP MDC. The design of the cooling system is not implemented at this state however, it is important to note that both cooling circuits must be set up independently of each other to avoid insulators of the cooling pipes inside the vacuum. It is planned to implement a HV cooling for the cylindrical top section of the second stage and water–cooling channels under the helical surface of the first stage.

Additional collector coils are required for the homogenization of the magnetic field in the $\vec{E}\times\vec{B}$ drift region of the MDC system to achieve a constant electron beam radius. A summarized constant coil current of 37.8 kA·t is applied for the first conceptual design of a CW MDC. In addition, a summarized alternating current with a peak value of 10.5 kA·t is applied to the two upper coils for the magnetic field sweeping. The summarized alternating peak current of the six sweeping coils of the CW SDC is 10.8 kA·t. The axial length of the sweeping area is close to 500 mm for both collector designs.

4.2 Methods for Electron Beam Sweeping

The increased size in radial dimension is not sufficient for an acceptable power loading density at the first stage. A further decrease of the power loading density on the helical surface is possible by either a decreased absolute power on the first stage, or a sweeping system for the first stage. A combination of both approaches is also possible.

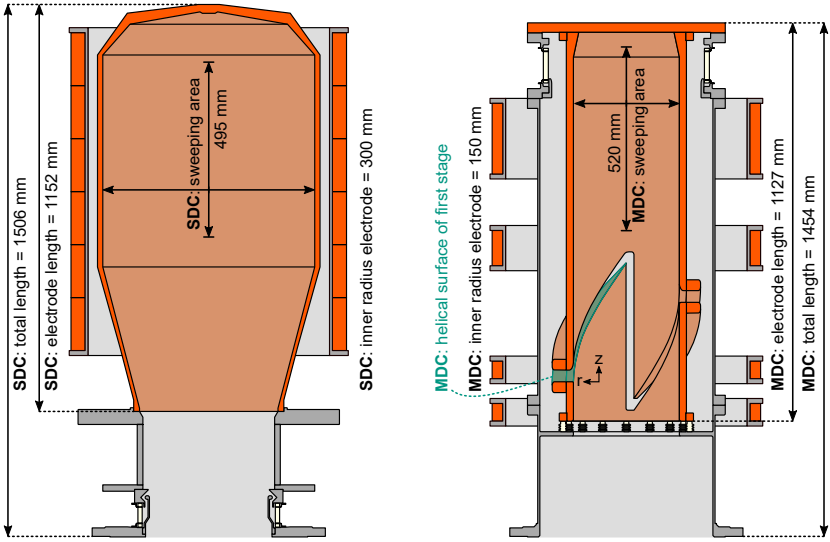

Figure 4.1: Size comparison between the CW SDC and the CW MDC. The fast spent electrons in the MDC are collected at the upper cylindrical section of the second stage. The slow spent electrons are collected at the three helical surfaces of the first stage (one marked in green) (deviated from [91]).

The only possibility for a sweeping system on the first stage is a variation of the radial position of the spent beam electrons on the helical surface. The final radial position is the sum of the beam radius in the collector plus the drift distance D_d, when no beam thickness is considered. A variation of the beam radius is not planned, due to the increased sensitivity to stray magnetic fields for a beam radius closer to the collector stage and a higher reflected current for a beam radius further away from the collector stage. A variation of the drift distance D_d is therefore the preferred option for a sweeping system on the first stage. The drift distance D_d is defined as:

$$D_\mathrm{d} = \frac{2\, m_\mathrm{e}\, v_0}{e\, B_\mathrm{z}} \tan\vartheta \tag{4.1}$$

for the simplified case of a planar electron drift [18]. The mass of the electron m_e, the (positive) charge of the electron e and the magnetic field parallel to the axis B_z are constant. The angle ϑ between the electric and magnetic field in the

collector is dependent on the geometry of the MDC and is therefore constant for a realistic system without moving parts. The velocity v_0 of the spent electrons at the moment when they reach the $\vec{E}\times\vec{B}$ drift region is the only variable which can be swept. It can be increased reducing the deceleration potential at the collector entrance, or vice versa; while the potential of the second stage should not be changed to keep a high collector efficiency.

A variation of the absolute power collected at the first stage is the most critical factor when the collector potentials are varied in an MDC. The theoretical power fraction of the spent electron beam collected at the first stage without a reflected current versus the depression potentials as function of the applied potentials of the two collector stages is shown in Fig. 4.2. The voltage operation points with constant potential difference ΔU between both stages are represented by straight lines. The radial position at which the spent electron beam is collected at the first stage is directly related to the potential difference, as it is proportional to the electron drift. A strong change of the potential difference is required to sweep the electron beam. The absolute power loading on the first stage is reduced compared to the SP MDC. Four different operation points are chosen along the line of 40 kW of power on the first stage to present the idea of an $\vec{E}\times\vec{B}$ sweeping system. The highest depression potential on the first stage is limited to 35 kV as applied in the conventional SDC to avoid reflections at the collector entrance. The simulation results of the different operation points are summarized in Tab. 4.1. It should be mentioned that the absolute power loading on the first stage is in all cases higher than the theoretical value due to the collection of some electrons with higher initial kinetic energies. The absolute power loading on the second stage is only slightly influenced and is in a non-critical range. The collector efficiency is varied over time due to the change in the voltage operation point.

The power loadings on the first stage for different operation points are shown in Fig. 4.3. The power loadings are pushed to a larger radial position with increased potential difference between both stages due to the increased $\vec{E}\times\vec{B}$ drift. The reason for the increased reflected current for a potential difference of 12 kV is clearly visible by the close proximity of the power loading to the inner edge of the helical surface. The higher reflected current could be prevented by a higher minimal potential difference or a steeper helical cut between both stages. The power loadings on the second stage are varied in axial direction for different operation points and are shown in Fig. 4.4. The power loading at the

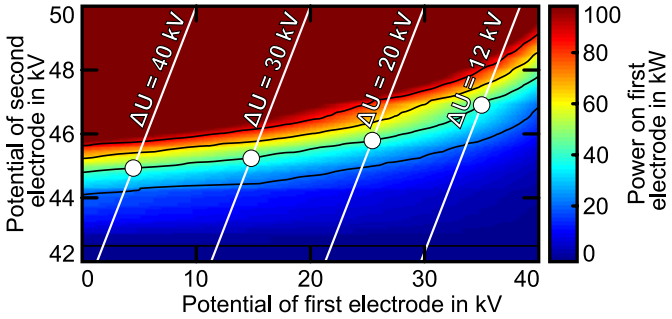

Figure 4.2: Theoretical power loading on the first stage versus depression potentials of both collector stages [91].

azimuthal location of the helical cut is pushed to a lower axial position with increased potential difference and to a higher axial position at the azimuthal location of the straight cut. The power loading at the intermediate locations is not significantly influenced by the $\vec{E}\times\vec{B}$ sweeping. The power loadings of the first and second stage with identical voltage operation points are calculated together in the same simulation.

The time averaged power loadings on the first and second stage are shown in the top of Fig. 4.5 and Fig. 4.6, respectively. The power loading is distributed

Table 4.1: Simulation results for different operation points. The total gyrotron efficiency is calculated under the consideration of 35 % interaction efficiency and 10 % losses in the electromagnetic wave.

ΔU	40 kV	30 kV	20 kV	12 kV
Potential first stage	−4.8 kV	−15.2 kV	−25.7 kV	−35 kV
Potential second stage	−44.8 kV	−45.2 kV	−45.7 kV	−46.8 kV
Power loading first stage	67 kW	44 kW	46 kW	46 kW
Reflected current	68 mA	107 mA	231 mA	518 mA
Collector efficiency	78.2 %	79.4 %	80.0 %	81.6 %
Total gyrotron efficiency	64.1 %	65.1 %	65.6 %	67.1 %

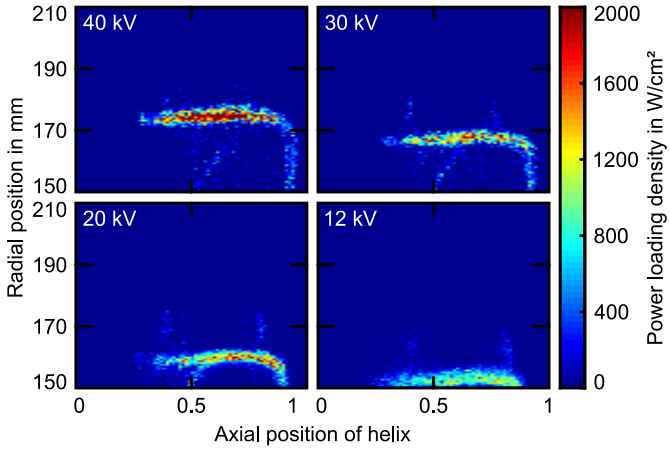

Figure 4.3: Power loading density on the first stage of the CW MDC with $\vec{E}\times\vec{B}$ sweeping for different operation points. The helical surfaces are projected to a 2D plane with their radial an axial position [91].

effectively on the helical surface and significantly improved on most of the cylindrical surface of the second stage.

Traditional magnetic field sweeping systems are limited in the sweeping frequency due to high eddy currents which are induced in the collector wall. The $\vec{E}\times\vec{B}$ sweeping is not limited to such low sweeping frequencies, as it is not based on alternating magnetic fields. The cyclic fatigue in the collector could be decreased by a higher sweeping frequency which could significantly improve the maximum acceptable power loading density. However, those expectations are exceeded in this design with the maximum power loading density of up to 3 kW/cm^2 at some points of the second stage in case of a pure $\vec{E}\times\vec{B}$ sweeping.

Another possibility for the operation of a CW MDC is a fixed voltage operation point with a small absolute power loading on the first stage and an axial magnetic field sweeping system for the second stage. Depression potentials of -25 kV for the first stage and -44 kV for the second stage are chosen. A collector efficiency of 78.1 %, a total gyrotron efficiency of 64.0 %, a reflected current below 65 mA and a power loading of 11 kW on the first stage are achieved in simulation, independent of the phase of the sweeping cycle. The trajectory simulations are performed in steady state for different time steps

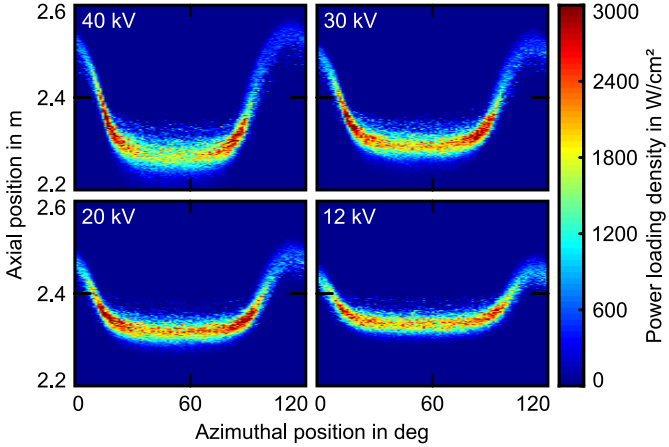

Figure 4.4: Power loading density on the second stage of the CW MDC with $\vec{E}\times\vec{B}$ sweeping for different operation points [91].

and combined in post–processing. Eddy currents are not considered in the system and an advanced sweeping function is chosen. The time averaged power loadings on the first and second stage are shown in the bottom of Fig. 4.5 and Fig. 4.6, respectively. The thermal loading on the helical surface of the first stage is not influenced by the magnetic field sweeping system of the second stage. The goal of a maximum power loading density of under 500 W/cm^2 without secondary electron emission is achieved for this design. The following parts of this chapter will be concentrated on the CW MDC with only magnetic field sweeping due to the acceptable loading densities on both stages and the lower demands on the gyrotron power supply compared to the CW MDC with $\vec{E}\times\vec{B}$ sweeping system.

The instantaneous maximum power loading density of the CW SDC and CW MDC with magnetic field sweeping is at 3.7 kW/cm^2 at the lower turning point of the sweep cycle [107]. The high instantaneous power loading density in the MDC is limited to in total six small areas at the azimuthal position of the transition between the straight and helical cut. It is reduced to less than 3.0 kW/cm^2 at the azimuthal position of the helical cut and to less than 1.3 kW/cm^2 at the azimuthal position of the straight cut. The power loading density in the CW SDC is independent on the azimuthal position. The maximum power loading density in the MDC is varied in azimuthal direction due to different beam

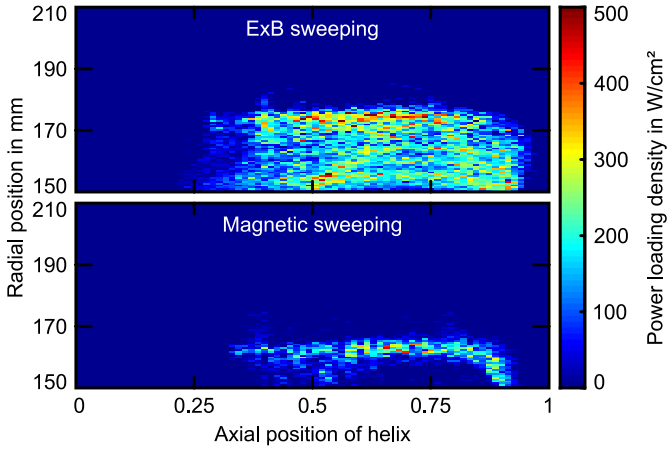

Figure 4.5: Time averaged power loading density on the first stage of the CW MDC with $\vec{E}\times\vec{B}$ sweeping (top) and magnetic field sweeping (bottom). The helical surfaces are projected to a 2D plane with their radial an axial position [91].

thickness caused by the $\vec{E}\times\vec{B}$ drift and variations in the angular line density. The line density of the thermal loading in azimuthal direction is in direct correlation to the absolute power that is absorbed in an angular segment of the cylindrical collector wall and is shown in Fig. 4.7. The azimuthal variation of the thermal loading is created by an azimuthal electron drift due to radial electric field components E_r near the edges of the cut between the collector stages. The azimuthal electron drift is strongest in the area of the straight cut (between 100° to 120° for the CW MDC) and is most noticeable due to a drift direction away from the cut and therefore a reduced thermal loading at this position. The angular line-density for an SDC is constant due to the symmetry condition and is independent on the collector geometry. The average angular line density is correlated with the efficiency of the collector and is different for all three collector systems.

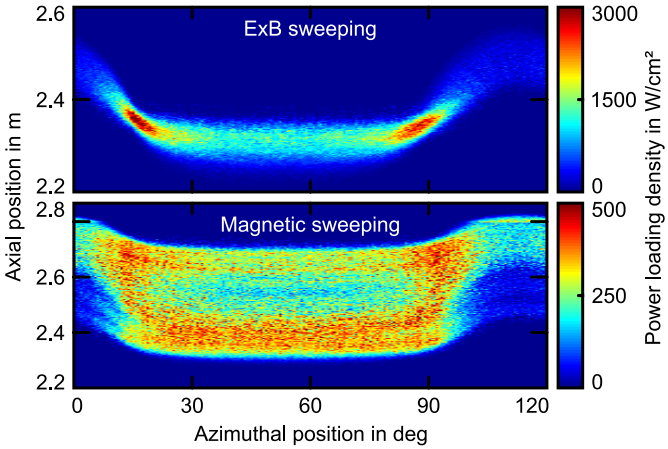

Figure 4.6: Time averaged power loading density on the second stage of the CW MDC for the $\vec{E}\times\vec{B}$ sweeping (top) and magnetic field sweeping (bottom) [91].

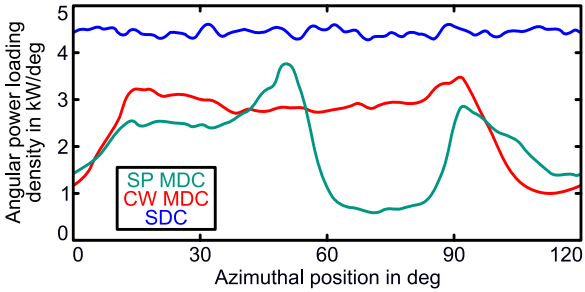

Figure 4.7: Angular power loading density for an SDC, the SP MDC and CW MDC with magnetic field sweeping [91].

4.3 Thermal Expansion for CW MDC

The thermal expansion in general is dependent on the temperature and temperature differences in a material. The temperature profile on the inner collector wall is in direct correlation to the thermal loading. In this section, the influence of the azimuthally varied thermal loading in the CW MDC to the thermal expansion of the second collector stage with a complex geometry is studied. The thermal simulations for a representation of a water cooling are performed in

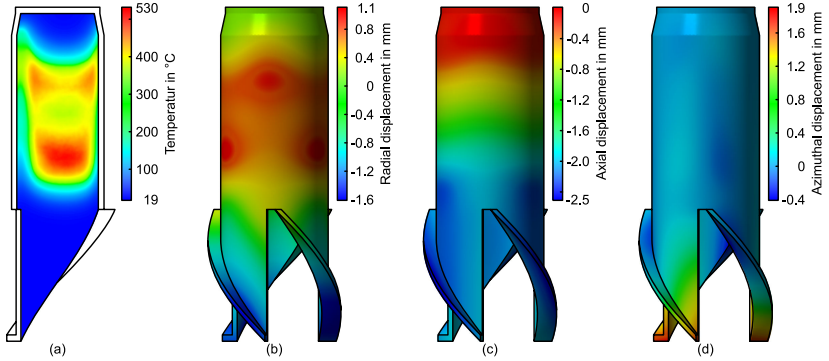

Figure 4.8: Temperature (a) and thermal expansion in radial (b), axial (c) and azimuthal (d) direction of the CW MDC [91].

Ansys with an imported power loading profile, a 3D geometry, a heat transfer coefficient of 8 kW/m^{2}K and an ambient temperature of 19 °C. The utilized heat transfer coefficient is in the range for a cooling with water–forced convection [45] and is a preliminary investigation for a worst–case scenario. The heat transfer coefficient for a HV cooling is in the range of 8.5 kW/m^{2}K to 23 kW/m^{2}K in combination with a larger surface [48]. The second collector stage is fixed at the top plate as shown in Fig. 4.1. The steady state temperature at the inner collector wall is shown in Fig. 4.8 (a) and is in correlation to the power loading as expected. The thermal expansion in radial direction is shown in Fig. 4.8 (b) and the deformation at the cylindrical top section is only slightly varied. The absolute value of deformation at the cylindrical top section should be uncritical as it is proportional to the collector size. The maximum power load density and thus the temperature and relative deformation should be identical to the validated CW SDC. However, the deformation at the lower part of the helical section is more critical, as a correct placement for a constant gap between both electrodes is required to achieve a well defined $\vec{E}\times\vec{B}$ drift. The same arguments also apply to the axial and azimuthal thermal expansion as shown in Fig. 4.8 (c) and (d), respectively.

The thermal deformation at the lower part of the second collector stage could be significantly improved by a different mounting method as the fixation at the top plate is not ideal. A mount directly above the $\vec{E}\times\vec{B}$ drift region should be more optimal since the lower part of the second collector stage is not heated. The

thermal expansion has to be considered for future more realistic mechanical designs of an $\vec{E}\times\vec{B}$ drift CW MDC.

4.4 Improved Mechanical Design with Cooling System

The thermal behavior of the CW MDC is of most importance for the process toward a mechanical design that can be built and operated. As mentioned at the end of the last section, the thermal deformation of the second collector electrode can be improved by a different mounting method. Another advantage of the mechanical support directly above the $\vec{E}\times\vec{B}$ drift region is the cooling possibility of the second electrode. The cylindrical top part can be exposed to the outside and the same HV cooling as in traditional SDCs could be utilized in the design. The improved preliminary mechanical design of the CW MDC is shown in Fig. 4.9a with the mechanical support position of the second electrode marked with a red line. Cooling of the first electrode is foreseen at the helical surface, where the slow electrons are collected. Cooling channels are integrated in each of the three helices with individual feedthroughs, two for each helix for the inlet and outlet of the cooling water. The insulator for the second stage is moved to the bottom of the collector and the first electrode is internally isolated to the second depression potential. A shield on the ceramic is added to protect the ceramic from stray radiation and to shield the electron beam from the second depression potential. From a physical point of view, the design is identical to the previous design as the internal shape of the electrodes is not changed. The power loading and temperature distribution are also identical due to the unchanged physical design.

However, the thermal deformation is significantly improved by the novel mechanical design idea, especially in the lower part of the second electrode, which is more sensitive than the cylindrical upper part. The radial displacement in the $\vec{E}\times\vec{B}$ drift region is reduced from 1.6 mm to 0.3 mm and is shown in Fig. 4.9b, while the axial displacement in the $\vec{E}\times\vec{B}$ drift region is reduced from 2.5 mm to 0.1 mm and is shown in Fig. 4.9c. The azimuthal displacement in the same area is reduced from 1.9 mm to 0.4 mm and is shown in Fig. 4.9d. In summary, it can be concluded that the thermal deformation in the $\vec{E}\times\vec{B}$ drift region has

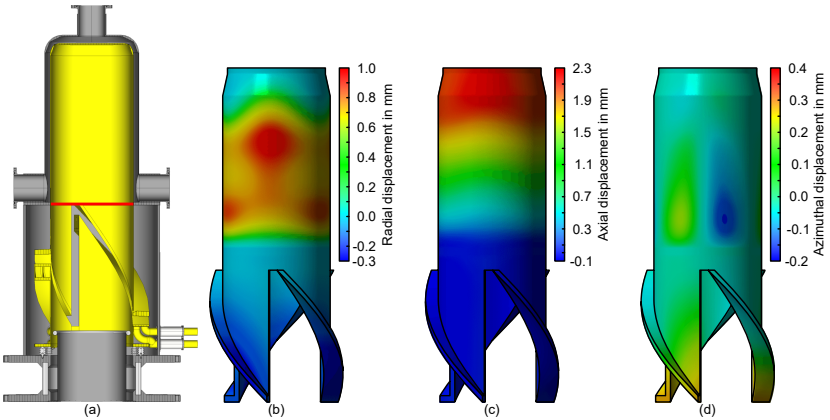

Figure 4.9: Updated preliminary mechanical design with mechanical support of the second electrode marked in red (a). Thermal expansion in radial (b), axial (c) and azimuthal (d) direction of the CW MDC.

been reduced to 21 % or less in comparison to the first draft with the improved mechanical design idea.

4.5 Stray Magnetic Field with CW MDC

The demonstration of an increased SMF sensitivity of the SP MDC prototype in section 3.1.7 in comparison to the operation of conventional SDCs in section 1.4.3 is primarily for scientific purposes, due to the usual absence of SMF sources in the proximity of SP gyrotron test-stands. For CW MDCs it will be different, since these will be installed in large ECRH installations with many gyrotrons and a tokamak in proximity. The same investigation for study of SMF influence on the collector operation is performed as in section 3.1.7 with constant radial magnetic field in the complete simulation volume to represent the SMF of a tokamak and with a single neighboring gyrotron approximated with a magnetic dipole. The simulated performance under the influence of a radial stray magnetic field is shown in Fig. 4.10. The collector efficiency is only slightly influenced with radial magnetic field and the reflected current is between 46 mA to 77 mA and therefore not included in the figure. The collector symmetry of 120° is also visible in the variation of collector efficiency and

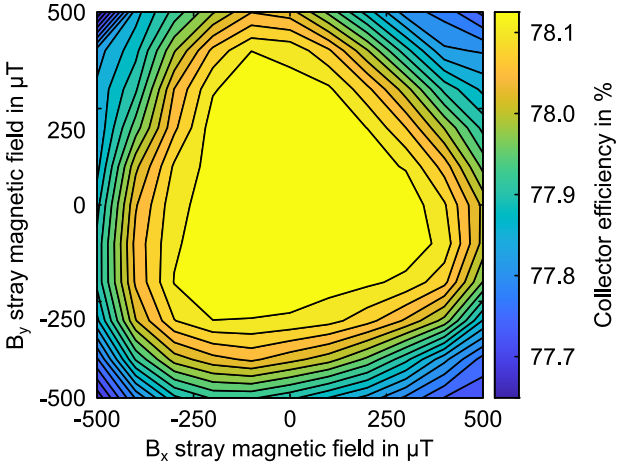

Figure 4.10: Simulated CW MDC performance under the influence of a radial stray magnetic field.

suggests that the collector has a slight azimuthal dependence for sensitivity against SMF.

The results for collector operation in proximity to neighboring gyrotrons is summarized in table 4.2 with an increased influence to SMF for a gyrotron distance of only 3 m. For distances of 4 m or larger, the influence of SMF is negligible to the collector performance. However, since the collector should be operated in CW, electrons are not allowed to hit the collector top plate. In the current design, with magnetic field sweeping at the second electrode, this is not the case for all time steps in the sweeping cycle. An increase of the upper cylindrical section could simply solve this challenge for future designs due to the fast diverging magnetic field lines in this section.

Table 4.2: Simulated CW MDC performance with the SMF of neighboring gyrotrons at different distances.

Distance	3 m	4 m	5 m
Collector efficiency	72.1 %	78.0 %	78.1 %
Reflected current	85 mA	55 mA	54 mA

4.6 Summary

The SP MDC prototype design for the KIT 2 MW 170 GHz coaxial-cavity gyrotron is presented in chapter 3 with promising results in its versatility and robustness. The main limitation in the maximum pulse length of a SP collector is a high-power loading density at the inner surface of the collector stage. The same principle is used to develop an upscaled CW compatible MDC, however, a pure increase in size is not sufficient for an acceptable maximum power loading density of 500 W/cm^2. In addition, two different sweeping concepts are presented to distribute the power loading to a larger surface and decrease the power loading density on the inner collector wall. Those include a variation of the voltage operation point to modify the electron collision point with the $\vec{E}\times\vec{B}$ drift and an LMFS as it is used in SDCs. The importance of the voltage operation point of the collector electrodes is mentioned in order to modify the power which is collected by each electrode. The power collected on the first electrode is particularly relevant due to the limited area on the helical surfaces and should not exceed an average power of 50 kW for the sweeping with the electrode potentials and 11 kW for the LMFS.

A comparison in size, sweeping system and maximum power loading density of the up-scaled CW MDC to a CW SDC of a 2 MW gyrotron is given. All three components are comparable between the SDC and MDC, despite the smaller electrode size of the MDC. The outer dimensions of both collectors have lengths of approximately 1.5 m and outer radii close to 300 mm without the coils of the sweeping system. The LMFS as used in SDCs can be implemented in an MDC to achieve an identical average power loading density of 500 W/cm^2 to apply the same kind of validated cooling system. The influence of the thermal expansion in a CW MDC is discussed, and the limitation is clarified. An updated mechanical design approach with modified mounting locations is presented and offers a significant reduction of the thermal deformation which should be considered for future design iterations. The updated mechanical design approach also simplifies the cooling of the cylindrical part of the second electrode, as it is identical to the implementation in an SDC. No principle showstoppers are found for the CW MDC in power loading density or mechanical deformation.

The sensitivity against SMF is at a high level with a compatibility of a pure radial magnetic field of up to 500 µT, or a neighboring gyrotron in 4 m distance

to operate without SMF compensation. Such values are improved even in comparison to a smaller SDC of a 1 MW gyrotron, which is limited to a pure radial magnetic field of around 200 µT and a neighboring gyrotron in 5 m distance to operate without SMF compensation [52]. The compatibility against SMF and the increased collector efficiency making the CW MDC a prime candidate for large ECRH installations in the future.

5 Enhancements in Thermal Loading and Lifetime with *E*×*B* Drift

The content of this chapter has already been published in Ref. [108].

The low sweeping frequencies of magnetic field sweeping systems as discussed in section 1.4.2 are not sufficient for a homogeneous temperature distribution at the inner collector wall due to the high instantaneous thermal power loading. Each point in the intersection region of the inner collector wall with the spent electron beam is rapidly heated when the electron beam is swept over and quickly cooled when the electron beam is at a different position. A higher sweeping frequency could significantly reduce the temperature variation at the inner collector wall and eliminate cyclic fatigue. The reduced peaks of temperature variations on the inner collector wall are no longer the limiting factor for the size of the collector but rather the critical heat flux of the cooling system. Cyclic thermal fatigue is the main limitation in the lifetime of high-power gyrotron collectors and will cause cracks and plastic deformation over time.

A sweeping system inside the gyrotron vacuum in close proximity to the electron beam is not limited in the sweeping frequency by eddy currents. However, the operation of a normal conducting coil with significant power consumption is not feasible inside the vacuum tube due to the thermal management of the coil. The power consumption of a sweeping system based on an electric field is reduced in comparison to a magnetic field sweeping system.

The spent electron beam in a high-power, high-frequency gyrotron is confined by a strong magnetic field. A strong electric field perpendicular to the magnetic field is required for modification of the electron trajectories as proposed with the $\vec{E}\times\vec{B}$ drift concept [70]. Static magnetic and electric fields are used in the initial idea to separate the spent beam electrons according to their kinetic

energy for an improvement in the collector efficiency. In this chapter, a periodic variation of the electric field and a constant magnetic field are applied for the sweeping of the electron beam in radial direction, similar to the sweeping of the spent electron beam on the first electrode of the CW MDC concept proposed in section 4.2. The variation in radial direction directly correlates with an axial variation of the intersection region of the electron beam with the cylindrical collector wall. This novel idea of an electric field sweeping system is designed for an SDC where a high collector efficiency is no priority. The main goal of a collector with an electric field sweeping system is the elimination of cyclic fatigue due to higher sweeping frequency and the possibility for smaller collector sizes.

5.1 Basic Principle with Infinite Electrodes

For simplicity, an ideal 2D model is analyzed in this section to demonstrate the principle. There is a constant axial magnetic field out of the plane of the polar coordinate system. A circular boundary is placed at a radius $r = R$ with infinite number of electrodes. The electric potential Φ on each electrode is a function of the azimuthal angle θ and time t:

$$[\Phi(\theta, t)]_{r=R} = \Phi_0 \, \sin\left(n\,\theta + 2\,\pi\,\frac{t}{T}\right) \tag{5.1}$$

where the electric potential Φ_0 is the amplitude of this periodic setup, T is the sweeping period and n is an arbitrary integer for the number of periods. The electric potential in the complete cross–section is solved by the Laplace equation to

$$\Phi(r, \theta, t) = \Phi_0 \, \left(\frac{r}{R}\right)^n \, \sin\left(n\,\theta + 2\,\pi\,\frac{t}{T}\right) \tag{5.2}$$

The relationship between the electric field E and the electric potential Φ is

$$\vec{E} = -\vec{\nabla}\Phi = -\frac{\partial\Phi}{\partial r} \cdot \vec{r} - \frac{1}{r}\,\frac{\partial\Phi}{\partial\theta} \cdot \vec{\theta} \tag{5.3}$$

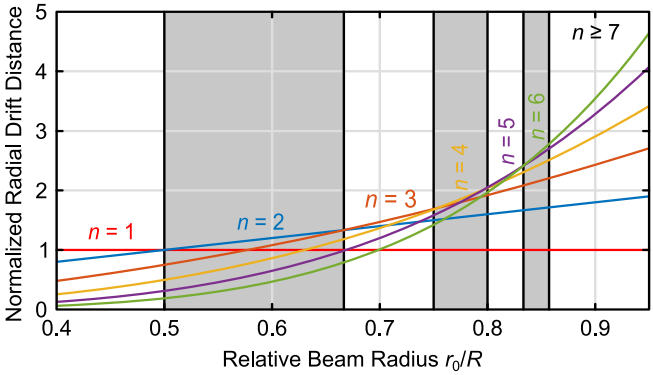

Figure 5.1: Normalized radial electron drift distance in the sweeping region over the relative beam radius for periodic factors of n between 1 to 6 [108].

The drift velocity $\vec{v_\mathrm{d}}$ from Eq. 1.17 of a non-relativistic electron in the axial magnetic field $\vec{B} = B \cdot \vec{z}$ and the perpendicular electric field from Eq. 5.2 is calculated to

$$\vec{v_\mathrm{d}}(r,\theta,t) = -\frac{\Phi_0}{B\,R}\,n\,\left(\frac{r}{R}\right)^{n-1} \cdot \left(\sin\left(n\,\theta + 2\,\pi\,\frac{t}{T}\right)\cdot\vec{r} + \cos\left(n\,\theta + 2\,\pi\,\frac{t}{T}\right)\cdot\vec{\theta}\right) \tag{5.4}$$

The maximum radial drift distance Δr of an electron within a short time interval $\tau \to 0$ is proportional to

$$\Delta r \propto \tau\,n\,\left(\frac{r_0}{R}\right)^{n-1} \tag{5.5}$$

Equation 5.5 shows that the effect of the drift becomes more significant with a larger τ and also when an electron beam is radially closer to the electrodes. Eq. 5.5 is visualized in Fig. 5.1 where the number n is represented by different curves. The radial drift distance is significantly increased for larger n in combination with an electron beam close to the electrodes. However, the relative beam radius is limited in a realistic design to a value not larger as

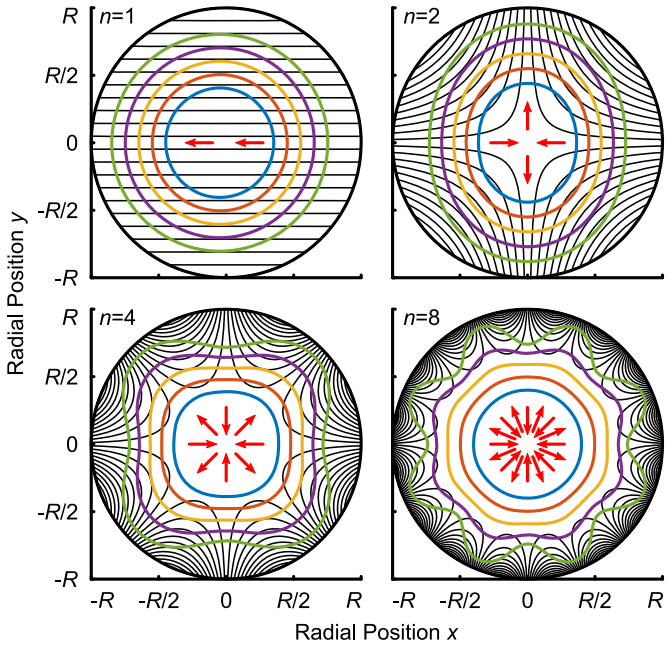

Figure 5.2: Cross–sections of the electric equipotential lines (black) for periodic factors of $n = 1, 2, 4, 8$. Different electron beams are shown after the influence of the sweeping region using $\tau \gg 0$ with relative beam radii of $r_0/R = 0.4, 0.5, 0.6, 0.7$ and 0.8. The radial drift direction is represented with arrows in the center of each plot (red) [108].

approximately 0.9 due to tolerances in the magnetic field and misalignments. In this frame, the maximum reasonable number of repeated potentials in the azimuthal direction is set to $n = 9$, as a larger number will not increase the drift distance. Another limitation to n is the maximum electric field $E_{\max}$, which is limited to around 70 kV/cm to 80 kV/cm to avoid breakdown. The peak to peak potential is limited to the depression potential Φ_{dep} due to axial electric field components of the sweeping structure.

The positions of the beam electrons after the influence of the electric field can be integrated in small time steps. The cross–sections of the electric potential lines (black lines) and electron beams with $r_0/R = 0.4, 0.5, 0.6, 0.7$ and 0.8 are shown in Fig. 5.2 for $n = 1, 2, 4$ and 8, while the azimuthal positions of a

maximum radial drift to the in– and outside are indicated with red arrows. The constant radial position of the electrodes R is critical for larger initial radii of the electron beams with increasing factor n due to the reduced distance between the electrodes and the electron beam. This point is addressed in the realistic conceptual design presented at a later point of this section. The electric fields are not varied over time in these calculations due to the condition of a large period length $T \gg \tau$. Over a larger time frame with periodic variation of the electric field, the electric fields and the shape of the swept electron beam are rotated along the center point in case of an infinite number of electrodes.

5.2 Model with Finite Number of Electrodes

A design for an electrical sweeping system with an unlimited number of electrodes is not feasible for a realistic design approach. The number of electrodes m is defined as $m = p\,n$ where n is the number of periods and p is the finite number of unique potentials, in contrast to the ideal model from the previous section corresponding to $p = \infty$ in which the influence of n is shown. The maximum electron drift in the cross–section of the electric sweeping system is constant over time for $p = \infty$ as the maximum potential difference is always $2\,\Phi_0$. The influence of a realistic finite value for p is discussed in this section for even numbers to achieve an average electric potential in the cross–section equal to zero. The electric potentials of the electrodes are defined with eq. 5.1 at the azimuthal center position of each electrode i (1, . . . , m) which is at an angle of

$$\theta(i) = \frac{2\,\pi}{n}\left(\frac{i}{p} - \frac{1}{4}\right) \tag{5.6}$$

The electric field between the electrodes is dependent on the size and shape of the electrodes however, the absolute electric potential in the center between two neighboring electrodes i and j at the radius R is less than or equal to the absolute average value of both potentials or

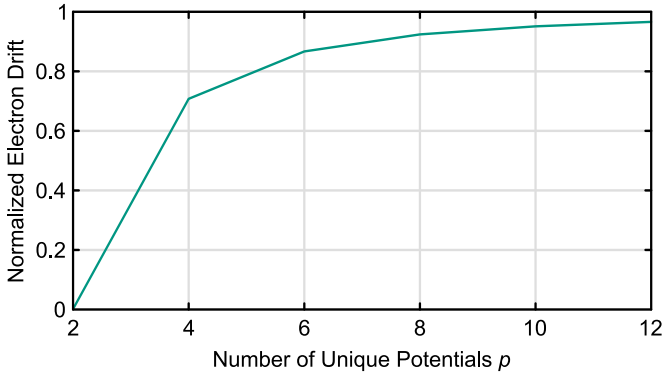

Figure 5.3: Normalized minimal electron drift distance over the number of unique potentials p [108].

$$|\Phi(i,j,t)| \leq \left| \frac{\Phi(\theta(i),t) + \Phi(\theta(j),t)}{2} \right| \tag{5.7}$$

$$= \frac{\Phi_0}{2} \left| \left(\sin\left(n\,\theta(i) + 2\,\pi\,\frac{t}{T} \right) + \sin\left(n\,\theta(j) + 2\,\pi\,\frac{t}{T} \right) \right) \right| \tag{5.8}$$

$$= \Phi_0\,\cos\left(\frac{\pi}{p}\right) \left| \sin\left(\pi\,\left(\frac{i+j}{p} - \frac{1}{2} \right) + 2\,\pi\,\frac{t}{T} \right) \right| \tag{5.9}$$

The maximum possible absolute electric potential $\Phi_{\max}$ over the period T at the center position between two neighboring electrodes results to

$$|\Phi_{\max}| \leq \Phi_0\,\cos\left(\frac{\pi}{p}\right) \tag{5.10}$$

The maximum electron drift in the cross–section of the electric sweeping system over the period T is minimized when the electric potential at the center position between two neighboring electrodes is maximized. The normalized maximum possible electron drift at the azimuthal position between two electrodes over the number of unique potentials is shown in Fig. 5.3. It is increased with p and converges to 1 for $p = \infty$, as expected with Eq. 5.10. The minimal

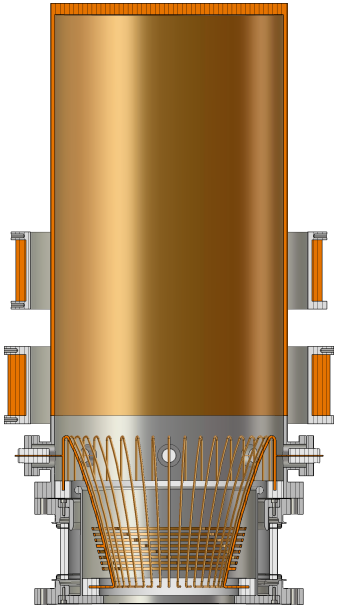

Figure 5.4: 3D–geometry of a collector with an $\vec{E}\times\vec{B}$ sweeping structure. The periodic factor is set to $n = 5$ and the number unique potentials to $p = 8$ for a total of 40 electrodes [108].

value of p to achieve an electron drift in the complete cross–section of the sweeping system is four. The difference between the maximum and minimum drift distance in a sweeping cycle is reduced to less than 10 % for $p \geq 8$. The complexity of a realistic design approach for an electric field sweeping system is significantly increased with more unique potentials due to the increased number of vacuum feedthroughs for every potential. The number of required power supplies is also increased with p.

5.3 Demonstration of the Concept

The conceptual design approach of the electric field sweeping system is optimized for the KIT 2 MW 170 GHz coaxial-cavity gyrotron[33]. The nominal depression potential of $\Phi_{\mathrm{dep}} = -35\,\mathrm{kV}$ as applied in a traditional SDC is used in simulations for the collector with an electric field sweeping system. A 3D geometry of a collector with an electric field sweeping system is shown in Fig. 5.4. The electrodes for the electric field are axially placed at the entrance of the collector due to the reduced magnetic field for an increased electron drift. The radial center position of the electrodes is set to achieve a relative outside beam radius of 0.85. The maximum possible amplitude of the sweeping potential of $\Phi_0 = \Phi_{\mathrm{dep}}/2 = 17.5\,\mathrm{kV}$ is applied without exceeding the limit of the breakdown electric field due to the increased radial dimensions at the collector entrance. The magnetic field of the gyrotron magnet is diverged with increasing distance to the cavity along the axis and the radial dimension of the electrodes in axial direction is adapted to the diverging electron beam along the sweeping region. Additional constant current collector coils are used to modify the magnetic field in the collector above the electric field sweeping area to reduce the incident angle of the magnetic field lines with the collector wall. The effectiveness of the electric field sweeping system and the electron beam width at the collector wall are increased with a shallower incidence angle. Currents of approximately 5 kA·t and 2 kA·t are applied to the lower and upper coil, respectively. The inner radius of the cylindrical copper collector surface is set to 200 mm with a length of 700 mm. The number of repeated potentials is set to $n = 5$ to achieve an optimal average radial drift distance for the beam electrons with the largest and smallest initial radial position. The number of unique potentials is set to $p = 8$ for a compromise in a high minimal drift distance and an acceptable complexity with a phase difference of 45°. In total, 40 electrodes are used for the electric field sweeping system. Each electrode is built out of a metallic rod with circular cross–section with a radial dimension of 2 mm. The commercially available voltage feedthroughs are located in 45° angles at the upper end of the $\vec{E}\times\vec{B}$ drift region and are each connected to a single rod. Each group of 5 rods is electrically and mechanically connected with metallic rings to distribute the electric potential in the complete structure. The $\vec{E}\times\vec{B}$ structure is embedded in two ceramic rings at the top and bottom of the rods for mechanical support. The large insulator with flanges and both

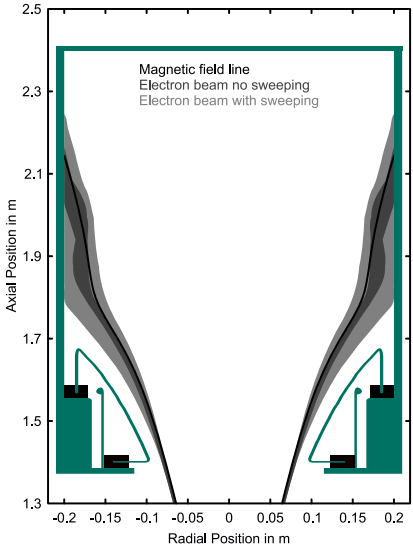

Figure 5.5: Schematic stretched view of the cut plane of the collector with a factor of 1 over 2 for the y– and x–axis. Magnetic field lines of the electron beam center (black), the electron beam thickness without sweeping (medium gray) and the electron beam thickness with sweeping (light gray) [108].

coils are modular gyrotron components at IHM/KIT and could be used for a concept prototype.

The magnetic field line of the electron beam center as well as the electron beam thickness in 2D are shown in Fig. 5.5 for the SDC with and without an applied electric field sweeping potential. The magnetic field in the collector region above the electric field sweeping area is tuned to achieve a non–adiabatic transition of the electron beam for an increased beam thickness, although it should be noted that a non–adiabatic transition of the electron beam without sweeping is not sufficient for an acceptable power loading density at the collector wall. The intersection area of the electron beam with the collector wall is significantly increased with the electric field sweeping system, which is shown with the momentary and time–averaged power loading densities at the collector surface without considering space charge or secondary electron emission as shown in Fig. 5.6 and 5.7, respectively. The power loading distributions are only shown in a 72° segment due to the symmetry condition of $n = 5$.

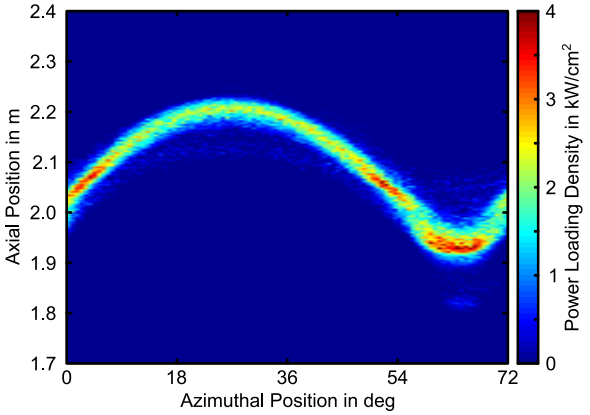

Figure 5.6: Momentary power loading at the cylindrical collector at a 72° segment due to the symmetry of the periodic factor of $n = 5$ [108].

The maximum momentary power loading density is reduced from 6 kW/cm^2 to 4 kW/cm^2 in comparison to a traditional SDC with 200 mm inner radius for the KIT 2 MW 170 GHz coaxial-cavity gyrotron, which is a result of the shallower incident angle between the electron beam and the collector wall as well as the increased beam thickness due to the $\vec{E}\times\vec{B}$ drift and the non–adiabatic transition. The maximum power loading density of the time–averaged wall loading is 600 W/cm^2, compared to the maximum acceptable averaged power loading density of conventional CW collectors with magnetic field sweeping is considered to 500 W/cm^2. Additional work must be done to verify that the increased heat flux is compatible with existing gyrotron collector cooling concepts.

An azimuthal density non–uniformity of the electron beam is a result of the azimuthal electron drift due to radial electric field components of the sweeping structure. An additional electric field is generated inside the electron beam with an azimuthal density non–uniformity with a similar shape to the electric field of the electric field sweeping electrodes [55]. Additional radial and azimuthal drift movements of the electrons will be observed when the space charge effect is included in the simulations. The momentary power loading density at the collector surface is slightly increased and shifted in phase in the positive azimuthal direction when the space charge effect is considered. The influence of the space charge is best visible in the angular power loading density shown in

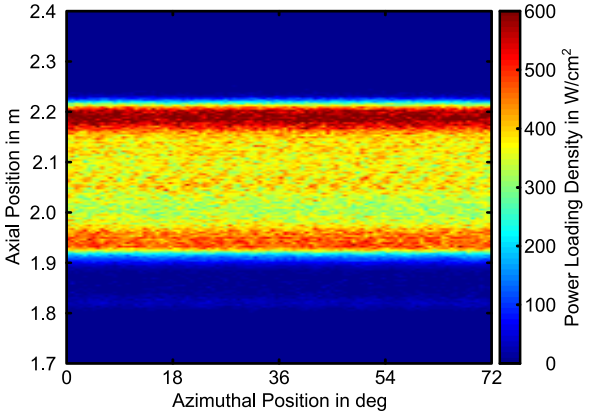

Figure 5.7: Time average power loading density as a combination of 20 individual momentary time simulations at different phases of the sweeping system [108].

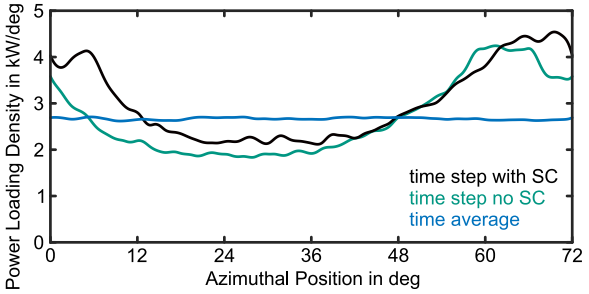

Figure 5.8: Angular power loading density for a momentary time step with space charge, a momentary time step without space charge and the time average power loading without space charge [108].

Fig. 5.8. The most challenging part of the electric field sweeping system is the Secondary Electron Emission (SEE). At the current state, a current is collected at the sweeping structure when SEE is considered. Future work must focus on the reduction of this current, as increased cooling of the sweeping structure, more than already necessary due to stray radiation inside the gyrotron, will increase the system complexity significantly.

5.4 Effects of Increased Sweeping Frequency

The goal of the electric field sweeping system is an increased sweeping frequency for a reduced temperature variation at the inner collector surface. A reduced temperature variation correlates with an increased life expectancy of the collector due to reduced cyclic fatigue. Heat transfer simulations are performed for different sweeping frequencies. The power loading distribution of the spent electron beam, as shown in Fig. 5.6, is applied to the inner collector wall with a thickness of 10 mm to 20 mm. The outer collector wall is corrugated with 10 mm squared grooves to represent a HV cooling structure as used in CW gyrotrons with heat transfer coefficients at the outside set to 23 kW/m^{2}K and around the groove to 8.5 kW/m^{2}K [109] with an external temperature of 20 °C. The average temperature obtained at a sample point near the maximum power loading is between 370 °C to 380 °C for all sweeping frequencies. However, the average temperature depends strongly on the heat transfer coefficient, which is not well-defined for HV cooling. The temperature variation at the sample point is only slightly dependent on the correct heat transfer coefficient. The influence of the sweeping frequency on the temperature variations is much stronger due to the slow heat transfer through the collector wall material, which depends on the heat capacity and thermal conductivity of copper. Simulation results of the temperature variations at a sample point for different sweeping frequencies are shown in Fig. 5.9. The reduction in the temperature variation for a sweeping frequency over 10 kHz with a similar power loading distribution is very small. The temperature variation of the hottest point in a collector with LMFS and a 10 Hz triangular waveform in the sweeping coil usually ranges from 150 K to 200 K within one sweep cycle [110]. The temperature variation of a sample point in a collector with TMFS and 50 Hz sweeping should be slightly above the 23.2 K observed for the electric field sweeping due to an increased instantaneous power loading density.

It should be noted that the electric field in the cross–section of the $\vec{E} \times \vec{B}$ drift region is very similar to a transverse electric field mode with the form $\mathrm{TE}_{\mathrm{n},1}$ in a circular waveguide. However, the outer boundary in the electric field sweeping system is not an electrical conductor thus the electric field lines are not orthogonal to the outer boundary. In theory, it should be possible to increase the electric field sweeping frequency until the cutoff frequency of the $\mathrm{TE}_{\mathrm{n},1}$ mode is reached. The lowest cutoff frequency in the collector region with

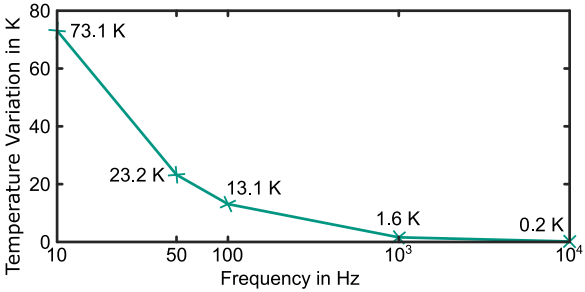

Figure 5.9: Temperature variations at the inner collector wall for different sweeping frequencies [108].

200 mm inner radius for a $TE_{n,1}$ is for $n = 1$ at 439 MHz. The cutoff frequency for the $TE_{5,1}$ as used in the conceptual design is at 1.53 GHz. However, the characteristic time τ of the electrons in the electric field region must be taken into account for such high sweeping frequencies.

5.5 Summary

A different approach of the $\vec{E}\times\vec{B}$ drift in gyrotron collectors is presented with the novel electron beam sweeping system. The mechanism, based on the periodic variation of an electric field instead of a magnetic field, is presented and analyzed. A conceptual design for a 2 MW 170 GHz CW fusion gyrotron is presented as an example for this new type of electron beam sweeping system. A strong $\vec{E}\times\vec{B}$ drift is achieved in the radial direction to alternate the axial position where the electron beam impinges the collector wall. To further amplify the sweeping effect, the static magnetic field in the collector region is optimized.

The sweeping frequency can be significantly increased for the variation of the electric field, as it is not limited by eddy currents which attenuate the magnetic field inside a collector with traditional magnetic field sweeping. The 2 magnetic field sweeping systems are limited to sweeping frequencies of 10 Hz up to 50 Hz which should result in temperature variations at the inner collector wall of 23 K up to 73 K during a single sweeping cycle in a collector with an inner radius of 200 mm. With the increased sweeping frequency of the electric field sweeping,

the temperature variation at the inner collector wall is significantly reduced and nearly eliminated for sweeping frequencies above 10 kHz. The lifetime of the collector can be significantly increased with the decreased cyclic fatigue with is caused by the periodic temperature variation.

6 Conclusion

In this work, the development, optimization and fabrication of the first SP MDC prototype for a MW-class high-power gyrotron is performed. At first, the requirements on the experimental equipment are discussed, which is followed by the identification of the most preferred MDC design concept. This design concept is further developed into a balanced prototype design which is focused on simplicity and manufacturability while maintaining compact dimensions and a promising electrical performance.

The developed SP MDC prototype represents a significant advance in an optimized electromagnetic configuration, simplified thermal management, a modular mechanical design, and operational versatility. The magnetic configuration of the SP MDC prototype is optimized to include only 3 dedicated collector coils for a constant beam radius in the $\vec{E}\times\vec{B}$ drift region of 98 mm. The electrode configuration, which is the key factor for the required electric field, is based on a hollow cylindrical design and a systematic investigation of the electrode geometry. These two elements are critical for an optimized $\vec{E}\times\vec{B}$ drift and efficient electron beam collection, minimizing power losses in the collector and limiting the reflected current. A high collector efficiency of 78.8 % is achieved with a minor reflected current at around 50 mA.

The thermal management for SP operation is considered, due to the limitation of the prototype, differently to traditional SP SDCs. It bases on the simplified mechanical design with electrodes enclosed in a vacuum housing. This is done as without the interface between the electrodes to the surroundings, the transport of the generated heat is not guaranteed. The mechanical design of the SP MDC prototype emphasizes modularity and ease of assembly, while maintaining compact dimensions with a length of less than 1.2 m and an outer radius of 235 mm without the additional coils. This approach not only facilitates prototyping and testing but also paves the way for upgrading of components, which is crucial for maintaining the long-term functionality of the prototype as

a toolkit for experimental MDC verification. The various mechanical components are described in detail, including their materials, fabrication processes, and assembly techniques. The operational versatility of the SP MDC prototype is theoretically investigated with different gyrotron configurations, proving its robustness across various operational scenarios. The prototype's ability to function effectively under different conditions ensures that it can be integrated into a wide range of systems, making it a versatile and robust solution.

The insights gained from the SP MDC prototype lay a solid foundation for the major and most critical step of development: transitioning to CW operation. In this work, it is indicated that the principles and design strategies applied in the SP prototype can be effectively scaled to CW operation, promising significant efficiency gains and power savings in long-duration applications. The CW MDC requires an up-scaled version of the SP prototype electrodes to handle CW power loads by decreased power loading densities. This includes larger radial and axial dimensions, as well as an optimized voltage operation point of the collector and an electron beam sweeping. Implementation of effective electron beam sweeping methods is crucial for managing thermal loads and preventing localized overheating by staying within the current technical limit of 500 W/cm^2 for the heat load. Two different techniques for electron beam sweeping are explored for the CW MDC, including longitudinal magnetic field sweeping and variation of the depression potentials to distribute the electron beam across the collector surface. Detailed analyses of the mechanical deformation under thermal load that the collector will be subjected to during CW operation are investigated during the CW MDC optimization. An outlook is provided in this work for the design modifications needed to accommodate these stresses. The novel idea of electron beam sweeping with electric fields is further expanded to a possible design concept for implementation in an SDC to reduce the temperature variations and thus thermal stresses.

In conclusion, the research presented in this work marks a significant step forward in the development of efficient, high-power gyrotrons. The successful prototyping and testing of the SP MDC will demonstrate the feasibility and benefits of advanced collector designs. The transition to CW operation holds the promise of even greater power gains in long-duration operation. The continued evolution of MDC technology, driven by ongoing research, will play a pivotal role in meeting the growing demands for high-power microwave and millimeter-wave technologies in scientific, industrial, and energy applications.

Bibliography

[1] A. Kerekeš, L. Breuning, A. von Müller, J. Gawlick, F. Warmer, S. Fietz, R. Kembleton, S. Ciattaglia, W. Hering, H. Zohm, and T. Hamacher. Operational characterization of tokamak and stellarator type fusion power plants from an energy system perspective. *Fusion Engineering and Design*, 190:113496, May 2023. doi: 10.1016/j.fusengdes.2023.113496.

[2] M. V. Kartikeyan, E. Borie, and M. K. A. Thumm. *Gyrotrons: High-power microwave and millimeter wave technology*. Advanced Texts in Physics. Springer, Berlin, Heidelberg, 2013. ISBN 978-3-662-07637-8. doi: 10.1007/978-3-662-07637-8.

[3] H. P. Laqua, K. A. Avramidis, H. Braune, I. Chelis, G. Gantenbein, S. Illy, Z. Ioannidis, J. Jelonnek, J. Jin, L. Krier, C. Lechte, A. Leggieri, F. Legrand, S. Marsen, D. Moseev, H. Oosterbeek, T. Rzesnicki, T. Ruess, T. Stange, M. Thumm, I. Tigelis, and R. C. Wolf. The ECRH-Power Upgrade at the Wendelstein 7-X Stellarator. *EPJ Web of Conferences*, 277:04003, 2023. doi: 10.1051/epjconf/202327704003.

[4] T. Omori, M. A. Henderson, F. Albajar, S. Alberti, U. Baruah, T. S. Bigelow, B. Beckett, R. Bertizzolo, T. Bonicelli, A. Bruschi, J. B. Caughman, R. Chavan, S. Cirant, A. Collazos, D. Cox, C. Darbos, M. R. de Baar, G. Denisov, D. Farina, F. Gandini, T. Gassmann, T. P. Goodman, R. Heidinger, J.-P. Hogge, S. Illy, O. Jean, J. Jin, K. Kajiwara, W. Kasparek, A. Kasugai, S. Kern, N. Kobayashi, H. Kumric, J. D. Landis, A. Moro, C. Nazare, Y. Oda, I. Pagonakis, B. Piosczyk, P. Platania, B. Plaum, E. Poli, L. Porte, D. Purohit, G. Ramponi, S. L. Rao, D. A. Rasmussen, D. M. S. Ronden, T. Rzesnicki, G. Saibene, K. Sakamoto, F. Sanchez, T. Scherer, M. A. Shapiro, C. Sozzi, P. Spaeh, D. Strauss, O. Sauter, K. Takahashi, R. J. Temkin, M. Thumm, M. Q. Tran, V. S. Udintsev, and H. Zohm. Overview of the ITER EC H&CD system

and its capabilities. *Fusion Engineering and Design*, 86(6):951–954, October 2011. doi: 10.1016/j.fusengdes.2011.02.040.

[5] M. Preynas, M. Schneider, J. M. Arroyo, F. Beaumont, N Casal, M Choe, G. Carannante, F. Gandini, M. A. Henderson, T. Omori, and S. Pascal. New modelling capabilities to support the ITER EC H&CD System optimisation and preparation of plasma operation. *EPJ Web of Conferences*, 277:01004, 2023. doi: 10.1051/epjconf/202327701004.

[6] T. Donné, W. Morris, X. Litaudon, C. Hidalgo, D. McDonald, H. Zohm, E. Diegele, A. Möslang, K. Nordlund, G. Federici, P. Sonato, C. Waldon, D. Borba, and P. Helander. European research roadmap to the realisation of fusion energy (long version). Technical report, EUROfusion, Garching / Munich, Germany, 2018. URL `https://www.euro-fusion.org/fileadmin/user_upload/EUROfusion/Documents/2018_Research_roadmap_long_version_01.pdf`. Accessed on: 2023-01-16 11:27:10.

[7] W. Biel. DEMO, September 2022. URL `https://www.fz-juelich.de/en/iek/iek-4/forschung/demo/`. Accessed on: 2023-01-16 11:42:44.

[8] A. Bruschi, J.-P. Hogge, J. Jelonnek, D. Strauss, C. Wu, G. Aiello, K. Avramidis, B. Baiocchi, D. Birlan, R. Chavan, I. Chelis, A. Clement, A. Collaku, F. Crisinel, R. Difonzo, B. Ell, F. Fanale, P. Fanelli, L. Figini, E. Gajetti, G. Gantenbein, S. Garavaglia, T. P. Goodman, S. Illy, Z. Ioannidis, J. Jin, G. Latsas, C. L. M. Borderas, S. Marsen, A. Moro, M. Noël, D. Peponis, T. Pinna, P. Platania, N. Rispoli, T. Ruess, T. Rzesnicki, A. Salvitti, L. Savoldi, T. Scherer, S. Schreck, A. Simonetto, P. Spaeh, S. Stanculovic, T. Stange, M. Thumm, I. Tigelis, C. Tsironis, D. Wagner, and A. Xydou. Conceptual design of a modular EC heating system for EU-DEMO. *Nuclear Fusion*, 64(10):106003, August 2024. doi: 10.1088/1741-4326/ad66e3.

[9] B. Lindley, T. Roulstone, G. Locatelli, and M. Rooney. Can fusion energy be cost-competitive and commercially viable? An analysis of magnetically confined reactors. *Energy Policy*, 177:113511, June 2023. doi: 10.1016/j.enpol.2023.113511.

[10] G. S. Nusinovich, M. K. A. Thumm, and M. I. Petelin. The Gyrotron at 50: Historical Overview. *Journal of Infrared, Millimeter, and Terahertz Waves*, 35(4):325–381, April 2014. doi: 10.1007/s10762-014-0050-7.

[11] S. Sabchevski, E. Di Palma, I. Spassovsky, and G. Dattoli. Gyrotrons as High-Frequency Drivers for Undulators and High-Gradient Accelerators. *Applied Sciences*, 12(12):6101, January 2022. doi: 10.3390/app12126101.

[12] T. Idehara, S. P. Sabchevski, M. Glyavin, and S. Mitsudo. The Gyrotrons as Promising Radiation Sources for THz Sensing and Imaging. *Applied Sciences*, 10(3):980, January 2020. doi: 10.3390/app10030980.

[13] S. Illy. *Untersuchungen von Strahlinstabilitäten in der Kompressionszone von Gyrotron- Oszillatoren mit Hilfe der kinetischen Theorie und zeitabhängiger Particle-in-Cell- Simulationen*, volume 6037 of *Wissenschaftliche Berichte Forschungszentrum Karlsruhe*. Universität Karlsruhe (TH), 1997. doi: 10.5445/IR/105397.

[14] P. C. Kalaria, K. A. Avramidis, G. Gantenbein, S. Illy, I. Gr. Pagonakis, M. Thumm, and J. Jelonnek. Mode competition control using triode-type start-up scenario for a 236 GHz gyrotron for DEMO. In *11th German Microwave Conference (GeMiC)*, pages 287–290, March 2018. doi: 10.23919/GEMIC.2018.8335086.

[15] S. Ruess, I. Gr. Pagonakis, G. Gantenbein, S. Illy, T. Kobarg, T. Rzesnicki, M. Thumm, J. Weggen, and J. Jelonnek. An Inverse Magnetron Injection Gun for the KIT 2-MW Coaxial-Cavity Gyrotron. *IEEE Transactions on Electron Devices*, 63(5):2104–2109, May 2016. doi: 10.1109/TED.2016.2540298.

[16] S. Ruess. *Pushing the KIT 2 MW Coaxial-Cavity Short-Pulse Gyrotron Towards a DEMO Relevant Design*, volume 15 of *Karlsruher Forschungsberichte aus dem Institut für Hochleistungsimpuls- und Mikrowellentechnik*. Karlsruher Institut für Technologie (KIT), 2020. ISBN 978-3-7315-1024-6. doi: 10.5445/KSP/1000117846.

[17] I. Gr. Pagonakis, S. Alberti, K. Avramidis, F. Legrand, G. Gantenbein, J. Genoud, J.-P. Hogge, S. Illy, Z. Ioannidis, P. Kalaria, B. Piosczyk, S. Ruess, T. Ruess, T. Rzesnicki, M.-Q. Tran, T.-M.

Tran, M. Thumm, I. Vomvoridis, and J. Jelonnek. Overview on recent progress in magnetron injection gun theory and design for high power gyrotrons. *EPJ Web of Conferences*, 203:04011, 2019. doi: 10.1051/epjconf/201920304011.

[18] C. Wu. *Conceptual Studies of Multistage Depressed Collectors for Gyrotrons*, volume 13 of *Karlsruher Forschungsberichte aus dem Institut für Hochleistungsimpuls- und Mikrowellentechnik*. KIT Scientific Publishing, Karlsruhe, 2019. ISBN 978-3-7315-0934-9. doi: 10.5445/KSP/1000094598.

[19] P. C. Kalaria, K. A. Avramidis, J. Franck, G. Gantenbein, S. Illy, I. Gr. Pagonakis, M. Thumm, and J. Jelonnek. Systematic cavity design approach for a multi-frequency gyrotron for DEMO and study of its RF behavior. *Physics of Plasmas*, 23(9):092503, September 2016. doi: 10.1063/1.4962238.

[20] D. M Pozar. *Microwave Engineering*. John Wiley & Sons, 4th edition edition, November 2011. ISBN 978-0-470-63155-3.

[21] D. V. Kas'yanenko, O. I. Louksha, B. Piosczyk, G. G. Sominsky, and M. Thumm. Low-Frequency Parasitic Space-Charge Oscillations in the Helical Electron Beam of a Gyrotron. *Radiophysics and Quantum Electronics*, 47(5):414–420, May 2004. doi: 10.1023/B:RAQE.0000046315.10190.1c.

[22] G. S. Nusinovich, R. Temkin, and V. Granatstein. *Introduction to the Physics of Gyrotrons*. Johns Hopkins University Press, Baltimore, 2004. ISBN 978-1-4214-2764-5.

[23] A. S. Gilmour, Jr. *Klystrons, Traveling Wave Tubes, Magnetrons, Crossed-field Amplifiers, and Gyrotrons*. Artech House, 2011. ISBN 978-1-60807-185-2.

[24] J. Jin, B. Piosczyk, M. Thumm, T. Rzesnicki, and S. Zhang. Quasi-Optical Mode Converter/Mirror System for a High-Power Coaxial-Cavity Gyrotron. *IEEE Transactions on Plasma Science*, 34(4):1508–1515, August 2006. doi: 10.1109/TPS.2006.877627.

[25] J. Jin, J. Flamm, J. Jelonnek, S. Kern, I. Pagonakis, T. Rzesnicki, and M. Thumm. High-Efficiency Quasi-Optical Mode Converter for a 1-MW

\rm TE_32,9-Mode Gyrotron. *IEEE Transactions on Plasma Science*, 41(10):2748–2753, October 2013. doi: 10.1109/TPS.2013.2261322.

[26] K. A. Avramidis, Z. C. Ioannidis, S. Kern, A. Samartsev, I. Gr. Pagonakis, I. G. Tigelis, and J. Jelonnek. A comparative study on the modeling of dynamic after-cavity interaction in gyrotrons. *Physics of Plasmas*, 22(5):053106, May 2015. doi: 10.1063/1.4919924.

[27] B. Piosczyk, C. T. Iatrou, G. Dammertz, and M. Thumm. Single-stage depressed collectors for gyrotrons. *IEEE Transactions on Plasma Science*, 24(3):579–585, June 1996. doi: 10.1109/27.532940.

[28] Deutsches Kupferinstitut. Cu-HCP, 2005. URL `https://kupfer.de/wp-content/uploads/2019/11/Cu-HCP.pdf`. Accessed on: 2024-01-30 08:58:25.

[29] Höganäs. GLIDCOP AL-15 Dispersion Strengthened Copper, 2013. URL `https://www.hoganas.com/api/Brochure/?pdf=/globalassets/downloads/libary/glidcop_glidcop-al-15-applications_0667hog.pdf&mode=brochure&title=GLIDCOP_GLIDCOP%20AL-15%20applications_0667HOG.pdf#page=1`. Accessed on: 2024-02-08 06:56:30.

[30] Deutsches Kupferinstitut. CuCr1Zr, 2005. URL `https://kupfer.de/wp-content/uploads/2019/11/CuCr1Zr.pdf`. Accessed on: 2024-01-23 07:45:27.

[31] J. R. Pierce. *Theory and design of electron beams*. The Bell Telephone Laboratories series. D. Van nostrand company, Inc., Princeton, N.J., 2. ed. edition, 1954. ISBN 978-1-124-09130-3.

[32] G. Dammertz, S. Alberti, A. Arnold, E. Borie, V. Erckmann, G. Gantenbein, E. Giguet, R. Heidinger, J.-P. Hogge, S. Illy, W. Kasparek, K. Koppenburg, M. Kuntze, H. P. Laqua, G. LeCloarec, Y. LeGoff, W. Leonhardt, C. Lievin, R. Magne, G. Michel, G. Muller, G. Neffe, B. Piosczyk, M. Schmid, K. Schworer, M. K. Thumm, and M. Q. Tran. Development of a 140-GHz 1-MW continuous wave gyrotron for the W7-X stellarator. *IEEE Transactions on Plasma Science*, 30(3):808–818, June 2002. doi: 10.1109/TPS.2002.801509.

[33] T. Rzesnicki, B. Piosczyk, S. Kern, S. Illy, J. Jin, A. Samartsev, A. Schlaich, and M. Thumm. 2.2-MW Record Power of the 170-GHz European Preprototype Coaxial-Cavity Gyrotron for ITER. *IEEE Transactions on Plasma Science*, 38(6):1141–1149, June 2010. doi: 10.1109/TPS.2010.2040842.

[34] M. Yu. Glyavin, A. N. Kuftin, N. P. Venediktov, and V. E. Zapevalov. Experimental investigation of a 110 GHz/1 MW gyrotron with the one-step depressed collector. *International Journal of Infrared and Millimeter Waves*, 18(11):2129–2136, November 1997. doi: 10.1007/BF02678255.

[35] K. Sakamoto, M. Tsuneoka, A. Kasugai, T. Imai, T. Kariya, K. Hayashi, and Y. Mitsunaka. Major Improvement of Gyrotron Efficiency with Beam Energy Recovery. *Physical Review Letters*, 73(26):3532–3535, December 1994. doi: 10.1103/PhysRevLett.73.3532.

[36] M. Thumm. Progress in gyrotron development. *Fusion Engineering and Design*, 66-68:69–90, September 2003. doi: 10.1016/S0920-3796(03)00132-7.

[37] K. Felch, M. Blank, P. Borchard, P. Cahalan, S. Cauffman, T. S. Chu, and H. Jory. Recent ITER-Relevant Gyrotron Tests. *Journal of Physics: Conference Series*, 25(1):13, January 2005. doi: 10.1088/1742-6596/25/1/003.

[38] M. Schmid, S. Illy, G. Dammertz, V. Erckmann, and M. Thumm. Transverse field collector sweep system for high power CW gyrotrons. *Fusion Engineering and Design*, 82(5):744–750, October 2007. doi: 10.1016/j.fusengdes.2007.06.008.

[39] G. Dammertz, S. Illy, B. Piosczyk, M. Schmid, and D. Bariou. Collector sweeping systems for high power gyrotrons. *Joint 30th International Conference on Infrared and Millimeter Waves and 13th International Conference on Terahertz Electronics*, 1:293–294 vol. 1, September 2005. doi: 10.1109/ICIMW.2005.1572524.

[40] V. Erckmann, M. Schmid, H. P. Laqua, G. Dammertz, S. Illy, H. Braune, F. Hollmann, F. Noke, and F. Purps. Advanced Gyrotron Collector Sweeping with smooth Power Distribution. In *4th IAEA Technical*

Meeting on ECRH Physics and Technology for ITER, pages pp. 1–5, January 2007.

[41] S. Illy, K. A. Avramidis, L. Jackowski, W. Kdous, and John Jelonnek. Optimized Vertical Collector Sweeping for High Power CW Gyrotrons Using Advanced Current Waveforms. *43rd International Conference on Infrared, Millimeter, and Terahertz Waves (IRMMW-THz)*, pages 1–2, September 2018. doi: 10.1109/IRMMW-THz.2018.8509998.

[42] V. Erckmann, G. Dammertz, and M. Schmid. Verfahren Und Vorrichtung Zur Kollektor-Sweeping-Steuerung Eines Elektronenstrahls, August 2011.

[43] M. K. Thumm. Progress on Gyrotrons for ITER and Future Fusion Reactors. *AIP Conference Proceedings*, 1187(1):21–28, November 2009. doi: 10.1063/1.3273732.

[44] Z. Ioannidis, T. Rzesnicki, F. Albajar, S. Alberti, K. Avramidis, W. Bin, T. Bonicelli, A. Bruschi, I. Chelis, F. Fanale, G. Gantenbein, V. Hermann, J.-P. Hogge, S. Illy, J. Jin, J. Jelonnek, W. Kasparek, G. Latsas, C. Lechte, F. Legrand, I. Pagonakis, F. Sanchez, M. Schmid, C. Schlatter, M. Thumm, I. Tigelis, M. Q. Tran, A. Zisis, and A. Zein. Report of recent experiments with the European 1 MW, 170 GHz CW and SP prototype gyrotrons for ITER. *EPJ Web of Conferences*, 203:04006, 2019. doi: 10.1051/epjconf/201920304006.

[45] W.-L. Cheng, W.-W. Zhang, H. Chen, and L. Hu. Spray cooling and flash evaporation cooling: The current development and application. *Renewable and Sustainable Energy Reviews*, 55:614–628, March 2016. doi: 10.1016/j.rser.2015.11.014.

[46] G. Cattadori, G. P. Gaspari, G. P. Celata, M. Cumo, A. Mariani, and G. Zummo. Hypervapotron technique in subcooled flow boiling CHF. *Experimental Thermal and Fluid Science*, 7(3):230–240, October 1993. doi: 10.1016/0894-1777(93)90006-5.

[47] G. Lorenzini and C. Biserni. A Vapotron Effect Application for Electronic Equipment Cooling. *Journal of Electronic Packaging*, 125(4): 475–479, December 2003. doi: 10.1115/1.1615796.

[48] D. Bariou and C. Lievin. Extract from RT 5307 design report ITER 170 GHz Gyrotron. Technical Report EFDA-03/960, December 2007.

[49] K. A. Avramidis, Z. C. Ioannidis, G. Aiello, P. Bénin, I. Chelis, A. Dinklage, G. Gantenbein, S. Illy, J. Jelonnek, J. Jin, H. P. Laqua, A. Leggieri, F. Legrand, A. Marek, S. Marsen, I. Gr. Pagonakis, T. Ruess, T. Rzesnicki, T. Scherer, D. Strauss, M. Thumm, I. Tigelis, D. Wagner, J. Weggen, and R. C. Wolf. Towards a 1.5 MW, 140 GHz gyrotron for the upgraded ECRH system at W7-X. *Fusion engineering and design*, 164:112173, 2021. doi: 10.1016/j.fusengdes.2020.112173.

[50] M. H. Beringer. *Design studies towards a 4 MW 170 GHz coaxial-cavity gyrotron*, volume 1 of *Karlsruher Forschungsberichte aus dem Institut für Hochleistungsimpuls- und Mikrowellentechnik*. Karlsruher Institut für Technologie (KIT), Karlsruhe, 2011. ISBN 978-3-86644-663-2. doi: 10.5445/KSP/1000022514.

[51] I. Gr. Pagonakis, F. Li, S. Illy, B. Piosczyk, S. Alberti, J.-P. Hogge, S. Kern, M. Henderson, and C. Darbos. Study of the ITER Stray Magnetic Field Effect on the EU 170-GHz 2-MW Coaxial Cavity Gyrotron. *IEEE Transactions on Plasma Science*, 40(7):1945–1956, July 2012. doi: 10.1109/TPS.2012.2197420.

[52] B. Ell, I. Gr. Pagonakis, G. Gantenbein, S. Illy, M. Thumm, and J. Jelonnek. Study of the Influence of Stray Magnetic Fields on the Operation of the European Gyrotron for ITER. *IEEE Transactions on Electron Devices*, 64(8):3421–3428, August 2017. doi: 10.1109/TED.2017.2716385.

[53] C. Christodoulides. Equivalence of the Ampere and Biot-Savart force laws in magnetostatics. *Journal of Physics A: Mathematical and General*, 20(8):2037, June 1987. doi: 10.1088/0305-4470/20/8/022.

[54] J. Gr. Pagonakis and J. L. Vomvoridis. The self-consistent 3D trajectory electrostatic code ARIADNE for gyrotron beam tunnel simulation. In *Joint 29th International Conference on Infrared and Millimeter Waves and 12th International Conference on Terahertz Electronics*, pages 657–658, Karlsruhe, Germany, September 2004. doi: 10.1109/ICIMW.2004.1422262.

[55] J. Gr. Pagonakis and J. L. Vomvoridis. Evolution of an electron beam with azimuthal density nonuniformity in a cylindrical beam tunnel. *IEEE Transactions on Plasma Science*, 32(3):890–898, June 2004. doi: 10.1109/TPS.2004.827617.

[56] D. J. Griffiths. *Introduction to electrodynamics*. Pearson, Boston, fourth edition edition, 2013. ISBN 978-0-321-85656-2.

[57] E. Thébault, C. C. Finlay, C. D. Beggan, P. Alken, J. Aubert, O. Barrois, F. Bertrand, T. Bondar, A. Boness, L. Brocco, E. Canet, A. Chambodut, A. Chulliat, P. Coïsson, F. Civet, A. Du, A. Fournier, I. Fratter, N. Gillet, B. Hamilton, M. Hamoudi, G. Hulot, T. Jager, M. Korte, W. Kuang, X. Lalanne, B. Langlais, J.-M. Léger, V. Lesur, F. J. Lowes, S. Macmillan, M. Mandea, C. Manoj, S. Maus, N. Olsen, V. Petrov, V. Ridley, M. Rother, T. J. Sabaka, D. Saturnino, R. Schachtschneider, O. Sirol, A. Tangborn, A. Thomson, L. Tøffner-Clausen, P. Vigneron, I. Wardinski, and T. Zvereva. International Geomagnetic Reference Field: the 12th generation. *Earth, Planets and Space*, 67(1):79, May 2015. doi: 10.1186/s40623-015-0228-9.

[58] S. Garavaglia. WPHCD-EC2022_rfbuilsings+Ducts+MBTLs, December 2023. URL `https://idm.euro-fusion.org/default.aspx?uid=2QKD32`. Accessed on: 2024-02-22 10:47:06.

[59] Infineon Technologies AG. TLE493D-A2B6 - Infineon Technologies, April 2019. URL `https://www.infineon.com/cms/en/product/sensor/magnetic-sensors/magnetic-position-sensors/3d-magnetics/tle493d-a2b6/`. Accessed on: 2024-11-14 09:29:44.

[60] F. Leuterer, M. Beckmann, H. Brinkschulte, F. Monaco, M. Münich, F. Ryter, H. Schütz, L. Empacher, G. Gantenbein, W. Förster, W. Kasparek, P. Schüller, K. Schwörer, A. Borchegowski, A. Fix, V. Illin, L. Popov, V. Sigalaev, and E. Tai. Experience with the ECRH system of ASDEX-Upgrade. *Fusion Engineering and Design*, 53(1):485–489, January 2001. doi: 10.1016/S0920-3796(00)00524-X.

[61] H. G. Kosmahl. Modern multistage depressed collectors—A review. *Proceedings of the IEEE*, 70(11):1325–1334, November 1982. doi: 10.1109/PROC.1982.12481.

[62] T. G. Mihran and W. Neugebauer. Analytic study of a depressed collector for linear beam microwave amplifiers Final report. Technical Report NASA-CR-72768, July 1970. URL https://ntrs.nasa.gov/citations/19710001886. Accessed on: 2024-11-14 13:46:09.

[63] A. Mercy Latha and S. K. Ghosh. A comprehensive review of depressed collectors of slow-wave devices. *Journal of Electromagnetic Waves and Applications*, 35(1):95–137, January 2021. doi: 10.1080/09205071.2020.1823895.

[64] B. Piosczyk, A. Arnold, G. Dammertz, O. Dumbrajs, M. Kuntze, and M. K. Thumm. Coaxial cavity gyrotron- recent experimental results. *IEEE Transactions on Plasma Science*, 30(3):819–827, June 2002. doi: 10.1109/TPS.2002.801557.

[65] S. Kern, J.-P. Hogge, S. Alberti, K. Avramides, G. Gantenbein, S. Illy, J. Jelonnek, J. Jin, F. Li, I. Gr Pagonakis, B. Piosczyk, T. Rzesnicki, M. K. Thumm, I. Tigelis, and M. Q. Tran. Experimental results and recent developments on the EU 2 MW 170 GHz coaxial cavity gyrotron for ITER. *EPJ Web of Conferences*, 32:04009, 2012. doi: 10.1051/epjconf/20123204009.

[66] A. Singh, R. L. Ives, R. V. Schumacher, and Y. M. Mizuhara. Multi-stage depressed collector for small orbit gyrotrons, July 1998.

[67] A. Singh, S. Rajapatirana, Y. Men, V. L. Granatstein, R. L. Ives, and A. J. Antolak. Design of a multistage depressed collector system for 1-MW CW gyrotrons. I. Trajectory control of primary and secondary electrons in a two-stage depressed collector. *IEEE Transactions on Plasma Science*, 27(2):490–502, April 1999. doi: 10.1109/27.772278.

[68] R. L. Ives, A. Singh, M. Mizuhara, R. Schumacher, J. Neilson, M. Gaudreau, J. A. Casey, and V. L. Granatstein. Design of a multistage depressed collector system for 1 MW CW gyrotrons. II. System consideration. *IEEE Transactions on Plasma Science*, 27(2):503–511, April 1999. doi: 10.1109/27.772279.

[69] C. Wu, I. Gr. Pagonakis, S. Illy, G. Gantenbein, M. Thumm, and J. Jelonnek. Comparison between controlled non-adiabatic and E×B concepts for gyrotron multistage depressed collectors. *EPJ Web of Conferences*, 149:04005, 2017. doi: 10.1051/epjconf/201714904005.

[70] I. Gr. Pagonakis, J.-P. Hogge, S. Alberti, K. A. Avramides, and J. L. Vomvoridis. A New Concept for the Collection of an Electron Beam Configured by an Externally Applied Axial Magnetic Field. *IEEE Transactions on Plasma Science*, 36(2):469–480, April 2008. doi: 10.1109/TPS.2008.917943.

[71] I. Gr. Pagonakis, C. Wu, S. Illy, and J. Jelonnek. Multistage depressed collector conceptual design for thin magnetically confined electron beams. *Physics of Plasmas*, 23(4):043114, April 2016. doi: 10.1063/1.4947565.

[72] C. Wu, I. Gr. Pagonakis, G. Gantenbein, S. Illy, M. Thumm, and J. Jelonnek. Conceptual designs of E×B multistage depressed collectors for gyrotrons. *Physics of Plasmas*, 24(4):043102, March 2017. doi: 10.1063/1.4979291.

[73] O. I. Louksha and P. A. Trofimov. A method of electron separation for multistep recuperation systems in gyrotrons. *Technical Physics Letters*, 41(9):884–886, September 2015. doi: 10.1134/S1063785015090230.

[74] O. I. Louksha and P. A. Trofimov. A multistage depressed collector system for gyrotrons. In *Eighteenth International Vacuum Electronics Conference (IVEC)*, pages 1–2, April 2017. doi: 10.1109/IVEC.2017.8289518.

[75] B. Ell, I. Gr. Pagonakis, C. Wu, M. Thumm, and J. Jelonnek. Coaxial multistage depressed collector design for high power gyrotrons based on E×B concept. *Physics of Plasmas*, 26(11):113107, November 2019. doi: 10.1063/1.5118338.

[76] C. Wu, I. Gr. Pagonakis, K. A. Avramidis, G. Gantenbein, S. Illy, M. Thumm, and J. Jelonnek. Gyrotron multistage depressed collector based on E×B drift concept using azimuthal electric field. I. Basic design. *Physics of Plasmas*, 25(3):033108, March 2018. doi: 10.1063/1.5016296.

[77] C. Wu, I. Gr. Pagonakis, D. Albert, K. A. Avramidis, G. Gantenbein, S. Illy, M. Thumm, and J. Jelonnek. Gyrotron multistage depressed collector based on E×B drift concept using azimuthal electric field. II: Upgraded designs. *Physics of Plasmas*, 26(1):013108, January 2019. doi: 10.1063/1.5078861.

[78] V. N. Manuilov, M. V. Morozkin, O. I. Luksha, and M. Yu Glyavin. Gyrotron collector systems: Types and capabilities. *Infrared Physics & Technology*, 91:46–54, June 2018. doi: 10.1016/j.infrared.2018.03.024.

[79] M. Glyavin, V. Manuilov, and M. Morozkin. Two-stage Energy Recovery System for DEMO Gyrotron. *43rd International Conference on Infrared, Millimeter, and Terahertz Waves (IRMMW-THz)*, pages 1–2, September 2018. doi: 10.1109/IRMMW-THz.2018.8510139.

[80] M. Schmid, D. Hrabal, B. Piosczyk, and M. Thumm. Past and future upgrades of the gyrotron high voltage cathode power supplies at the Forschungszentrum Karlsruhe. *Fusion Engineering and Design*, 84(7): 1734–1738, June 2009. doi: 10.1016/j.fusengdes.2009.01.059.

[81] G. Gantenbein. Commissioning of the Gyrotron Test Facility FULGOR - First Results, June 2022. URL `https://indico.iter.org/event/2/contributions/743/`.

[82] M. Schmid, J. Franck, P. Kalaria, K. A. Avramidis, G. Gantenbein, S. Illy, J. Jelonnek, I. Gr. Pagonakis, T. Rzesnicki, and M. Thumm. Gyrotron development at KIT: FULGOR test facility and gyrotron concepts for DEMO. *Fusion Engineering and Design*, 96-97:589–592, October 2015. doi: 10.1016/j.fusengdes.2015.03.003.

[83] A. Zein, D. Cesnjevar, A. Epp, G. Gantenbein, S. Illy, Z. Ioannidis, T. Kobarg, W. Leonhardt, D. Mellein, S. Ruefenacht, T. Rzesnicki, M. Schmid, M. Thumm, J. Weggen, and J. Jelonnek. 10 MW FULGOR power supply performance tests and overview of test facility components. In *Indico*, Giardini Naxos, Sicily - Italy, September 2018.

[84] G. Gantenbein, S. Illy, J. Jelonnek, T. Ruess, T. Rzesnicki, M. Schmid, and S. Stanculovic. Status and First Operation of Gyrotron Teststand FULGOR at KIT. *47th International Conference on Infrared, Millimeter and Terahertz Waves (IRMMW-THz)*, pages 1–2, August 2022. doi: 10.1109/IRMMW-THz50927.2022.9895889.

[85] O. I. Louksha and P. A. Trofimov. Highly Efficient Gyrotron with Multi-Stage Recuperation of Residual Electron Energy. *Technical Physics*, 64 (12):1889–1897, December 2019. doi: 10.1134/S1063784219120156.

[86] O. I. Louksha, P. A. Trofimov, V. N. Manuilov, and M. Yu. Glyavin. Trajectory Analysis in a Collector with Multistage Energy Recovery for a DEMO Prototype Gyrotron. Part I. Idealized Magnetic Field Distribution. *Technical Physics*, 66(1):118–123, January 2021. doi: 10.1134/S1063784221010138.

[87] O. I. Louksha, P. A. Trofimov, V. N. Manuilov, and M. Yu. Glyavin. Trajectory Analysis in a Collector with Multistage Energy Recovery for a DEMO Prototype Gyrotron. Part II. Toroidal Magnetic Field. *Technical Physics*, 66(8):992–998, August 2021. doi: 10.1134/S1063784221070082.

[88] O. I. Louksha, A. S. Zuev, A. G. Malkin, E. S. Semenov, P. A. Trofimov, and M. Yu. Glyavin. Trajectory analysis in a collector with multistage energy recovery for a DEMO prototype gyrotron. Part III. Influence of the spent electron beam parameters. *Technical Physics*, 68(5):670, 2023. doi: 10.21883/TP.2023.05.56075.14-23.

[89] O. I. Louksha, A. G. Malkin, and P. A. Trofimov. First Experiments on Multistage Energy Recovery in a 4-mm Wavelength Gyrotron. *IEEE Electron Device Letters*, 45(9):1638–1641, September 2024. doi: 10.1109/LED.2024.3424661.

[90] I. Gr. Pagonakis, K. A. Avramidis, G. Gantenbein, T. Rzesnicki, A. Samartsev, and J. Jelonnek. Magnetic field profile analysis for gyrotron experimental investigation. *Physics of Plasmas*, 24(3):033102, March 2017. doi: 10.1063/1.4977460.

[91] B. F. Ell, C. Wu, G. Gantenbein, S. Illy, M. S. Misko, I. Gr. Pagonakis, J. Weggen, M. Thumm, and J. Jelonnek. Toward the First Continuous Wave Compatible Multistage Depressed Collector Design for High Power Gyrotrons. *IEEE Transactions on Electron Devices*, 70(3):1299–1305, March 2023. doi: 10.1109/TED.2023.3234885.

[92] B. Ell, I. Gr. Pagonakis, C. Wu, D. Albert, G. Gantenbein, S. Illy, T. Kobarg, T. Rzesnicki, M. Thumm, and J. Jelonnek. Mechanical Design Study for Gyrotron E×B Drift Two-Stage Depressed Collector. In *21st International Conference on Vacuum Electronics (IVEC)*, pages 187–188, October 2020. doi: 10.1109/IVEC45766.2020.9520565.

[93] B. Ell, L. Feuerstein, G. Gantenbein, S. Illy, T. Ruess, T. Rzesnicki, S. Stanculovic, M. Thumm, J. Weggen, C. Wu, and J. Jelonnek. Robustness of the E×B MDC prototype design for gyrotrons. *Fusion Engineering and Design*, 215:114979, June 2025. doi: 10.1016/j.fusengdes.2025.114979.

[94] B. Ell, C. Wu, L. Feuerstein, G. Gantenbein, S. Illy, T. Ruess, T. Rzesnicki, S. Stanculovic, M. Thumm, J. Weggen, and J. Jelonnek. Fabrication and assembly of the gyrotron multi-stage depressed collector prototype at KIT. *EPJ Web of Conferences*, 313:04006, 2024. doi: 10.1051/epjconf/202431304006.

[95] dahren. Damid-200-Flat. URL `https://www.dahrengroup.com/wp-content/uploads/2023/04/Damid-200-Flat.pdf`. Accessed on: 2024-01-30 09:35:15.

[96] M. Seilmayer, V. Kumar Katepally, and Department of Magnetohydrodynamics, Institute of Fluid Dynamics, Helmholtz-Zentrum Dresden-Rossendorf, Dresden, Germany. Thermal conductivity survey of different manufactured insulation systemsof rectangular copper wires. *AIMS Electronics and Electrical Engineering*, 2(1):27–36, 2018. doi: 10.3934/ElectrEng.2018.1.27.

[97] K. A. Avramidis, T. Ruess, F. Mentgen, J. Jin, D. Wagner, G. Gantenbein, S. Illy, C. Ioannidis, H. P. Laqua, I. Gr. Pagonakis, T. Rzesnicki, M. Thumm, R. C. Wolf, and J. Jelonnek. Studies towards an upgraded 1.5 MW gyrotron for W7-X. *EPJ Web of Conferences*, 203:04003, 2019. doi: 10.1051/epjconf/201920304003.

[98] T. Rzesnicki, K. A. Avramidis, I. Chelis, G. Gantenbein, S. Illy, Z. C. Ioannidis, J. Jin, M Thumm, and J. Jelonnek. 1.5 MW, 140 GHz Gyrotron for W7-X - development status and experimental results -. *47th International Conference on Infrared, Millimeter and Terahertz Waves (IRMMW-THz)*, pages 1–2, August 2022. doi: 10.1109/IRMMW-THz50927.2022.9896025.

[99] T. Ruess. *A First 2 MW-Class (136)/170/204 GHz Multi-Frequency Gyrotron Pre-Prototype for DEMO: Design, Construction and Key Components Verification*, volume 18 of *Karlsruher Forschungsberichte aus*

dem Institut für Hochleistungsimpuls- und Mikrowellentechnik. Karlsruher Institut für Technologie (KIT), 2023. ISBN 978-3-7315-1309-4. doi: 10.5445/KSP/1000160391.

[100] K. A. Avramides, C. T. Iatrou, and J. L. Vomvoridis. Design considerations for powerful continuous-wave second-Cyclotron-harmonic coaxial-cavity gyrotrons. *IEEE Transactions on Plasma Science*, 32(3): 917–928, June 2004. doi: 10.1109/TPS.2004.828781.

[101] L. Feuerstein, A. Marek, C. Wu, S. Illy, M. Thumm, and J. Jelonnek. Design of a Second Harmonic MW-Level Coaxial Gyrotron Cavity. In *24th International Vacuum Electronics Conference (IVEC)*, pages 1–2, April 2023. doi: 10.1109/IVEC56627.2023.10156958.

[102] S. Illy, K. A. Avramidis, I. Chelis, B. Ell, L. Feuerstein, G. Gantenbein, Z. Ioannidis, J. Jelonnek, J. Jin, G. Latsas, A. Marek, D. Peponis, T. Rzesnicki, M. Thumm, I. Tigelis, and C. Wu. Progress in the Design of Megawatt-Class Fusion Gyrotrons Operating at the Second Harmonic of the Cyclotron Frequency. *48th International Conference on Infrared, Millimeter, and Terahertz Waves (IRMMW-THz)*, pages 1–2, September 2023. doi: 10.1109/IRMMW-THz57677.2023.10299170.

[103] D. M. Anderson. *Design for Manufacturability*. CRC Press, 2014. ISBN 978-1-4822-0492-6.

[104] G. Boothroyd. Product design for manufacture and assembly. *Computer-Aided Design*, 26(7):505–520, July 1994. doi: 10.1016/0010-4485(94)90082-5.

[105] B. Ell, I. Gr. Pagonakis, C. Wu, G. Gantenbein, S. Illy, T. Rzesnicki, S. Stanculovic, M. Thumm, J. Weggen, and J. Jelonnek. Mechanical Design of the Short Pulse E×B Drift Two-Stage Depressed Collector Prototype for High Power Gyrotron. In *22nd International Vacuum Electronics Conference (IVEC)*, pages 1–2, April 2021. doi: 10.1109/IVEC51707.2021.9722425.

[106] B. Ell, C. Wu, G. Gantenbein, S. Illy, I. Gr Pagonakis, T. Rzesnicki, S. Stanculovic, M. Thumm, J. Weggen, and J. Jelonnek. Design of a Two-Stage Depressed Collector for Continuous Wave Operation of MW-Class Gyrotrons. In *23rd International Vacuum Electronics Conference*

(IVEC), 2022. URL https://publikationen.bibliothek.kit.edu/1000146726.

[107] S. Illy and B. Piosczyk. Simulating the effect of secondary emission in the collector of high power CW gyrotrons, June 2008.

[108] B. Ell, C. Wu, G. Gantenbein, S. Illy, M. Misko, I. Gr. Pagonakis, M. Thumm, and J. Jelonnek. Novel High-Frequency Electric Field Sweeping Concept for High-Power Gyrotron Collectors. *IEEE Transactions on Electron Devices*, 70(3):1312–1317, March 2023. doi: 10.1109/TED.2023.3240121.

[109] S. Illy, S. Kern, I. Gr. Pagonakis, and A. Vaccaro. Collector Loading of the 2-MW, 170-GHz Gyrotron for ITER in Case of Beam Power Modulation. *IEEE Transactions on Plasma Science*, 41(10):2742–2747, October 2013. doi: 10.1109/TPS.2013.2262607.

[110] B. Lyu. *Thermal investigation and lifetime estimation for the design improvement of a 2 MW fusion gyrotron collector*. Master's thesis, Karlsruhe Institute of Technology, Karlsruhe, Germany, July 2020.

List of Figures

List of Tables